

Dynamics of the East Asian Summer Monsoon in Present and Future Climates

Thesis by

Jinqiang Chen

In Partial Fulfillment of the Requirements

for the Degree of

Doctor of Philosophy



California Institute of Technology

Pasadena, California

2016

(Defended August 25, 2015)

© 2015

Jinxiang Chen

All Rights Reserved

To my curiosity for climate science, and humans' broader fight against climate change.

Acknowledgments

Four years ago, with great ambition to understand and fight against climate change, I came to Caltech. Four years later, I am summarizing my Ph.D. work, ready to move forward to solve climate problems through policy innovation. Looking backward, I had a couple of dramatic turnovers in my life: one was my career expansion from climate science to energy policy; the other one was my drowning accident a few days after I arrived in the States. There started most of my unforgettable stories, throughout which I met several good friends. Some of them ended up being important ones. I feel really happy and lucky to have them in my life. In finishing my thesis, I would like to spare some pages to acknowledge their significant roles during my Ph.D. life.

I want to thank my Ph.D. advisor Simona Bordoni. Simona has been a great advisor in inspiring, encouraging, and supporting me in my academic life. I developed my Ph.D. research from scratch under her guidance. She is a very patient, enthusiastic, humble, and immensely knowledgeable intellectual. Collaborating with her has been a productive and enjoyable learning experience. In addition, she has gracefully offered me freedom to explore climate change problems from various perspectives. I am extremely lucky to have Simona as my academic advisor and I do not think I could ever overestimate her contribution to my academic development. I want to tell her: *“Senza di te il mio successo non si sarebbe facilmente avverato.”*

I would also like to thank my Ph.D. thesis committee members Andrew Ingersoll, Andrew Thompson, Jess Adkins, Paul Wennberg, and Simona Bordoni for their valuable input in my Ph.D. work. In particular, I want to thank Simona and Paul for offering tremendous

support to my academic life and career expansion. Paul was a research supervisor for one of my qualifying exam projects. Like Simona, he has been sitting on all my exams and has witnessed my growth at Caltech. He has been greatly helpful and supportive during my Ph.D. life.

I also want to thank Yuk Young for gracefully treating me as a Chinese member of his group.

I want to thank members of Simona's group – Anne Laraia, Jennifer Walker, Ho-Hsuan Wei, Hyo-Seok Park, Joan Ballester, Nicole Feldl, Salvatore Pascale, Alex Henny – and Zhihong Tan for helpful discussion and a joyful time together.

I want to thank the Caltech administrators Liz Boyd, Marcia Hudson, Nora Oshima, Kathy Young, and Megan Schmid for their help during my stay at Caltech.

I want to thank my American Mom, Maria Lopez. I came to know Maria when I was visiting the Caltech Counseling Center. It was right after I was discharged from hospital and they wanted to know if I was doing well. I remember that the first time I met Maria she was so welcoming, considerate, and empathetic. She offered to help with any problems, which to me – someone who had no friends or relatives nearby after a nearly fatal accident – was truly caring. Indeed, in the following days, I turned to Maria for help and advice, and soon we became good friends. She has been my American Mom for several years and she is a kind, good-hearted person who makes me feel cherished on my birthday.

I want to thank my excellent personal mentors, Laura Flower Kim and Natalie Gilmore. On the first day I was discharged from the hospital, they treated me to dinner and a long conversation, and we have maintained our friendship thereafter. Laura, Associate Director of International Student Programs, has done a great favor in helping me maneuver the transition between student life and my new professional life. Natalie Gilmore, Associate Dean of Graduate Studies, has offered me understanding, support and encouragement throughout my Ph.D. Both Laura and Natalie have both been great friends to whom I turn when I need help, and they are always ready to give constructive advice.

I want to thank my landlady and awesome housemate Maribelle Denslow, for treating me as a family member for the past couple of years. I learnt so much about American culture, mentality and daily lifestyle from her, especially those subtle differences that really make me think about how elements of culture are reflected in national policy making. She is also a very funny and interesting person – she would count while I do pushups and she wants to be parented while wanting ice cream. We had a wonderful time together. Thanks to her, I came to know Fengying Ming, a previous tenant. Fengying is a very understanding, considerate, elegant, and well-mannered friend with lots of stories to share. She has played a significant role in my spiritual life at Caltech. She later became my Gan Ma (adopted Mom in Mandarin).

I want to express my special gratitude to Bill Crowfoot for being an excellent but unassuming mentor, and a thoughtful but critical friend. He inspired me to solve climate change problems from different angles, and encouraged me to add financial and political flavors. His innovative, insightful, and critical thinking about the world is always admirable to me. Thank you so much, Bill, for motivating me to embark on this exciting journey.

Last but most important, I want to thank my family – my grandparents, my parents, my aunts, my uncles, and my friends in China, in Europe, and here at Caltech – for giving me love, support, and understanding in my life. In particular, I want to thank my grandma for bringing me up and finding the courage to visit me in the States. Without you, I could not have achieved so much. I love you all.

ABSTRACT

This thesis aims at enhancing our fundamental understanding of the East Asian summer monsoon (EASM), and mechanisms implicated in its climatology in present-day and warmer climates. We focus on the most prominent feature of the EASM, i.e., the so-called Meiyu-Baiu (MB), which is characterized by a well-defined, southwest to northeast elongated quasi-stationary rainfall band, spanning from eastern China to Japan and into the northwestern Pacific Ocean in June and July.

We begin with an observational study of the energetics of the MB front in present-day climate. Analyses of the moist static energy (MSE) budget of the MB front indicate that horizontal advection of moist enthalpy, primarily of dry enthalpy, sustains the front in a region of otherwise negative net energy input into the atmospheric column. A decomposition of the horizontal dry enthalpy advection into mean, transient, and stationary eddy fluxes identifies the longitudinal thermal gradient due to zonal asymmetries and the meridional stationary eddy velocity as the most influential factors determining the pattern of horizontal moist enthalpy advection. Numerical simulations in which the Tibetan Plateau (TP) is either retained or removed show that the TP influences the stationary enthalpy flux, and hence the MB front, primarily by changing the meridional stationary eddy velocity, with reinforced southerly wind on the northwestern flank of the north Pacific subtropical high (NPSH) over the MB region and northerly wind to its north. Changes in the longitudinal thermal gradient are mainly confined to the near downstream of the TP, with the resulting changes in zonal warm air advection having a lesser impact on the rainfall in the extended MB region.

Similar mechanisms are shown to be implicated in present climate simulations in the Couple Model Intercomparison Project - Phase 5 (CMIP5) models. We find that the spatial distribution of the EASM precipitation simulated by different models is highly correlated with the meridional stationary eddy velocity. The correlation becomes more robust when energy fluxes into the atmospheric column are considered, consistent with the observational

analyses. The spread in the area-averaged rainfall amount can be partially explained by the spread in the simulated globally-averaged precipitation, with the rest primarily due to the lower-level meridional wind convergence. Clear relationships between precipitation and zonal and meridional eddy velocities are observed.

Finally, the response of the EASM to greenhouse gas forcing is investigated at different time scales in CMIP5 model simulations. The reduction of radiative cooling and the increase in continental surface temperature occur much more rapidly than changes in sea surface temperatures (SSTs). Without changes in SSTs, the rainfall in the monsoon region decreases (increases) over ocean (land) in most models. On longer time scales, as SSTs increase, rainfall changes are opposite. The total response to atmospheric CO₂ forcing and subsequent SST warming is a large (modest) increase in rainfall over ocean (land) in the EASM region. Dynamic changes, in spite of significant contributions from the thermodynamic component, play an important role in setting up the spatial pattern of precipitation changes. Rainfall anomalies over East China are a direct consequence of local land-sea contrast, while changes in the larger-scale oceanic rainfall band are closely associated with the displacement of the larger-scale NPSH. Numerical simulations show that topography and SST patterns play an important role in rainfall changes in the EASM region.

Contents

Acknowledgments	iv
1 Motivation	1
1.1 Present climate	3
1.2 Model spread	8
1.3 Future climate	8
1.4 Goals of this dissertation work	11
2 Energetics of the EASM system	13
2.1 Data and method	13
2.2 Thermodynamic equation	14
2.3 MSE budget	16
2.4 Energy advection decomposition	22
2.5 Moisture budget	27
2.6 Conclusions	29
3 Orographic effect of the TP on the EASM formation	31
3.1 Data and method	31
3.2 Numerical simulations	32
3.3 Conclusions	41
4 Inter-model spread of EASM simulations	44
4.1 Data and method	44

4.2	Assessment of inter-model spread	48
a	Spatial structure	49
b	Rainfall amount	51
4.3	Conclusions	53
5	Response of the East Asian Summer Monsoon to Atmospheric CO₂ Forcing and Subsequent Sea Surface Warming	55
5.1	Data and Method	55
5.2	Rainfall anomalies	59
a	Fast Response	60
b	Slow response	61
c	Summary	70
5.3	Numerical simulations	71
a	Land warming	72
b	SST patterns	72
5.4	Summary and discussion	73
6	Conclusions	78
7	Appendix: Decomposition of the approximated vertical velocity	84

List of Figures

1.1	Climatological mean precipitation during the MB season. Bold black contour shows where orography intersects the 800 mb level.	5
-----	---	---

- 1.2 Climatology of the MB season from 1997 to 2009. a) Seasonal cycle of the precipitation averaged over the area enclosed by the red lines in Fig. 1.1, where precipitation is the largest. The blue and yellow lines show the daily mean precipitation and filtered precipitation by a low pass filter with a cutoff period of 20 days, respectively. The tick marks on the horizontal axis correspond to the middle of each month. b) Interannual precipitation anomaly over the enclosed region. 6
- 1.3 MB climatology. a) Moisture flux convergence (color contours, $\text{g kg}^{-1} \text{ day}^{-1}$) and near surface (925 mb) specific humidity (line contours, g kg^{-1}). b) Absolute value of lower-level (850 mb) temperature gradient (color contours, K (1000 km)^{-1}) and temperature (line contours, K). c) Lower-level (850 mb) wind convergence (color contours, 10^6 s^{-1}) and wind field (vector, m s^{-1}). d) Lower-level (850 mb) meridional wind (color contours, m s^{-1}) and meridional divergence (line contours, $\text{m s}^{-1}(\text{1000 km})^{-1}$). 7
- 2.1 Mid-tropospheric temperature advection in the MB season. Columns show zonal (left), meridional (middle), and total (right) horizontal temperature advection. Rows show the total advection (top), the mean advection (middle), and the transient eddy term (bottom). In all panels, color contours indicate temperature advection (K day^{-1} , with warm/cold colors indicating warm/cold air advection) and line contours indicate the mid-tropospheric vertical velocity (Pa s^{-1} , with upward/downward motion in solid/dash contours and the zero contour thickened.) 16
- 2.2 Vertically integrated MSE budget. Net energy flux into the atmospheric column $\overline{F^{net}}$ (left), vertical integral of horizontal moist enthalpy advection $-\langle \overline{\mathbf{v} \cdot \nabla E} \rangle$ (middle), and vertical integral of vertical MSE advection $-\langle \overline{\omega \frac{\partial h}{\partial p}} \rangle$ (right) for the pre-MB season (top), MB season (middle), and post-MB season (bottom). Contours are in W m^{-2} . 19

- 2.3 Vertical MSE advection computed as $\overline{F^{net}} - \langle \mathbf{v} \cdot \nabla E \rangle$ (color contours, W m^{-2} , left) and GPCP climatological mean precipitation (color contours, mm day^{-1} , right). Rows are the same as in Fig. 2.2. In all panels, line contours show vertical velocity (Pa s^{-1} , contour interval 0.02 Pa s^{-1}), with upward/downward motion in solid/dash contours and the zero contour thickened. 23
- 2.4 Eddy decomposition of the vertical integral of the horizontal moist enthalpy advection $-\langle \mathbf{v} \cdot \nabla E \rangle$ (left), the horizontal dry enthalpy advection $-\langle c_p \mathbf{v} \cdot \nabla T \rangle$ (middle), and the latent energy advection $-\langle L_v \mathbf{v} \cdot \nabla q \rangle$ (right) during the MB season. Rows indicate the total advection $-\langle \mathbf{v} \cdot \nabla(\cdot) \rangle$ (a,b,c), the advection of the stationary eddy energy by the zonal-mean flow $-\langle [\overline{\mathbf{v}}] \overline{\nabla(\cdot)^*} \rangle$ (d,e,f), the advection of the zonal-mean energy by the stationary eddy velocity $-\langle \mathbf{v}^* [\overline{\nabla(\cdot)}] \rangle$ (g,h,i), the advection of the stationary eddy energy by the stationary eddy velocity, or pure stationary eddy $-\langle \mathbf{v}^* \overline{\nabla(\cdot)^*} \rangle$ (j,k,l), and the advection of the transient eddy energy by the transient eddy velocity $-\langle \mathbf{v}' \cdot \nabla(\cdot)' \rangle$ (m,n,o). Contours are in W m^{-2} . 24
- 2.5 Moisture budget for the MB season. a) Vertically integrated moisture flux convergence $-\langle \overline{\nabla \cdot (\mathbf{v}q)} \rangle$. b) Evaporation E . c) Product of moisture and wind convergence $-\langle \overline{q \nabla \cdot \mathbf{v}} \rangle$. d) Moisture advection $-\langle \mathbf{v} \cdot \nabla q \rangle$. Units are mm day^{-1} . Line contours are precipitation with interval 1 mm day^{-1} . 28
- 2.6 Eddy decomposition of the vertical integral of the the product of moisture and wind convergence $-\langle \overline{q \nabla \cdot \mathbf{v}} \rangle$ (e) into the product of the stationary eddy convergence and the zonal-mean specific humidity $-\langle [\overline{q}] \overline{\nabla \cdot \mathbf{v}^*} \rangle$ (a), the product of the zonal-mean flow convergence and the stationary specific humidity $-\langle \overline{q^*} [\overline{\nabla \cdot \mathbf{v}}] \rangle$ (b), the product of the stationary eddy convergence and the stationary specific humidity or pure stationary eddy $-\langle \overline{q^* \nabla \cdot \mathbf{v}^*} \rangle$ (c), and the product of the transient flow convergence and the transient specific humidity $-\langle \overline{q' \nabla \cdot \mathbf{v}'} \rangle$ (d) during the MB season. Contours are in W m^{-2} . 29

- 3.1 Hovmöller plot of precipitation averaged from 110°E to 160°E in GPCP v1.1 (a), AM2.1 simulations with the TP (b) and without the TP (c). 33
- 3.2 Precipitation (upper, color contours, mm day⁻¹) and vertical MSE advection (bottom, color contours, W m⁻²) of AM2.1 integration with the TP (right) and without the TP (left) during the MB season. Line contours indicate vertical ascending velocity (Pa s⁻¹, contour interval 0.02Pa s⁻¹) at 500 mb. 34
- 3.3 Anomalies (TP - noTP experiments) in horizontal dry enthalpy advection $-\langle c_p \mathbf{v} \cdot \nabla T \rangle$ (color contours) and vertically-integrated (normalized, not mass-weighted) meridional stationary eddy velocity divergence $\langle \overline{\partial_y v^*} \rangle$ (line contours, contour interval 10⁻⁶ s⁻¹) (a), latent energy advection $-\langle \overline{L_v \mathbf{v} \cdot \nabla q} \rangle$ (b), the advection of the stationary eddy dry enthalpy by the zonal-mean flow $-\langle c_p [\overline{\mathbf{v}}] \cdot \overline{\nabla T^*} \rangle$ (c), the advection of the zonal-mean dry enthalpy by the stationary eddy velocity $-\langle c_p \overline{\mathbf{v}^*} \cdot [\overline{\nabla T}] \rangle$ (color contours) and vertically-integrated (normalized, not mass-weighted) stationary eddy wind fields (vectors) with reference vector 3 m s⁻¹ (d), the advection of the stationary eddy energy by the stationary eddy velocity $-\langle c_p \overline{\mathbf{v}^*} \cdot \overline{\nabla T^*} \rangle$ (e), and the advection of the transient eddy energy by the transient eddy velocity $-\langle c_p \overline{\mathbf{v}'} \cdot \overline{\nabla T'} \rangle$ (f). 36
- 3.4 Anomaly (TP - noTP experiments) in the product of the zonal mean moisture and stationary eddy divergence $\langle [\overline{q}] \overline{\nabla \cdot \mathbf{v}^*} \rangle$. Contours are in mm day⁻¹. 37
- 3.5 Meridional stationary eddy velocity $\overline{v^*}$ (color contours, m s⁻¹) and its convergence $\overline{\partial_y v^*}$ (line contours, contour interval 10⁻⁶ s⁻¹) averaged from 110°E to 160°E in the ERA-Interim reanalysis data (a), in the AM2.1 simulation in the presence of the TP (b), in the absence of the TP (c), and the difference between a and b (d). 39
- 3.6 Anomalies (TP - noTP experiments) in $\partial_y \overline{v^*}$ (a), $\partial_x \overline{u^*}$ (b), and $\nabla \cdot \overline{\mathbf{v}^*}$ (c) integrated (normalized, not mass-weighted) from surface to 700 mb. Contours are in day⁻¹. 40

- 4.1 June-July climatological mean precipitation (shaded, mm day^{-1}) for the 2001-2009 nine-year period for the CMIP5 decadal2000 MMM (a), GPCP (b) and TRMM (c). Line contours (contour interval 0.5 mm day^{-1}) in (a) show the model spread or standard deviation of the twenty experiments listed in Fig. 4.2. Line contours in (b) and (c) show vertically-normalized stationary zonal and meridional eddy velocities, $\{\overline{u^*}\}$ and $\{\overline{v^*}\}$ (contour interval 1 m s^{-1} and 0.4 m s^{-1}), respectively. Red contour encloses the EASM region, comprising East China and the CBP region. See text for details. 47
- 4.2 Spatial pattern correlation (centered) between the precipitation over the EASM region (left in each column), East China (middle), and the CBP region (right) and the metrics indicated in the diagram. Each metric is summarized by a boxplot, characterized by mean value and standard deviation of correlation (with the exception of FGOALS-s2). The name of the seventeen models and three additional experiments with different initialization method are labeled in the legend, with initialization methods (when necessary) labeled with $i\#$, and the number in parenthesis indicating the number of ensembles. 50
- 4.3 Regression between the regional precipitation \overline{P} (x -axis) and (top) global precipitation $[\overline{P}]$ (y -axis), between the estimated moisture flux convergence $\overline{P} - \overline{E}$ (x -axis) and (center) normalized $-\int_{surf}^{700mb} \overline{q^d} \partial_y \overline{v^{*d}} dp$ (y -axis), and (bottom) vertically-normalized stationary zonal wind eddy velocity $\{\overline{u^*}\}$ (y -axis) over the EASM region (left), East China (middle), and the CBP region (right). The coefficient of determination R^2 is calculated based on all models except for FGOALS-s2, which does not satisfy the global P-E budget, excludes ECMWF reanalysis, GPCP, and TRMM products, and is significant at the 95% level of a two-tailed Student's t test if larger than 21%. The dashed line denotes the one-to-one relationship. 53

- 5.1 Multi-model mean changes in precipitation (shading, W/m^2) between different climate states and climatological precipitation (linear contour interval 1 mm/day, 3 – 9 mm/day) in each base state. 61
- 5.2 MMM anomalies (shading, W/m^2) between sstClim4xCO2 and sstClim of net precipitation $\delta(P - E)$ (a), evaporation δE (b), mean flux convergence $-\langle \delta \nabla(\mathbf{v} \cdot Hq_s) \rangle$ (c), transient component (d, subtracted from a by c), wind component $-\langle \nabla(\delta \mathbf{v} \cdot Hq_s) \rangle$ (e), relative humidity component $-\langle \nabla(\mathbf{v} \cdot \delta Hq_s) \rangle$ (f), temperature component $-\langle \nabla(\mathbf{v} \cdot H\delta q_s) \rangle$ (g), temperature component due to the Planck response (surface temperature) $-\alpha \delta T_s(P - E)$ (h), temperature component due to lapse rate response (i, subtracted from g by h), covariance between relative humidity and wind $-\langle \nabla(\delta \mathbf{v} \cdot \delta Hq_s) \rangle$ (j), covariance between relative humidity and temperature $-\langle \mathbf{v} \cdot \nabla(\delta H\delta q_s) \rangle$ (k), and covariance between wind and temperature $-\langle \nabla(\delta \mathbf{v} \cdot H\delta q_s) \rangle$ (l). Line contour (contour interval 1 mm/day, solid (dash) line means positive (negative) value) indicates climatological net precipitation in sstClim4xCO2 (a,c-l), climatological evaporation (b). 62
- 5.3 Same with Fig. 5.2 but for slow response. 63
- 5.4 MMM anomalies of precipitation (shading, W/m^2) due to winds, winds at 850 mb (vector, m/s), and difference in geopotential height between its maximum and locational value (line contour, contour interval 30 m, solid black, purple and brown lines indicate sstClim, sstClim4xCO2, and abrupt4xCO2, respectively) at 850 mb in the fast (a) and slow (b) responses. Short dash lines in black and purple indicate the inter-model spread (1 standard deviation) in sstClim and sstClim4xCO2 simulations. 65
- 5.5 MMM anomalies of climatological moisture weighted wind convergence (shading, W/m^2) and vertical velocity at 500 mb (line contour, contour interval 0.005 Pa/s). Solid/dash line indicates ascending/descending motion. 66

- 5.6 MMM anomalies of approximated vertical velocity $\omega_{500\text{apprx}}$ (Eq. 7.1, shading, Pa/s) and MMM anomalies of climatological vertical velocity at 500 mb (line contour, contour interval 0.005 Pa/s). Solid/dash line indicates ascending/descending motion. $\omega_{500\text{apprx}}$ is multiplied by a factor of 2 in the fast response (a). 68
- 5.7 MMM anomalies of energy input (a and c, first term in Eq. 7.2, shading, W/m^2), fractional changes in stability weighted by climatological energy input (b and d, second term in Eq. 7.2, shading, W/m^2), and climatological vertical velocity at 500 mb (line contour, contour interval 0.005 Pa/s) in the fast (a and b) and slow (c and d) responses. Solid/dash line indicates ascending/descending motions. 69
- 5.8 Zonal (a, c) and meridional (b, d) components of MMM anomalies of climatological moisture advection at 850 mb (shading, W/m^2) in the fast (a, b) and slow (c, d) responses. 70
- 5.9 Scatterplot (blue/red for fast/slow reponse) of meridional wind anomaly over East China and adjacent oceans (25N-40N, 110E-130E) and surface pressure gradient anomaly between land (100E-120E) and ocean (130E-150E) over 25N-40N band. Each dot represents one model output as indicated in Table 5.1. Solid line indicates linear regression line in fast/slow response, respectively. See text for more details. 71
- 5.10 GFDL AM2.1 simulations of precipitation (shading, W/m^2) in the fast response with full topography (left) and without topography (right) in May (a,b), June (c,d), and July (e,f). Line contour (contour interval 1 mm/day, 3 – 9 mm/day) indicates climatological precipitation in each comparison. 73

- 5.11 GFDL AM2.1 simulations of precipitation in June (shading, W/m^2) with CMIP5 anomalous SST pattern (a) and with 4K uniform SST increase (b). Line contour (contour interval 1 mm/day, 3 – 9 mm/day) indicates climatological precipitation. 74
- 5.12 GFDL AM2.1 simulations of surface temperature (shading, W/m^2), 850 mb winds (vector) and the westerly core (maximum westerly wind, black indicates climatology, purple and blue indicate simulations with CMIP5 anomalous SST pattern and 4K uniform SST increase, respectively) with CMIP5 anomalous SST pattern (a) and with 4K uniform SST increase (b). 75
- 5.13 GFDL AM2.1 simulations of net precipitation (a-c), evaporation (d-f), wind component (g-i), relative humidity component (j-l) and temperature component (m-o) as in Fig. 5.2 for fast response (left), slow response (middle), and slow response with uniform 4K increase in SSTs (right) with full topography. Line contour (contour interval 1 mm/day, 3 – 9 mm/day) indicates climatological precipitation in each comparison. 76
- 6.1 GFDL AM2.1 simulations of geopotential height at 750 mb in the presence (top) and absence (bottom) of global topography. Color shading indicates topography height. 80
- 6.2 Schematic of the role of the TP (red oval) in the NPSH (dashed lined) and the EASM in present-day climate. 81
- 6.3 Schematic of the fast response of the EASM to CO_2 forcing. Notation as in Fig. 6.2. 82
- 6.4 Schematic of the slow response of the EASM to CO_2 forcing. Notation as in Fig. 6.2. 83

List of Tables

5.1	CMIP5 models that have outputs in piControl, sstClim, sstClim4xCO2, and abrupt4xCO2.	56
5.2	Experiments designed by using the GFDL-AM2.1.	60

Chapter 1

Motivation

Monsoons are conventionally defined as summertime tropical circulations with seasonally reversing prevailing winds accompanied by alternating dry and wet seasons associated with zonally asymmetric heating (e.g., Webster 1987; Webster and Fasullo 2003; Trenberth et al. 2006). They exert a significant and far-reaching influence on the general circulation of the atmosphere, the global hydrological cycle and the atmospheric energy transport (e.g., Dima and Wallace 2003; Rodwell and Hoskins 1996, 2001). The Asian monsoon, the largest monsoon system on Earth, plays a crucial role in the entire eastern hemisphere tropics, subtropics, and mid-latitudes, and affects 60% of the world population (e.g., Wang 2006). The East Asian summer monsoon (EASM) is one important branch of the Asian Monsoon. On the large scale, the EASM is primarily characterized by a quasi-stationary, southwest to northeast elongated rainfall band, spanning from China to Japan into the northwestern Pacific (Fig. 1.1a). This precipitation front brings the major rainy season, referred to as Meiyu in China and Baiu in Japan,¹ in these densely-populated and rapidly-growing regions. Its large intraseasonal and interannual variability causes flooding, droughts, heat waves, and other consequent natural hazards, affecting millions of people's lives and resulting in huge economic losses (e.g., Gao and Yang 2009; Sampe and Xie 2010; Waliser 2006; Yang and Lau

¹In China, the name “Meiyu” is used for persistent rainfall from mid-June to mid-July over the Yangtze River Valley (Tao 1987). The name “Baiu” is used in Japan during the same period (Saito 1985). In Chinese, “Mei” means plums, which in the Yangtze River valley reach maturity in the Meiyu-Baiu season. A homonym of “Mei” in Chinese means mold, which vividly describes the tendency to molding under very moist and warm atmospheric conditions.

2006).

Because of the socioeconomic importance of the EASM, its meteorological and climatological significance are highlighted and widely investigated in the literature (e.g., Ding and Chan 2005; Wang 2006). However, even its large-scale dynamics, let alone factors controlling its multi-scale variability, remains poorly understood. Fundamental questions, such as what controls the location and the seasonal evolution of the EASM front, or why maximum rainfall is not colocated with maximum SSTs, remain largely unanswered. Finding answers to these questions is even more pressing in the face of the predicted expansion of subtropical dry zones with climate change, with potentially significant impacts on subtropical precipitation fronts such as the EASM, and enhanced regional sensitivity to greenhouse gases and aerosol radiative forcing (e.g., Hirahara et al. 2012; Hsu et al. 2013).

Despite being a large-scale feature of the summer tropical and subtropical circulation over eastern Asia and the northwestern Pacific, the EASM is not well represented in most state-of-the-art Global Climate Models (GCMs), both in terms of its climatological features and seasonal evolution (Sampe and Xie 2010). Large inter-model spread in EASM simulations exists in current climate simulations that are amplified when considering future projections. Model resolution is found to be a factor affecting the quality of the simulated large-scale precipitation over the EASM region (IPCC AR4, Solomon et al. 2007), but it is not the only factor: improvements in EASM rainfall simulations can only be observed in some models and do not continue when resolution is high enough. Ocean-atmosphere interactions are other factors believed to produce significantly different simulated precipitation in the Asian monsoon: the intensity of the EASM is relatively lower in AGCMs (Atmospheric General Circulation Models) in which sea surface temperatures (SSTs) are prescribed, and no interaction between atmosphere and ocean is allowed (Gao et al. 2011; Kitoh 2004).

In the following, I provide a review of the current knowledge of the EASM, which is divided in three different sections to reflect the three overarching goals of this dissertation work.

1.1. Present climate

The climatology of the EASM has been widely investigated in the literature, but no mechanism for this formation has yet been accepted. In this study, we focus on the energetics of the EASM system and untangle the mechanisms by which the Tibetan Plateau (TP) dominates the formation of the EASM. In general, the EASM is characterized by mixed tropical and mid-latitude influences with frontal systems and jet stream effects (Ding and Chan 2005; Molnar et al. 2010). One of its notable features is its seasonal northward and northeastward migration punctuating three stationary periods, two abrupt northward jumps, and rapid southward retreat: heavy rainfall starts in the South China Sea (SCS) and tropical oceans at the beginning of May and shifts rapidly to the Yangtze River Valley, Korea, and southern Japan in mid-June, when the Meiyu-Baiu (MB) front reaches maturity; in mid-July, the rainfall core jumps to North and Northeast China, marking the end of the MB, and then retreats back to South China at the end of August (e.g., Ding and Chan 2005; Gao et al. 2011; Sampe and Xie 2010).

The formation of the EASM is believed to be the product of land-sea thermal contrast, orographic forcing, and the seasonal shift of the subtropical westerly jet. In simulations with idealized continental configuration, land-sea thermal contrast alone, due to the differing response of land and ocean surfaces to the seasonally varying insolation, was shown to produce a precipitation zone to the east of the continent and a dry zone to the west through Rossby wave dynamics and ventilation of low moist static energy (MSE) air from the ocean to the land, which resemble the large-scale summertime precipitation pattern over Eurasia (Chou et al. 2001). More comprehensive simulations, however, suggest that a realistic EASM can be simulated only when topography over Asia is included (e.g., Kitoh 2004; Liu and Yin 2002; Park et al. 2012a; Wu et al. 2012). The TP has long been held to exert a profound influence on the Asian climate primarily through thermal forcing (e.g., Flohn 1957; Yeh et al. 1957; Li and Yanai 1996). During the warm season, increased surface heat flux over the TP

drives the large-scale atmospheric circulation and reinforces the land-sea thermal contrast, resulting in an intensified EASM (Wu et al. 1997, 2002, 2007b, 2012): elevated heat flux causes cross-isentropic surface airflow along the TP slopes and results in cyclonic circulation around the TP in the lower-troposphere and anticyclonic circulation (the so-called Tibetan or South Asian High, SAH) in the upper troposphere (Yanai and Wu 2006). The lower-level cyclonic circulation strengthens the moisture transport to the EASM region, thus reinforcing the precipitation. The establishment of SAH, one of the hallmarks of the larger-scale Asian monsoon, has a significant impact on the seasonal transition of the atmospheric circulation over the EASM areas and far-reaching influences over the entire northern hemisphere (Enomoto et al. 2003; Yanai and Wu 2006; Rodwell and Hoskins 2001).

Recent work, however, suggests that mechanical effects might be more important than traditionally thought: the subtropical westerly jet, whose core is still located on the high elevation terrain of the TP in late spring (Park et al. 2012a), induces a region of lower-level downstream convergence, which may be a primary driver of the EASM (work of Takahashi and Battisti, reported by Molnar et al. 2010). This hypothesis may explain why the demise of the MB in mid-July is concurrent with the northward jump of the subtropical westerly jet (as already identified in the late 50s, e.g., Dao and Chen 1957; Suda and Asakura 1955), in spite of increasing land-sea thermal contrast. While suggestive, the precise workings of this mechanism on the formation of the MB rainband have not been fully investigated.

In a recent observational study, Sampe and Xie (2010) called for a re-interpretation of the thermal influence of the TP on the EASM. In boreal summer, because of the elevated topography and latent heating due to monsoonal convection in South Asia, air over and south of the TP is warmer than the surrounding regions. The subtropical westerly jet that is still prevailing over the TP advects warm air from the southeastern TP to the MB region. The warm air advection provides a large-scale environmental forcing capable of maintaining the MB rainfall band even in the absence of diabatic terms. Such forcing can also steer weather disturbances, which favor vertical convection by intensifying lower-level moisture advection

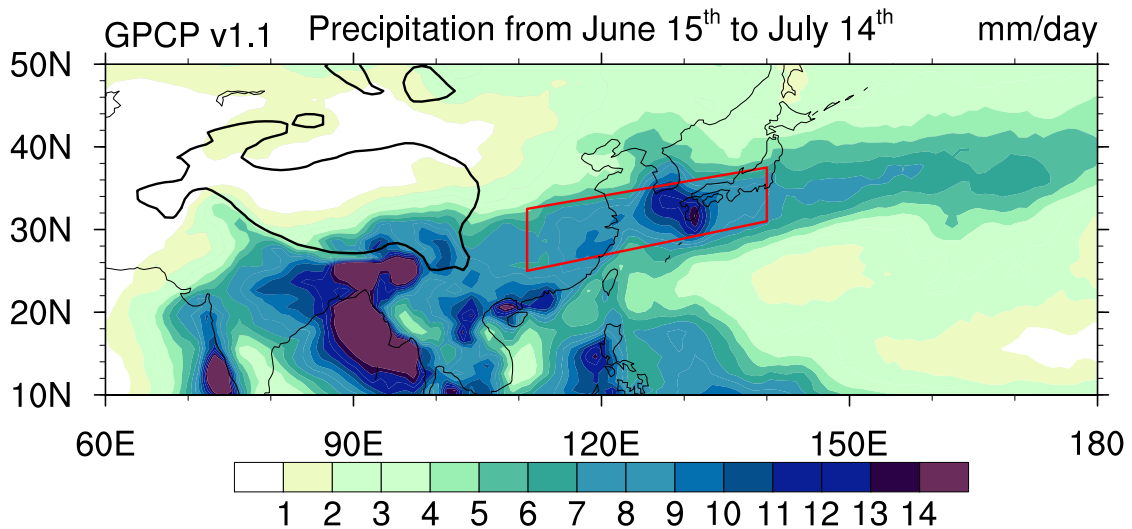


Figure 1.1 Climatological mean precipitation during the MB season. Bold black contour shows where orography intersects the 800 mb level.

with transient upward motion. As the jet stream rapidly jumps northward in mid-July (e.g., Schiemann et al. 2009), westerly flow and maximum mid-tropospheric temperatures are no longer colocated, causing the rapid weakening of the EASM rainfall band.

Following Sampe and Xie (2010), we define June 15 to July 14, May 16 to June 14, and July 15 to August 13 as the climatological MB, pre-MB, and post-MB seasons, respectively. During the MB season, a spatially well-organized rainfall band extends over East Asia and the northwestern Pacific (Fig. 1.1). The time evolution of the daily precipitation averaged over the MB region (Fig. 1.2a) shows a gradual increase from winter to late spring, and a sharp increase in mid-June, when the precipitation reaches its peak; around mid-July, the precipitation decreases rapidly and returns to values comparable to those in the pre-MB season. The MB also shows a large interannual variability in its duration and intensity which causes variations up to 20% (1σ variability) in precipitation during the MB season (Fig. 1.2b), far larger than that in the Indian summer monsoon (e.g., Krishnan et al. 2011).

The climatological conditions of the MB have been described at length in the literature (e.g., Ding and Chan 2005; Ninomiya and Murakami 1987; Sampe and Xie 2010) and here we only provide a brief summary, based on the most recent ERA-Interim product. Generally

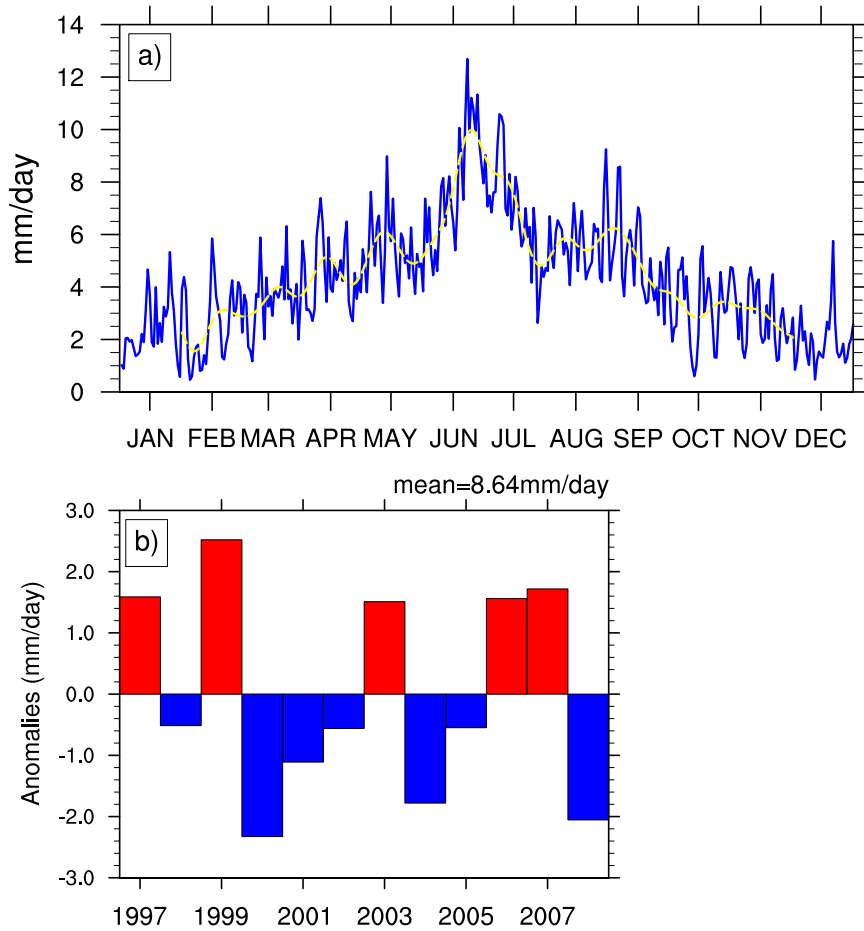


Figure 1.2 Climatology of the MB season from 1997 to 2009. a) Seasonal cycle of the precipitation averaged over the area enclosed by the red lines in Fig. 1.1, where precipitation is the largest. The blue and yellow lines show the daily mean precipitation and filtered precipitation by a low pass filter with a cutoff period of 20 days, respectively. The tick marks on the horizontal axis correspond to the middle of each month. b) Interannual precipitation anomaly over the enclosed region.

speaking, the MB rainfall is associated with pronounced lower-level moisture flux convergence (Fig. 1.3a) and wind convergence (Fig. 1.3c). A large meridional gradient of specific humidity (Fig. 1.3a) is present in both the Meiyu and the Baiu regions but a sharp meridional gradient of temperature (Fig. 1.3b) is only seen in the Baiu region and further downstream over the northwestern Pacific, which confirms that only the Baiu is associated with a lower-level baroclinic zone (e.g., Chen and Chang 1980; Ding 1992; Ding and Chan 2005). The importance of the zonal wind (i.e., the subtropical westerly jet) in the maintenance of the rainband has been strongly emphasized in the literature (e.g., Molnar et al. 2010; Sampe and

Xie 2010), while the role of the meridional wind has primarily been interpreted in association with the southerly moisture transport from tropical oceans. Here, we will argue for a more fundamental role of the meridional wind as an intrinsic component of the circulation response to the TP forcings and an essential element of the MB front. As evident in Fig. 1.3d, over the MB region the meridional wind is primarily from the south, advecting warm and moist air from the tropical oceans to support the MB rainfall band. The meridional wind convergence contributes significantly to the total horizontal convergence (Fig. 1.3c); in fact, the zonal winds diverge in the MB region primarily due to the interaction of the zonal wind and the TP.

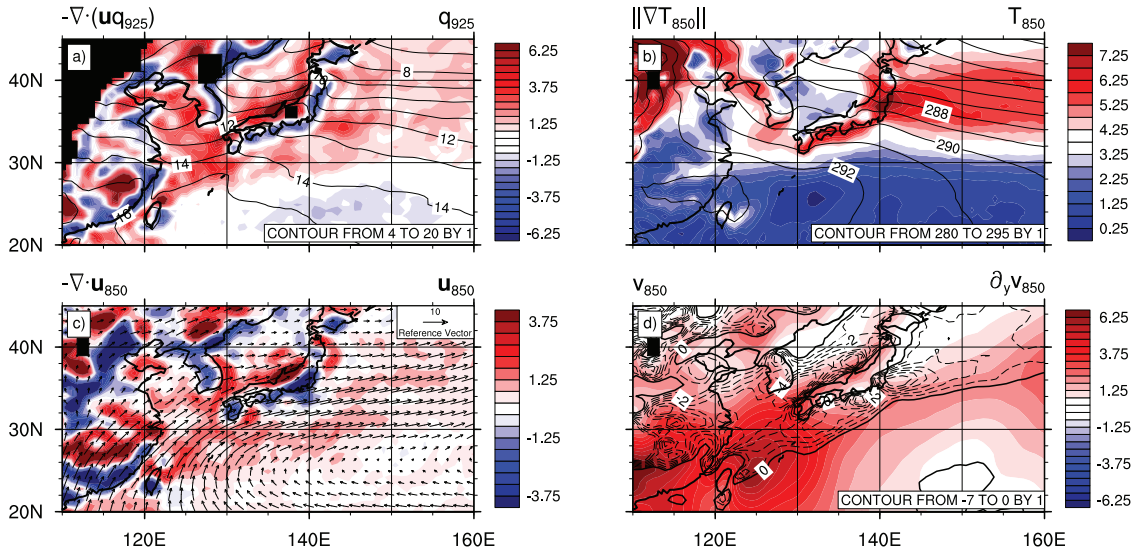


Figure 1.3 MB climatology. a) Moisture flux convergence (color contours, $\text{g kg}^{-1} \text{ day}^{-1}$) and near surface (925 mb) specific humidity (line contours, g kg^{-1}). b) Absolute value of lower-level (850 mb) temperature gradient (color contours, K (1000 km)^{-1}) and temperature (line contours, K). c) Lower-level (850 mb) wind convergence (color contours, 10^6 s^{-1}) and wind field (vector, m s^{-1}). d) Lower-level (850 mb) meridional wind (color contours, m s^{-1}) and meridional divergence (line contours, $\text{m s}^{-1}(\text{1000 km})^{-1}$).

1.2. Model spread

State-of-the-art Global Climate Models (GCMs) participating in the World Climate Research Programme (WCRP) Coupled Model Intercomparison Project Phase 3 (CMIP3) and CMIP5 have been shown to grossly capture the large-scale pattern of the EASM precipitation, but wide model-spread exists (Huang et al. 2013; Sperber et al. 2012; Song and Zhou 2013). While CMIP5 models have a slightly enhanced skill relative to CMIP3 in simulating the EASM climatological precipitation in terms of multi-model mean (MMM) (Sperber et al. 2012), significant biases in MMM rainfall amounts and spatial distribution remain. Fundamental issues related to the representation of basic physical processes in GCMs, such as moist convection (Bony et al. 2013b; Huang et al. 2013; Stevens and Bony 2013; Chen et al. 2010) and large-scale circulations (e.g., Ceppi et al. 2012; Huang et al. 2013), have been suggested to be the limiting factors in improved climate simulations, together with relatively coarse resolution, especially in regions with complicated topography like Asia (e.g., Boos and Hurley 2013). However, no study has yet provided a unified framework to reconcile the spread in present-day EASM simulations.

1.3. Future climate

It is well understood that the increase in global precipitation in response to greenhouse warming is energetically constrained rather than being limited by the availability of atmospheric water vapor (e.g., Mitchell et al. 1987; O’Gorman et al. 2012). Therefore, the global precipitation changes less rapidly with temperature (at around 2% K⁻¹ in current climate) than the change in water vapor in the atmosphere at around 7.5% K⁻¹ from the Clausius-Clapeyron relation (Held and Soden 2006). Changes in precipitation at the regional scale are more complex, and arguably more important than global changes, as circulation changes will affect the precipitation locally. Here, we explore regional changes in the EASM region,

in response to CO₂ forcing. Although it has been found that the rainfall during the EASM season is projected to increase at the end of the 21st century, limited understanding has prevented us from robustly identifying the physical and dynamical processes contributing to the change of the EASM and from better constraining the inter-model spread of EASM projections. Understanding how the EASM responds to a changing climate can provide support to theories of its maintenance in present-day climate and shed light into the dynamics and responses of other subtropical convergence zones to climate change.

The mechanisms that alter regional precipitation vary at different time scales. A fast response to an increase in CO₂ concentration before sea surface temperatures (SSTs) change occurs at short timescales and is associated with changes in large-scale wind patterns in the atmosphere. Large uncertainties in the precipitation change are found in the fast response, particularly over tropical oceanic regions, which are identified as a primary contributor to the inter-model spread in the difference in simulated precipitation between two equilibrium climate states (Bony et al. 2013a). A slow response to the subsequent increase in SSTs while maintaining the radiative forcing of CO₂ in the atmosphere is found to resemble the climatological precipitation pattern following observe the “wet get wetter” behavior (Held and Soden 2006).

The “wet get wetter” response captures the thermodynamic response of net rainfall over oceanic regions to SST forcing. Based on the assumptions of unchanged relative humidity and circulation, increases in atmospheric water vapor in a warmer climate intensify climatological convergence of water vapor fluxes. As a result, climatological wet regions (positive net precipitation regions) will become wetter. This simplified depiction has been generally accepted in the study of the response of the hydrological cycle to climate change; however, because of its assumptions, it does not capture the complexity of the thermodynamic precipitation response at the regional scale. For example, Xie et al. (2010) found that tropical rainfall change follows a “warmer get wetter” pattern modulated by future SST pattern, rather than the “wet get wetter” pattern, which can only be realized if SSTs are increased

uniformly.

While providing a useful starting point, the thermodynamic change due to SSTs is only one component of the total precipitation response. Dynamic changes in response to SST forcing have also been found to be important both globally and locally (e.g., Xie et al. 2010, 2009; He and Zhou 2015). Over the EASM region, dynamic changes have, for instance, shown to be associated with changes in the NPSH. Kitoh et al. (1997) found that global warming is associated with a strengthening and southward movement of the NPSH in a global climate model (GCM). Together with more El Niño-like patterns in future climates, it explains the mean sea-level pressure anomalies that might be related to the delay of Baiu withdrawal simulated in GCMs (Kitoh and Uchiyama 2006). The influence of tropical SST anomalies on the western NPSH has been vastly explored at the interannual timescale. It has been proposed that increases in rainfall over the tropical Indian Ocean due to the resulting warm SST anomalies from El Niño in the precedent year generate Kelvin waves emanating into the tropical western Pacific, inducing local northeasterly surface wind anomalies and resulting in an anticyclonic circulation over the western North Pacific (e.g., Yang et al. 2007; Xie et al. 2009). This signal can be enhanced by a cold tropical Pacific SST anomaly that generates anticyclonic Rossby waves to its northwestern region (e.g., Terao and Kubota 2005). This relationship between the western NPSH and the zonal SST gradient between the tropical Indian Ocean and the tropical Western Pacific is examined in RCP4.5 and RCP8.5 model outputs in CMIP5 by He and Zhou (2015). They found that this zonal temperature gradient has a robust influence on simulated western NPSH anomalies, which modulate the climate change over eastern China. In addition, they performed a sensitivity test on the impacts of tropical SST anomalies on the western NPSH, and they found that both the tropical Indian Ocean and tropical Western Pacific SST anomalies contribute to changes in the projected western NPSH intensity.

Mechanisms driven by changes other than just SSTs have, however, been invoked. Zhao et al. (2011a) investigated the tropical-North Pacific mode in present climate and found

that this mode is closely correlated with the variability of climate over Asia and the Pacific Ocean through Asian-Pacific Oscillation (APO). Sensitivity experiments emphasize the importance of the Asian land heating due to elevated topography (the TP) in generating summertime Asian-Pacific climate anomalies. Pacific SST forcing, seemingly important in this teleconnection, was suggested to play a much weaker role in the summertime Asian-Pacific atmospheric circulation. At interdecadal timescale, Zhao et al. (2011b) found that from a low-APO to a high-APO decade, both the upper-tropospheric SAH and the lower-tropospheric low pressure system intensify over Asia. This strengthened circulation results in anomalous southerly, southwesterly winds prevailing over the Asian monsoon region and leads to a strong northward transport of moisture and enhanced rainfall over the Asian monsoon region.

1.4. Goals of this dissertation work

In this thesis, I explore the fundamental dynamics of the EASM with the aim of unraveling dynamic and thermodynamic mechanisms that are implicated in 1) its current climatology, 2) its representation in present-day simulations by state-of-the-art climate models, and 3) its response to CO₂ forcing at different time scales. We frame our analyses of the current climatology of the EASM within the context of the moist static energy budget as observed in the European Center for Medium-Range Weather Forecasts (ECMWF) ERA-Interim products. Eddy decomposition of the advection terms in the MSE budget is used to expose the role of zonally asymmetric forcings in the energetics of the EASM system. Finally, we use numerical experiments with the Geophysical Fluid Dynamics Laboratory (GFDL) Atmospheric Model, version 2.1 (AM2.1, Anderson et al. (2004)) to explore the processes through which the TP influences the EASM rainfall formation.

We then use the theoretical understanding of the energetics of the EASM developed in part I to analyze model simulations from state-of-the-art climate models in the Coupled

Model Intercomparison Project Phase 5 (CMIP5). This allows us to expose processes contributing to the large inter-model spread of rainfall amount and spatial pattern of rainfall of EASM simulations based on our previous study of current climatology.

In the final part of this dissertation work, we use CMIP5 simulations to investigate the response of the EASM to atmospheric CO₂ forcing and subsequent sea surface warming within the context of the moisture budget. The relative role of the thermodynamic and dynamic contributions to the rainfall changes are examined. We use GFDL AM2.1 numerical experiments to further explore contributions from topography and surface warming pattern to rainfall changes.

Chapter 2

Energetics of the EASM system

Studies on the energetics of the EASM system date back to the late 80s, when latent energy advection was identified as a major energy source for the development and maintenance of the rainfall band over the MB region. However, a different mechanism has been recently proposed by Sampe and Xie (2010), who argue that mid-tropospheric warm air advection through the subtropical westerly jet provides a large-scale forcing, which is fundamental in triggering and maintaining the MB front even in the absence of diabatic forcing. In this view, advection of dry enthalpy, rather than latent energy, plays a key role. The work by Sampe and Xie (2010) is based on observational studies of the dry thermodynamic equation. Here, we extend their work to a comprehensive consideration of moisture, by framing our analyses within the context of the MSE and moisture budgets. As detailed below, this provides a more consistent view of the energetics of the EASM and allows us to highlight the role of zonally asymmetric circulations in the maintenance of the rainfall band.

2.1. Data and method

Precipitation data are from the Global Precipitation Climatology Project (GPCP) One-Degree Daily Precipitation Dataset (1DD) plotted over a $1^\circ \times 1^\circ$ latitude-longitude grid from 1997 to 2008 with daily temporal resolution (Huffman et al. 2001). All other data are from the European Center for Medium-Range Weather Forecasts (ECMWF) ERA-Interim products,

spanning the 20-year period from 1990 to 2009. Surface fluxes (latent heat and sensible heat) and radiation fluxes are from the ERA-Interim (1.5° grid, Dee et al. 2011) 3-hour-forecast fields produced from forecasts beginning at 0000 and 1200 UTC. Data on pressure levels, such as temperature, wind field, and humidity, are obtained from ERA-Interim reanalysis (37 pressure levels, 512×256 N128 Gaussian grid, analysis fields produced for 0000, 0600, 1200, 1800 UTC) in the Data Support Section of the National Center for Atmospheric Research (NCAR). The energy and radiation flux data are then converted to daily data, while data on pressure levels are analyzed at a 4×daily frequency to improve eddy statistics.

We use the reanalysis data to compute the MSE and moisture budgets for the EASM, and we perform a decomposition of all terms in the budgets into mean, stationary, and transient eddy components. To do so, we denote $(\cdot)'$ as the deviation from the monthly time mean $\overline{(\cdot)}$ for each individual year (e.g., $u' = u - \overline{u}$), and $(\cdot)^*$ as the deviation from the global zonal mean $[\cdot]$ (e.g., $u^* = u - [u]$). As detailed in Eq. 2.6, we thus decompose fluxes into mean, stationary, and transient eddy terms. Monthly total and eddy fluxes are computed for each year and then averaged over all available years to generate a 20-year long-term climatology. Based on the above definitions, transient eddies contain sub-monthly synoptic-scale variability, with longer-scale (timescale longer than a month) variability being captured by the stationary eddy terms.

2.2. Thermodynamic equation

Sampe and Xie (2010) investigated the large-scale dynamics of the MB in the context of the dry thermodynamic budget evaluated from the Japanese reanalysis (JRA-25), and argued that temperature advection from the southeastern flank of the TP at 500 mb is important in inducing vertical motion and positioning the MB front. The dry thermodynamic equation

in pressure coordinates is,¹

$$\overline{\partial_t T} = \overline{Q}/c_p - \frac{\overline{\omega}}{c_p} \overline{\partial_p s} - \overline{\mathbf{v}} \cdot \nabla_p \overline{T} - \frac{1}{c_p} \overline{\omega' \partial_p s'} - \overline{\mathbf{v}' \cdot \nabla_p T'}, \quad (2.1)$$

where Q is diabatic heating/cooling, c_p is the specific heat at constant pressure, $s = c_p T + gz$ is the dry static energy, \mathbf{v} is horizontal wind, T is temperature, z is geopotential height, and g is gravitational acceleration. $(\cdot)'$ denotes time deviations from the temporal mean $\overline{(\cdot)}$. Averaged over a climatological period, the heat storage on the left hand side can be neglected. Here, we briefly discuss the TD budget in the MB region based on Era-Interim data and compare our findings with those in Sampe and Xie (2010).

In the tropics, the leading order balance is between the vertical advection term (second term on the right hand side in Eq. 2.1) and the diabatic term, with smaller contribution from the horizontal temperature advection (the third term on the right hand side) because of weak temperature gradients (e.g., Sobel et al. 2001). However, in the MB region, especially over the Baiu region and the northwestern Pacific, horizontal advection becomes significant and provides warm air advection that well correlates with the vertical ascending motion (Fig. 2.1c,f; Sampe and Xie 2010). Both zonal and meridional components contribute to the overall pattern of warm air advection in the MB region, with the former dominating in the Meiyu region and the northwestern Pacific at lower latitudes (Fig. 2.1a,d), and the latter dominating in the Baiu region and the northwestern Pacific at higher latitudes (Fig. 2.1b,e). In partial agreement with Sampe and Xie (2010), we find that transient eddy fluxes are negligible in limited areas of the MB region but become more important further downstream over oceanic regions (Fig. 2.1i).

While the mid-tropospheric dry thermodynamic balance successfully explains the overall position of the MB rainfall band, it has the conceptual disadvantage of treating the diabatic term as a known forcing, which in fact influences and strongly depends on the circulation

¹Sampe and Xie (2010) write the thermodynamic equation in potential temperature. Here, we use temperature for notation consistency with Eq. 2.2, used to derive the moist static energy budget.

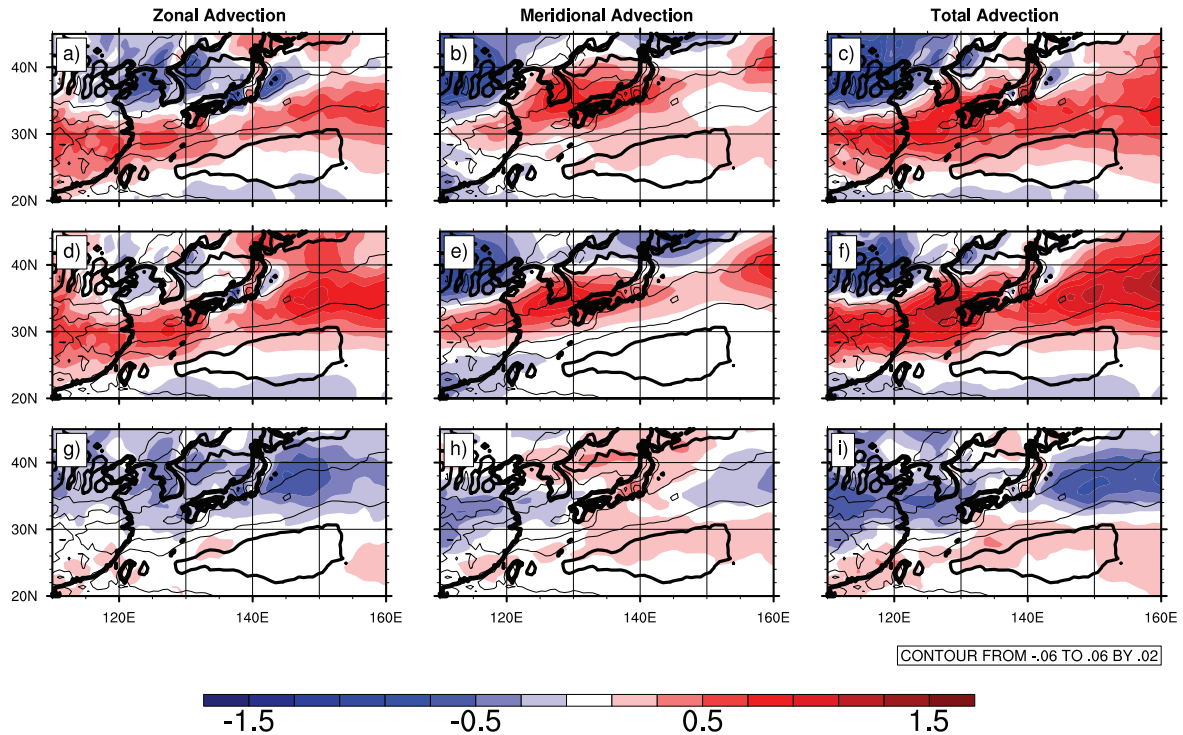


Figure 2.1 Mid-tropospheric temperature advection in the MB season. Columns show zonal (left), meridional (middle), and total (right) horizontal temperature advection. Rows show the total advection (top), the mean advection (middle), and the transient eddy term (bottom). In all panels, color contours indicate temperature advection (K day^{-1} , with warm/cold colors indicating warm/cold air advection) and line contours indicate the mid-tropospheric vertical velocity (Pa s^{-1} , with upward/downward motion in solid/dash contours and the zero contour thickened.)

itself. Even when used as a diagnostic tool from reanalysis data, it provides the challenge of estimating the non-readily available diabatic term as the residual of the thermodynamic budget, with results potentially dependent on the relatively coarse vertical resolution.

2.3. MSE budget

Previous work has emphasized the advantages of the MSE budget over the dry thermodynamic equation in studies of tropical-subtropical circulations in which comprehensive

effects of temperature, humidity, and diabatic processes are taken into consideration, and the interaction between moist convection and the circulation is accounted for (e.g., Chou and Neelin 2003; Neelin 2007). Following these studies, first we consider the vertically-integrated thermodynamic and moisture equations in pressure coordinates,

$$c_p \langle \partial_t T \rangle + c_p \langle \mathbf{v} \cdot \nabla T \rangle + \langle \omega \partial_p s \rangle = \langle Q_c \rangle + S^{net} + R^{net} + SH, \quad (2.2)$$

$$L_v \langle \partial_t q \rangle + L_v \langle \mathbf{v} \cdot \nabla q \rangle + L_v \langle \omega \partial_p q \rangle = \langle Q_q \rangle + LH, \quad (2.3)$$

where q is specific humidity and $\langle \cdot \rangle$ indicates a vertical mass integral (i.e., $\int \cdot dp/g$). The vertically-integrated change of internal energy and work done by the atmosphere is balanced by the energy fluxes at the boundaries of the atmospheric column, that is, the net shortwave radiation S^{net} , the net longwave radiation R^{net} and the sensible heat SH , and the convective heating Q_c . The vertically-integrated change of moisture in the atmospheric column is balanced by the evaporation LH/L_v and precipitation $-\langle Q_q \rangle/L_v$, where LH is the surface latent heat flux, Q_q is moistening and L_v is latent heat of vaporization. The sum of convective heating and moistening must be zero in the atmospheric column because precipitation $P = -\langle Q_q \rangle/L_v = \langle Q_c \rangle/L_v$.

The MSE balance in the atmospheric column is obtained by summing Eqs. 2.2 and 2.3 and averaging over a climatological period:

$$\overline{\left\langle \frac{\partial E}{\partial t} \right\rangle} = \overline{F^{net}} - \overline{\langle \mathbf{v} \cdot \nabla E \rangle} - \overline{\left\langle \omega \frac{\partial h}{\partial p} \right\rangle}, \quad (2.4)$$

and

$$F^{net} = S_t^\downarrow - S_t^\uparrow - S_s^\downarrow + S_s^\uparrow - R_t^\uparrow + R_s^\uparrow - R_s^\downarrow + SH + LH, \quad (2.5)$$

where $h = c_p T + gz + L_v q$ is the MSE, $E = c_p T + L_v q$ is the atmospheric moist enthalpy, and F^{net} is the net energy flux into the atmosphere, with the subscript t and s denoting the top of atmosphere and surface, respectively. The vertical advection of MSE is the column-integrated

product of vertical velocity in pressure coordinate ω and the MSE stratification $\partial_p h$, whose vertical integral in the troposphere is negative in pressure coordinates. Therefore, regions of positive vertical advection, where $\langle \overline{\omega \frac{\partial h}{\partial p}} \rangle > 0$, correspond to ascending vertical motion, and vice versa. That is, vertical motion can be inferred from the sum of the net energy flux into the atmospheric column and horizontal advection of moist enthalpy, provided that the storage term is negligible over a climatological period. In the tropics and over land, the vertical MSE advection is almost entirely balanced by the net energy flux; however, over oceans outside of the deep tropics, the horizontal advection of moist enthalpy is non-negligible and essential in maintaining vertical motions (Fig. 2.2). The horizontal moist enthalpy advection has also been shown to be critical in setting the poleward boundary of monsoonal convergence zones over subtropical continents (Chou and Neelin 2003; Neelin 2007). In the extra-tropics, where precipitation is primarily due to moisture transport along isentropes by large-scale baroclinic eddies, vertical motion is primarily along rather than across isentropes (which are parallel to isobars in the tropics), and the stratification (which determines the total gross moist stability) is dynamically determined (e.g., Schneider 2004), rather than thermodynamically constrained to follow a moist adiabat as it is in the tropics. Therefore the MSE budget in the extra-tropics provides weaker constraints on the circulation (e.g., Merlis and Schneider 2010). With these caveats in mind, the MSE budget as written in Eq. 4.1 does hold across latitudes and we will use it in the MB region to shed some light on its dynamics.

As discussed in previous studies (e.g., Chou and Neelin 2003), $\overline{F^{net}}$ is positive over land and most convective zones in tropical oceans but negative in extra-tropical oceans (Fig. 2.2, left). In boreal summer, the continents in the northern hemisphere receive high insolation extending to high latitudes. The outgoing longwave radiation depends largely on the upper-tropospheric temperature and cannot fully compensate the incoming insolation. The thermal inertia of land is very small, which results in a zero heat flux condition at the surface (Chou and Neelin 2003), whereas, over the oceans, the net flux into the surface can be

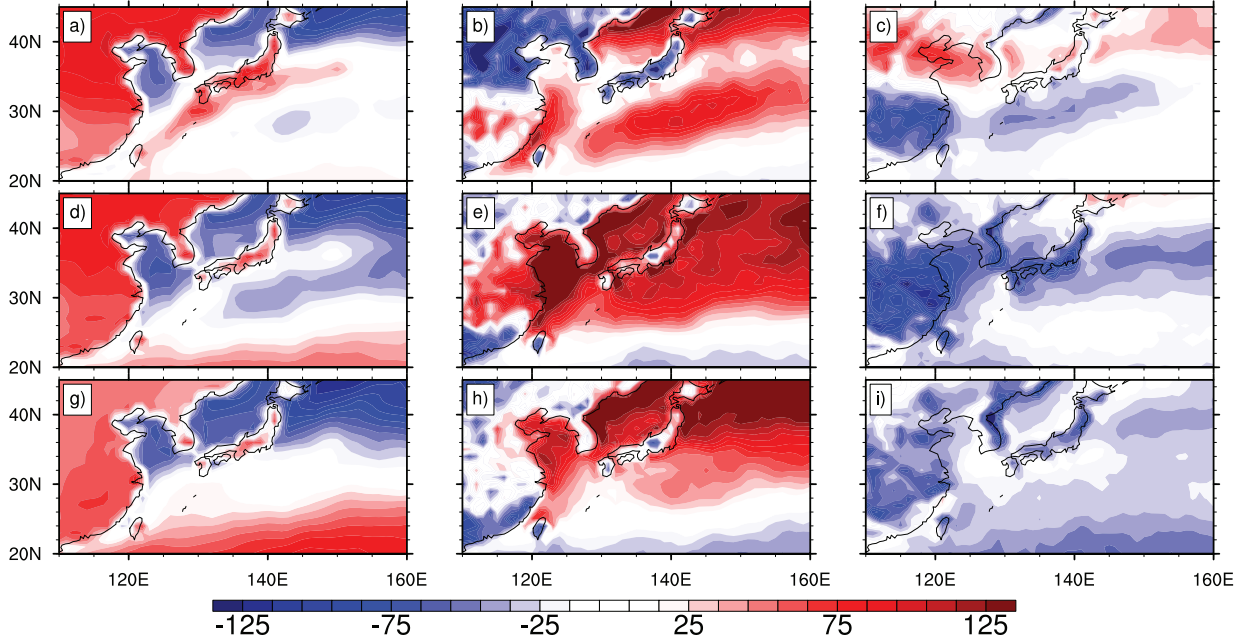


Figure 2.2 Vertically integrated MSE budget. Net energy flux into the atmospheric column $\overline{F^{net}}$ (left), vertical integral of horizontal moist enthalpy advection $-\langle \mathbf{v} \cdot \nabla E \rangle$ (middle), and vertical integral of vertical MSE advection $-\langle \omega \frac{\partial h}{\partial p} \rangle$ (right) for the pre-MB season (top), MB season (middle), and post-MB season (bottom). Contours are in W m^{-2} .

balanced by heat transport and heat storage, which in turn affects $\overline{F^{net}}$. As a result, $\overline{F^{net}}$ is positive over the northern hemisphere continents and convective oceanic regions in boreal summer. The horizontal advection of moist enthalpy tends to offset $\overline{F^{net}}$ in most regions (Fig. 2.2, middle). Over land and convective tropical oceans, the horizontal moist enthalpy advection is negative, indicating that moist enthalpy is transported away from regions of positive $\overline{F^{net}}$; however, over non-convective oceans and parts of the continents, the horizontal moist enthalpy advection is positive, indicating that moist enthalpy is transported into these regions of negative $\overline{F^{net}}$ from neighboring areas.

The vertical MSE advection in Fig. 2.2 (right) is obtained explicitly as the product of the MSE stratification, which is susceptible to the relatively coarse vertical resolution of the data used, and the vertical velocity. In our analysis, the MSE budget (Eq. 4.1) does

not close, resulting in a relatively small residual caused by insufficient vertical resolution, non-resolved sub-grid scale motions, and existing imbalances of atmospheric energy and mass in the reanalysis data from both the ERA forecast model and the assimilation system (Berrisford et al. 2011). In Fig. 2.3 (left) we show the vertical MSE advection computed as the difference between $\overline{F^{net}}$ and the horizontal moist enthalpy advection, which therefore includes the residual necessary to close the budget (note the opposite sign in Fig. 2.2, right and Fig. 2.3, left). Given that the MSE stratification is mostly negative in pressure coordinates, the vertical motion is qualitatively coupled to the vertical advection of MSE: ascending and descending motions are expected to occur where the sum of the net energy input and advective fluxes are positive and negative, respectively. This qualitative correspondence does not, however, imply a quantitative mapping, since the MSE stratification varies spatially. In the Baiu region and the northwestern Pacific Ocean, the fact that precipitation occurs in a region of otherwise negative net energy input into the atmospheric column invalidates the traditional tropical-subtropical balance in which ascending motion is correlated with positive net energy input into the atmospheric column. The horizontal moist enthalpy advection therefore plays an essential role in sustaining the MB rainfall band.

In the seasonal evolution of the EASM, both the net energy into the atmosphere and the horizontal moist enthalpy advection vary in location and intensity. In the pre-MB season, $\overline{F^{net}}$ is positive over continents and tropical oceans but decreases rapidly poleward over the oceanic regions (Fig. 2.2a). The horizontal moist enthalpy advection $-\langle \mathbf{v} \cdot \nabla E \rangle$ is prevalently negative and offsetting $\overline{F^{net}}$ in most continental and tropical regions, except over and to the east of the TP (Fig. 2.2b). The sum of these two terms is the vertical MSE advection (Fig. 2.2c or Fig. 2.3a), whose pattern resembles the precipitation pattern in the pre-MB season (Fig. 2.3d). The precipitation pattern, in turn, is spatially correlated with the pattern of horizontal moist enthalpy advection everywhere except over southeast China where vertical ascending motion is colocated with positive $\overline{F^{net}}$. To the north of the rainfall band, strong negative horizontal moist enthalpy advection is balanced by vertical descending mo-

tion. Over the oceans, precipitation occurs in regions of weak energy flux but strong positive horizontal moist enthalpy advection; however, the horizontal moist enthalpy advection cannot balance the strong negative energy flux in the mid-latitudes, resulting in an unfavorable region for convection.

During the MB season, the energy flux (Fig. 2.2d) decreases in the MB region and the northwest Pacific Ocean, mainly because of increased reflection of insolation due to increased cloud cover and decreased latent heat flux over oceanic regions. In the tropical and subtropical oceans, however, as the SSTs continue to increase, evaporation from the ocean increases accordingly, resulting in an increase in net energy input into the atmospheric column. Nevertheless, convection is not favored to the south of the MB region despite higher SST values (Sampe and Xie 2010, Fig. 2.3e). Sampe and Xie (2010) attribute this preference of convection over the northwest Pacific Ocean with lower SSTs to the combined effect of the mid-tropospheric warm air advection and weather disturbances steered by the subtropical westerly jet. In the framework of the MSE budget, this preference is largely governed by the horizontal moist enthalpy advection: to the south of the MB region, regardless of higher SSTs, the net energy is weak and cannot trigger convection; the horizontal moist enthalpy advection is large over the northwestern Pacific while hardly affecting or even suppressing convection in the subtropical ocean. The MB rainfall band, similar to what is seen in the pre-MB season, is primarily sustained by the horizontal moist enthalpy advection, with its overall structure and location resulting from both the net energy input and the horizontal moist enthalpy advection (Fig. 2.2f or Fig. 2.3b). In addition, over the Meiyu region, the horizontal moist enthalpy advection is positive before and during the MB season, but becomes negligible in the post-MB season.

In the post-MB season, the net energy flux over the ocean increases in tropical and subtropical latitudes but decreases in the mid-latitudes. Over the continents, it decreases in most regions (Fig. 2.2g). The horizontal moist enthalpy advection displaces poleward and becomes less intense, resulting in a sharp reduction in horizontal moist enthalpy advection

over the MB region but a slight increase to both its south and north (Fig. 2.2h). As a result, the MB region is less favored energetically and a bifurcation of the vertical MSE advection is formed to the south and north of the MB region (Fig. 2.2i or Fig. 2.3c). This pattern of vertical MSE advection explains the suppression of rainfall and revival of convection over the subtropical northwestern Pacific during and after the MB season: during the MB season, despite high SSTs, strong negative horizontal moist enthalpy advection is balanced by descending motions in this region; after the MB season, the increase in net energy flux into the atmosphere combined with a reduction in negative horizontal moist enthalpy advection provides a favorable environment for the development of convection (Fig. 2.3f).

The similarity between the vertical MSE advection and the precipitation pattern in the three subsequent seasons using two independent datasets (Fig. 2.3, left, right) gives us confidence in the validity of using the MSE framework to study the climatology and seasonality of the EASM.

2.4. Energy advection decomposition

During the MB season, both $\overline{F^{net}}$ and horizontal moist enthalpy advection are important in sustaining the rainfall in the Meiyu region; however, in the Baiu region and northwestern Pacific, energy input into the atmosphere is negative, and the horizontal moist enthalpy advection alone sustains the rainfall. Given that the horizontal moist enthalpy advection plays an essential role in positioning the stationary MB rainfall band, heuristically we expect the stationary eddy fluxes to be the dominant terms in the horizontal moist enthalpy advection. Here, we decompose the horizontal moist enthalpy advection into mean, transient, and stationary eddy fluxes. As explained in Section 1 Data and Method, $(\cdot)'$ and $(\cdot)^*$ denote deviations from the time $\overline{(\cdot)}$ and zonal $[\cdot]$ mean, respectively. Hence, the time mean

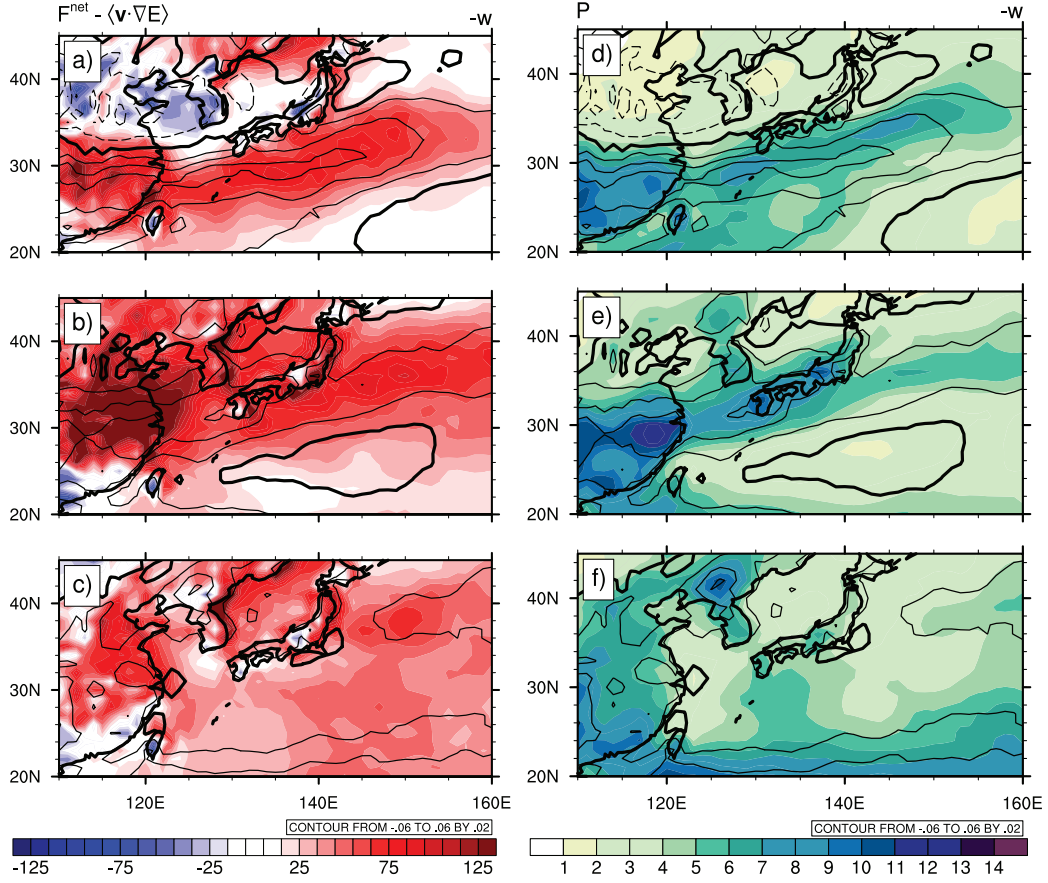


Figure 2.3 Vertical MSE advection computed as $\overline{F^{net}} - \langle \mathbf{v} \cdot \nabla E \rangle$ (color contours, W m^{-2} , left) and GPCP climatological mean precipitation (color contours, mm day^{-1} , right). Rows are the same as in Fig. 2.2. In all panels, line contours show vertical velocity (Pa s^{-1} , contour interval 0.02 Pa s^{-1}), with upward/downward motion in solid/dash contours and the zero contour thickened.

advection of the atmospheric energy $\langle \mathbf{v} \cdot \nabla E \rangle$ can be written as

$$\langle \mathbf{v} \cdot \nabla E \rangle = \langle [\bar{\mathbf{v}}] \cdot [\nabla E] \rangle + \langle [\bar{\mathbf{v}}] \cdot \nabla E^* \rangle + \langle \mathbf{v}^* \cdot [\nabla E] \rangle + \langle \mathbf{v}^* \cdot \nabla E^* \rangle + \langle \mathbf{v}' \cdot \nabla E' \rangle. \quad (2.6)$$

The first term on the right side is the zonal-mean energy advection by the zonal-mean flow; the second term is the advection of the stationary eddy energy by the zonal-mean flow; the third term is the advection of the zonal-mean energy by the stationary eddy velocity; the fourth term is the advection of the stationary eddy energy by the stationary eddy velocity; the fifth term is the advection of the transient eddy energy by the transient eddies.

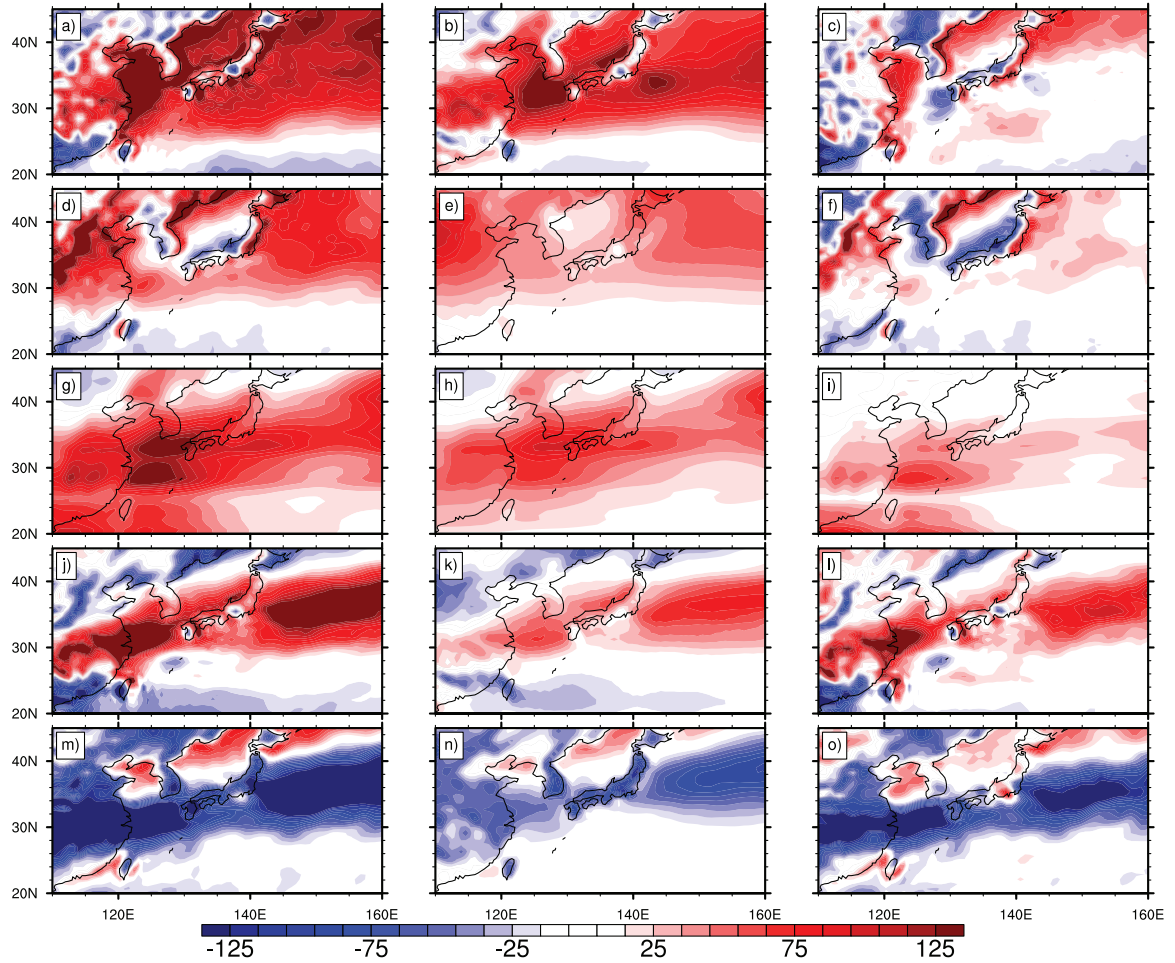


Figure 2.4 Eddy decomposition of the vertical integral of the horizontal moist enthalpy advection $-\langle \mathbf{v} \cdot \nabla E \rangle$ (left), the horizontal dry enthalpy advection $-\langle c_p \mathbf{v} \cdot \nabla T \rangle$ (middle), and the latent energy advection $-\langle L_v \mathbf{v} \cdot \nabla q \rangle$ (right) during the MB season. Rows indicate the total advection $-\langle \mathbf{v} \cdot \nabla(\cdot) \rangle$ (a,b,c), the advection of the stationary eddy energy by the zonal-mean flow $-\langle [\bar{\mathbf{v}}] \nabla(\cdot)^* \rangle$ (d,e,f), the advection of the zonal-mean energy by the stationary eddy velocity $-\langle \mathbf{v}^* [\nabla(\cdot)] \rangle$ (g,h,i), the advection of the stationary eddy energy by the stationary eddy velocity, or pure stationary eddy $-\langle \mathbf{v}^* \nabla(\cdot)^* \rangle$ (j,k,l), and the advection of the transient eddy energy by the transient eddy velocity $-\langle \mathbf{v}' \cdot \nabla(\cdot)' \rangle$ (m,n,o). Contours are in W m^{-2} .

The zonal-mean term $\langle [\bar{\mathbf{v}}] \cdot [\nabla E] \rangle$ is very small compared to the other terms and can be neglected (not shown). All other terms are shown in Fig. 2.4 (left), together with separate contributions by the dry enthalpy (Fig. 2.4, middle) and latent energy (Fig. 2.4, right). Comparing the horizontal dry enthalpy advection and latent energy advection on the MB region during the MB season, we find that the dry enthalpy component tends to dominate

in the core of the MB region, with the latent energy advection becoming important only over the midlatitude ocean. Previous evaluations based on observational and numerical studies argued latent energy advection through the lower-level southwesterly transport of moisture from the tropical oceans, including the Bay Of Bengal (BOB), the SCS, and the western Pacific, to be the major source of energy for the development and maintenance of the rainfall band over the MB region (e.g., Ninomiya and Murakami 1987; Kuo et al. 1986; Wang 1987; Wang et al. 1993). However, our analysis de-emphasizes the importance of moisture advection as an energy supply and confirms that the MB rainfall band, from a large-scale perspective, is mainly the result of dry enthalpy advection (Sampe and Xie 2010). As we have identified the horizontal dry enthalpy advection as the main component in the horizontal moist enthalpy advection, we now focus on its eddy fluxes and assess their relative contributions to the moist enthalpy advection.

The total dry enthalpy advection results from the advection of the stationary eddy dry enthalpy by the zonal-mean flow $-\langle [c_p \bar{\mathbf{v}}] \cdot \overline{\nabla T^*} \rangle$ (Fig. 2.4e), the advection of the zonal-mean dry enthalpy by the stationary eddy velocity $-\langle c_p \bar{\mathbf{v}}^* \cdot \overline{[\nabla T]} \rangle$ (Fig. 2.4h), the pure stationary eddy flux $-\langle c_p \bar{\mathbf{v}}^* \cdot \overline{\nabla T^*} \rangle$ (Fig. 2.4k) and the transient eddy flux $-\langle c_p \bar{\mathbf{v}}' \cdot \overline{\nabla T'} \rangle$ (Fig. 2.4n). All the three stationary eddy fluxes have positive dry enthalpy advection into the MB region and the northwestern Pacific; however, the transient eddy flux, which is expected to diverge atmospheric energy away from the subtropics into higher latitudes, has the opposite sign in the MB region. The first two terms, $-\langle [c_p \bar{\mathbf{v}}] \cdot \overline{\nabla T^*} \rangle$ and $-\langle c_p \bar{\mathbf{v}}^* \cdot \overline{[\nabla T]} \rangle$, vanish when one takes the global zonal mean, but represent stationary eddy-mean flow interactions, which locally are of primary importance. The pure stationary eddy flux and the transient eddy flux are comparable in magnitude to the other two stationary eddy fluxes, but they appear to have similar spatial patterns of opposite sign, such that their combined contribution to the total dry enthalpy advection over the overall MB region and the northwestern Pacific is negligible. This is even more evident if we look at the zonal and meridional components of dry enthalpy advection (not shown), which are dominated by $-\langle [c_p \bar{\mathbf{v}}] \cdot \overline{\nabla T^*} \rangle$ and $-\langle c_p \bar{\mathbf{v}}^* \cdot$

$[\overline{\nabla T}]$), respectively, with a negligible contribution from the corresponding components of the pure stationary and transient fluxes. While we still do not understand to what extent this cancellation might be a coincidence or an intrinsic feature of the EASM, we also observe it in the numerical simulations discussed in the next section. For this reason, in the following we primarily focus on the two stationary eddy fluxes that depend on stationary eddy-mean flow interactions, that is, the advection of the stationary eddy dry enthalpy by the zonal-mean flow, $-\langle [c_p \overline{\mathbf{v}}] \cdot \overline{\nabla T^*} \rangle$, and the advection of the zonal-mean dry enthalpy by the stationary eddy velocity, $-\langle c_p \overline{\mathbf{v}^*} \cdot [\overline{\nabla T}] \rangle$.

The $[\overline{\mathbf{v}}] \cdot \overline{\nabla T^*}$ term is approximately equal to the product of the zonal mean zonal wind $[\overline{u}]$ and the longitudinal stationary thermal gradient due to zonal asymmetries $\partial_x \overline{T^*}$. The $\overline{\mathbf{v}^*} \cdot [\overline{\nabla T}]$ term is equal to the product of the meridional stationary eddy velocity $\overline{v^*}$ and zonal mean meridional temperature gradient $[\partial_y \overline{T}]$. The zonal mean zonal wind and the zonal mean meridional temperature gradient are primarily determined by the global energy and momentum budgets and barely affected by local forcings, especially in Northern Hemisphere summer (cf. Peixoto and Oort 1992). Hence, the presence of the TP will not influence zonal mean quantities but will be primarily manifest in the local longitudinal thermal gradient due to zonal asymmetries $\partial_x \overline{T^*}$ and the meridional stationary eddy velocity $\overline{v^*}$.

The zonal gradient of the stationary temperature term $\partial_x \overline{T^*}$ is due to the land-sea thermal contrast and the TP thermal effects. Given that during the MB season, the predominant winds are still eastward, both locally over the TP and the MB region and in the zonal average at these latitudes, the land-sea differential heating results in warm air advection in the downstream of the TP. Such inhomogeneous heating is reinforced by the presence of the TP, which is heated up rapidly during the spring and summer. The factor $[\overline{u}] \partial_x \overline{T^*}$ is the backbone of the theory in Sampe and Xie (2010), in which the advection of warm air from the TP to the MB region is argued to be the major forcing of the MB rainfall system. The presence of the TP can also contribute to the meridional stationary eddy velocity $\overline{v^*}$ in its downstream by both thermal and mechanical effects. The thermal effect can drive lower-level

cyclonic circulation around the TP, which enhances the southerlies in the MB region. The mechanical interaction between the subtropical westerly jet and the TP induces a region of lower-level convergence in its downstream, with southerlies to the south and northerlies to the north of the MB region.

In the zonal mean, transient and stationary eddy fluxes are the primary means by which energy is transported poleward in the extra-tropics to satisfy the global energy budget. Zonal asymmetries can create regions of enhanced and suppressed eddy transport through local effects. For instance, in a recent work, Kaspi and Schneider (2013) showed that a zonally asymmetric surface heating in an otherwise uniform slab ocean can shape storm tracks by modulating local baroclinicity through stationary fluxes. In the MB region, the local moist enthalpy advection arises, as shown by our analysis above, because of zonal asymmetries due to both land-sea contrast and the TP. The precise role of the TP in the local moist enthalpy advection, which cannot be assessed by means of observations only, will be more systematically explored using numerical simulations in Chapter 3.

2.5. Moisture budget

The distribution of the net precipitation in the MB rainfall needs to satisfy the moisture budget:

$$\langle \overline{\partial_t q} \rangle + \langle \overline{\nabla \cdot (\mathbf{v}q)} \rangle + \langle \overline{\partial_p(wq)} \rangle = -\overline{P} + \overline{E}. \quad (2.7)$$

Averaged over a climatological period, the tendency term $\langle \overline{\partial_t q} \rangle$ and the vertical term $\langle \overline{\partial_p(wq)} \rangle$ can be neglected (not shown). The convergence of moisture flux $-\langle \overline{\nabla \cdot (\mathbf{v}q)} \rangle$ can be decomposed into the moisture advection $-\langle \overline{\mathbf{v} \cdot \nabla q} \rangle$ and the product of moisture and wind convergence $-\langle \overline{q \nabla \cdot \mathbf{v}} \rangle$. In most of the MB region, particularly over the oceanic regions, surface evaporation is limited (Fig. 2.5b) and the moisture flux convergence (Fig. 2.5a) plays a more dominant role in water vapor supply. Further decomposition indicates that the moisture flux convergence primarily arises from the wind convergence (Fig. 2.5c) over the

MB region, whereas moisture advection becomes dominant in mid-latitude oceanic regions (Fig. 2.5d), consistent with the results discussed in the previous section.

As we did for the MSE budget, we decompose $-\overline{q\nabla\cdot\mathbf{v}}$ into mean ($-\overline{[\bar{q}][\nabla\cdot\mathbf{v}]}$), stationary ($-\overline{q^*[\nabla\cdot\mathbf{v}]}$, $-\overline{[\bar{q}]\nabla\cdot\mathbf{v}^*}$, $-\overline{q^*\nabla\cdot\mathbf{v}^*}$) and transient eddy fluxes ($-\overline{q'\nabla\cdot\mathbf{v}'}$). The dominant term is $-\overline{[\bar{q}]\nabla\cdot\mathbf{v}^*}$ (Fig. 2.6a), while the zonal asymmetries due to water vapor are negligible (Fig. 2.6b). As argued above, the presence of the TP will primarily impact stationary quantities, including the stationary eddy convergence term $-\overline{\nabla\cdot\mathbf{v}^*}$. The pure stationary eddy flux $-\overline{q^*\nabla\cdot\mathbf{v}^*}$ is comparable to the $-\overline{[\bar{q}]\nabla\cdot\mathbf{v}^*}$ term over the Meiyu region, but becomes negligible over the Baiu and oceanic regions (Fig. 2.6c). The transient eddy flux $-\overline{q'\nabla\cdot\mathbf{v}'}$ plays only a minor role.

The results discussed so far identify the longitudinal thermal gradient due to zonal asymmetries $\partial_x\overline{T^*}$ and the meridional stationary eddy velocity $\overline{v^*}$ as important dynamical factors

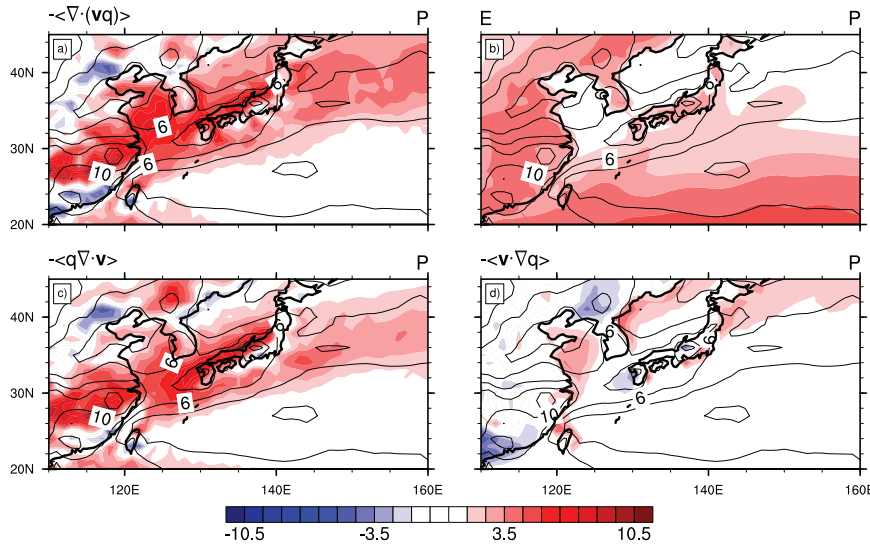


Figure 2.5 Moisture budget for the MB season. a) Vertically integrated moisture flux convergence $-\langle\nabla\cdot(\mathbf{v}q)\rangle$. b) Evaporation E . c) Product of moisture and wind convergence $-\langle q\nabla\cdot\mathbf{v}\rangle$. d) Moisture advection $-\langle\mathbf{v}\cdot\nabla q\rangle$. Units are mm day^{-1} . Line contours are precipitation with interval 1 mm day^{-1} .

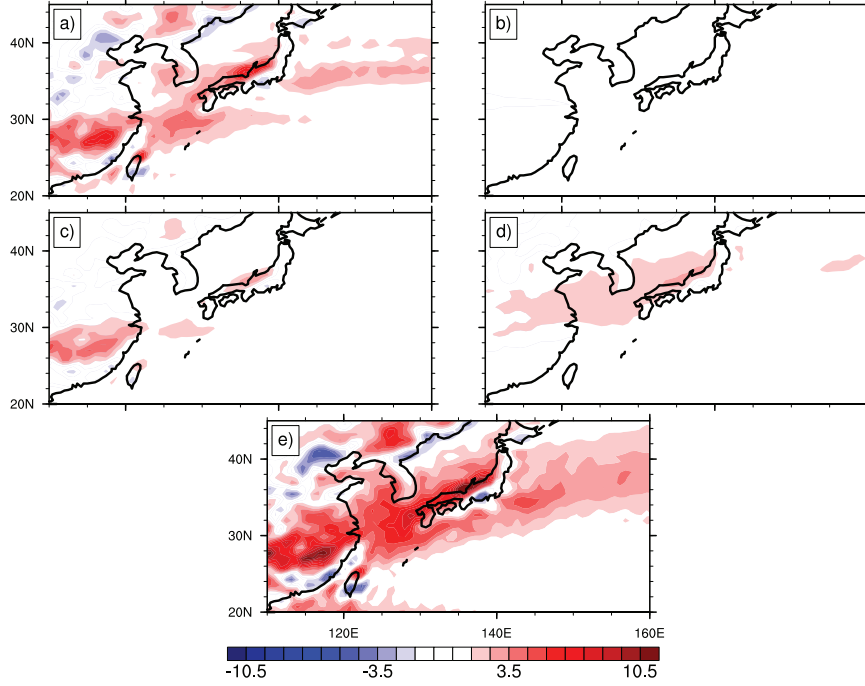


Figure 2.6 Eddy decomposition of the vertical integral of the the product of moisture and wind convergence $-\langle q \nabla \cdot \mathbf{v} \rangle$ (e) into the product of the stationary eddy convergence and the zonal-mean specific humidity $-\langle [\bar{q}] \nabla \cdot \mathbf{v}^* \rangle$ (a), the product of the zonal-mean flow convergence and the stationary specific humidity $-\langle \bar{q}^* [\nabla \cdot \mathbf{v}] \rangle$ (b), the product of the stationary eddy convergence and the stationary specific humidity or pure stationary eddy $-\langle \bar{q}^* \nabla \cdot \mathbf{v}^* \rangle$ (c), and the product of the transient flow convergence and the transient specific humidity $-\langle q' \nabla \cdot \mathbf{v}' \rangle$ (d) during the MB season. Contours are in W m^{-2} .

implicated in the MB formation. In the next section, we perform numerical simulations with the AM2.1 AGCM to explore how the presence or absence of the TP affects the MB rainfall through these exposed factors.

2.6. Conclusions

We have used the MSE and moisture budgets in observations to identify large-scale mechanisms controlling the development and seasonality of the EASM. Novel results emerging from this study include:

- Positive horizontal moist enthalpy advection, and primarily dry enthalpy advection, sustains the MB rainfall band in a region of otherwise negative net energy input into the atmosphere;
- The zonal thermal gradient due to zonal asymmetries $\partial_x \overline{T^*}$ and the meridional stationary eddy velocity $\overline{v^*}$ are the dominant stationary terms creating the pattern of total dry enthalpy advection in the MB region;
- The largest contribution to the moisture flux convergence sustaining the MB rainfall arises from stationary eddy convergence $-\overline{\nabla \cdot \mathbf{v}^*}$.

In the next chapter, we leverage numerical experiments to disclose the mechanisms through which the TP affects the EASM formation within the theoretical framework of the MSE budget.

Chapter 3

Orographic effect of the TP on the EASM formation

The observational analyses presented in Chapter 2 highlight the importance of the horizontal advection of moist enthalpy in the energetics of the EASM system. The further decomposition into mean and eddy terms identifies the stationary eddy-mean flow terms as playing a dominant role in controlling the overall pattern of the horizontal moist enthalpy advection. These terms involve zonal asymmetries in both the zonal temperature gradient and the meridional velocity, which are influenced by zonally asymmetric forcing such as that provided by the TP. Observational analyses alone, however, cannot allow for an assessment of the precise role the TP plays in shaping these terms. Hence, we perform numerical experiments in which the TP is retained or removed to more systematically examine its on the EASM formation.

3.1. Data and method

Numerical simulations are performed with the AM2.1 AGCM developed at the Geophysical Fluid Dynamics Lab (GFDL, Anderson et al. 2004). AM2.1 uses a finite-volume dynamical core (Lin 2004) with $2.5^\circ \times 2.0^\circ$ horizontal resolution and 24 vertical levels. Climatologically fixed SSTs from monthly mean Reynolds SST analysis are used as boundary condition (Smith et al. 1996). Two different model integrations are performed with different

topography over Asia, one where full topography at present-day height is retained (control) and one where the TP and Himalaya mountains are removed (experiment). More specifically, in the no-TP experiment, the entire TP and Central Asian mountains from 45° to 125°E and from 28° to 55°N are reduced by 95%. The experiments are the same as those described in Park et al. (2012a). Climatological mean winds, temperature, and geopotential height fields obtained from the control run are used as the initial conditions in the experiment run. Each experiment ran for 19 years, and the last 12 years of the simulations are used for the analysis.

Previous studies have shown that the presence of the TP causes changes in the SSTs in the surrounding oceanic regions, which have an impact on the evolution of the EASM in addition to the direct effects from the TP (Abe et al. 2004; Kitoh 2004). However, in this paper, we focus on the direct effects of the TP on the EASM and leave examination of possible indirect effects through SST changes to future studies.

3.2. Numerical simulations

Here, we analyze the AM2.1 control simulation and the experiment simulation to explore the role of the TP on the existence of the EASM. The control experiment simulates reasonably well the seasonal evolution of the EASM (Fig. 3.1). However, the model underestimates the precipitation over the MB region, possibly because of coarse resolution and deficiencies in the convective parameterization.¹ When the TP is removed, the MB rainfall almost disappears and oceanic precipitation in the deep tropics slightly increases. This confirms that the TP plays a fundamental role in the existence of the EASM, in agreement with previous studies (e.g., Kitoh 2004; Park et al. 2012a; Wu et al. 2012).

Fig. 3.2 shows the precipitation distribution and the vertical MSE advection calculated

¹In the AM2.1 control simulation, the MB season is anticipated by around 30 days. Here, we define the MB season in the control simulation as the 30 days in which the precipitation over the MB region reaches its maximum.

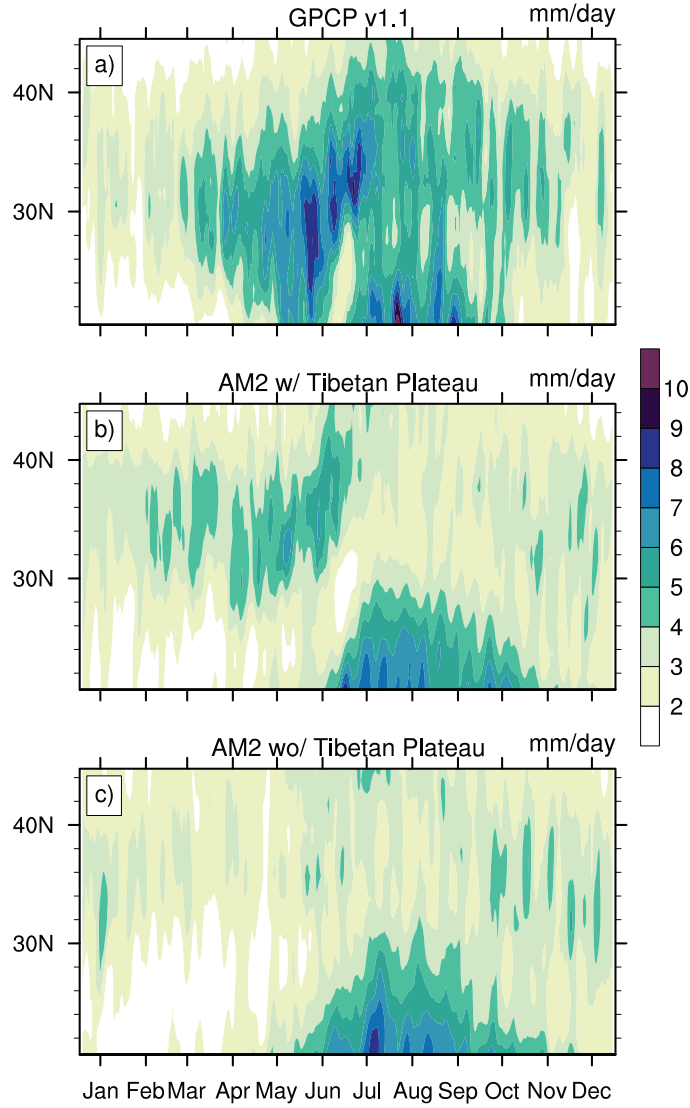


Figure 3.1 Hovmöller plot of precipitation averaged from 110°E to 160°E in GPCP v1.1 (a), AM2.1 simulations with the TP (b) and without the TP (c).

as the difference between $\overline{F^{net}}$ and horizontal moist enthalpy advection in the control run and experiment run. The precipitation is strongly coupled with mid-tropospheric vertical velocity, which is highly correlated with the vertical MSE advection. In the presence of the TP, a tilted, intensified rainfall band expands across the MB region and to the northwestern Pacific. In the absence of the TP, however, the precipitation over the MB region is significantly weakened and sparsely distributed. The suppression of precipitation over higher SST regions is not observed in the absence of the TP. The similarity between the precipitation

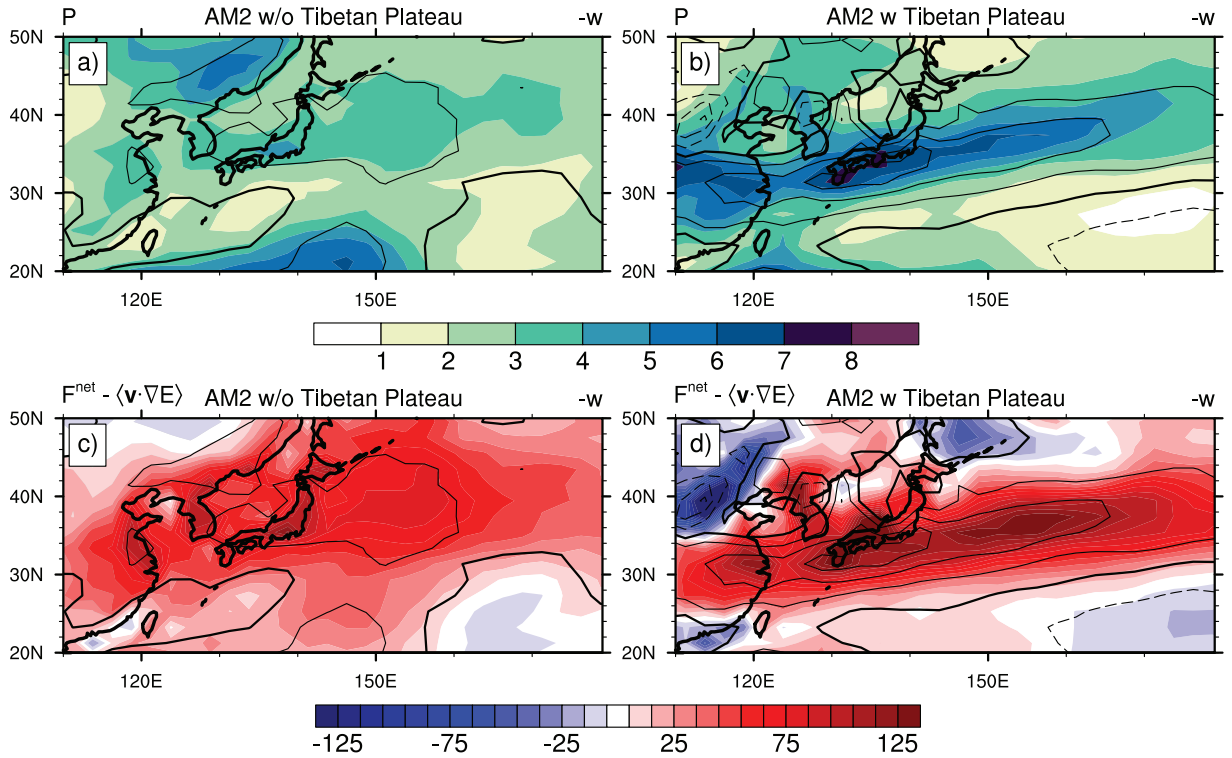


Figure 3.2 Precipitation (upper, color contours, mm day⁻¹) and vertical MSE advection (bottom, color contours, W m⁻²) of AM2.1 integration with the TP (right) and without the TP (left) during the MB season. Line contours indicate vertical ascending velocity (Pa s⁻¹, contour interval 0.02 Pa s⁻¹) at 500 mb.

pattern and the vertical MSE advection further confirms the feasibility of our framework in capturing the precipitation in the MB season.

The difference between the experiment run and control run in the vertical MSE advection mainly results from changes in horizontal moist enthalpy advection rather than changes in net energy flux over the MB region (not shown). The change in horizontal moist enthalpy advection is dominated by changes in the horizontal dry enthalpy advection, with smaller or opposite signed changes in latent energy advection (Fig. 3.3a,b). The presence of the TP creates a narrow and titled band of positive dry enthalpy advection in its downstream, highly resembling the rainfall pattern. Strong negative advection, which is balanced by descending motion, appears to the north and south of the positive advection zone.

Performing the same decomposition of the dry enthalpy advection in mean and eddy terms as the one presented in Section 4c, we find that the main contribution to the total dry enthalpy advection (Fig. 3.3a) arises from the advection of the zonal mean dry enthalpy by stationary eddies $-\langle c_p \overline{\mathbf{v}^*} \cdot [\overline{\nabla T}] \rangle$ (Fig. 3.3d). Interestingly, the advection of the stationary eddy dry enthalpy by the zonal-mean flow $-\langle c_p [\overline{\mathbf{v}}] \cdot \overline{\nabla T^*} \rangle$ (Fig. 3.3c) only exerts a minor and relatively local influence over the near downstream of the TP. Similar changes occur in the mid-tropospheric warm air advection at 500 mbar (not shown). This result shows that local heating over the TP, which reinforces the land-sea thermal contrast, and hence the longitudinal temperature gradient, only impacts the near downstream of the TP, leaving the Baiu region and the northwestern Pacific largely unaffected. However, the presence of the TP, through both its mechanical effect and changes in the circulation due to the thermal effect, influences the meridional stationary eddy velocity and helps sustain the MB rainfall band. The pure stationary eddy flux and the transient eddy flux both increase in magnitude in the presence of the TP (Fig. 3.3e,f), but their combined contribution to the total dry enthalpy advection remains negligible.

To further expose the role of the TP in determining patterns of dry enthalpy advection necessary to maintain the MB front, we compute the anomalous advection of the mean dry enthalpy by stationary eddies as the difference between the control $(\overline{\mathbf{v}^*}_c \cdot [\overline{\nabla T}]_c)$ and experiment $(\overline{\mathbf{v}^*}_e \cdot [\overline{\nabla T}]_e)$ simulations and we further partition it in such way that

$$\langle \delta(\overline{\mathbf{v}^*} \cdot [\overline{\nabla T}]) \rangle = \langle \delta \overline{\mathbf{v}^*} \cdot [\overline{\nabla T}]_e \rangle + \langle \overline{\mathbf{v}^*}_e \cdot \delta[\overline{\nabla T}] \rangle + \langle \delta \overline{\mathbf{v}^*} \cdot \delta[\overline{\nabla T}] \rangle, \quad (3.1)$$

where $\delta(\cdot)$ is defined as the difference between the experiment with the TP and without the TP, i.e. $\delta(\cdot) = (\cdot)_c - (\cdot)_e$, where the subscript c and e denote the experiment with the TP and without the TP, respectively. The result (not shown) indicates that the total difference $\langle \delta(\overline{\mathbf{v}^*} \cdot [\overline{\nabla T}]) \rangle$ is almost entirely due to changes in \mathbf{v}^* , $\langle \delta \overline{\mathbf{v}^*} \cdot [\overline{\nabla T}]_e \rangle$, while the difference in the zonal mean temperature gradient, $[\overline{\nabla T}]$ in $\langle \overline{\mathbf{v}^*}_e \cdot \delta[\overline{\nabla T}] \rangle$, and co-variation $\langle \delta \overline{\mathbf{v}^*} \cdot \delta[\overline{\nabla T}] \rangle$

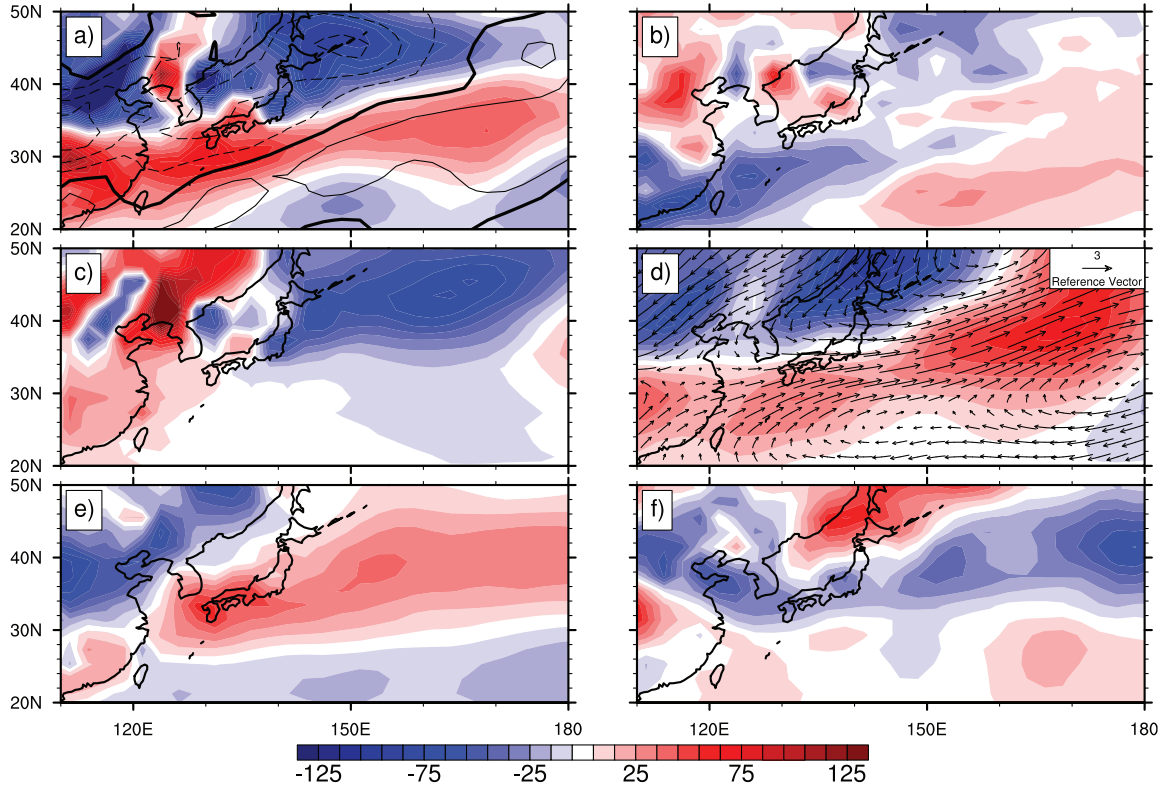


Figure 3.3 Anomalies (TP - noTP experiments) in horizontal dry enthalpy advection $-\langle c_p \mathbf{v} \cdot \nabla T \rangle$ (color contours) and vertically-integrated (normalized, not mass-weighted) meridional stationary eddy velocity divergence $\langle \partial_y v^* \rangle$ (line contours, contour interval 10^{-6} s^{-1}) (a), latent energy advection $-\langle L_v \mathbf{v} \cdot \nabla q \rangle$ (b), the advection of the stationary eddy dry enthalpy by the zonal-mean flow $-\langle c_p [\bar{\mathbf{v}}] \cdot \nabla T^* \rangle$ (c), the advection of the zonal-mean dry enthalpy by the stationary eddy velocity $-\langle c_p \bar{\mathbf{v}}^* \cdot \nabla T \rangle$ (color contours) and vertically-integrated (normalized, not mass-weighted) stationary eddy wind fields (vectors) with reference vector 3 m s^{-1} (d), the advection of the stationary eddy energy by the stationary eddy velocity $-\langle c_p \bar{\mathbf{v}}^* \cdot \nabla T^* \rangle$ (e), and the advection of the transient eddy energy by the transient eddy velocity $-\langle c_p \mathbf{v}' \cdot \nabla T' \rangle$ (f).

are negligible.

The same analysis is performed on the moisture budget and it is found that the presence of the TP primarily influences the stationary eddy convergence term $-\langle \nabla \cdot \mathbf{v}^* \rangle$ in the product of the zonal mean moisture and stationary eddy convergence $-\langle [\bar{q}] \nabla \cdot \mathbf{v}^* \rangle$ (Fig. 3.4). The presence of the TP barely exerts any influence on the zonal mean atmospheric specific humidity. The enhanced moisture flux convergence therefore is primarily due to enhanced wind convergence, or more specifically lower-level convergence, because the term $-\langle [\bar{q}] \nabla \cdot \mathbf{v}^* \rangle$ is

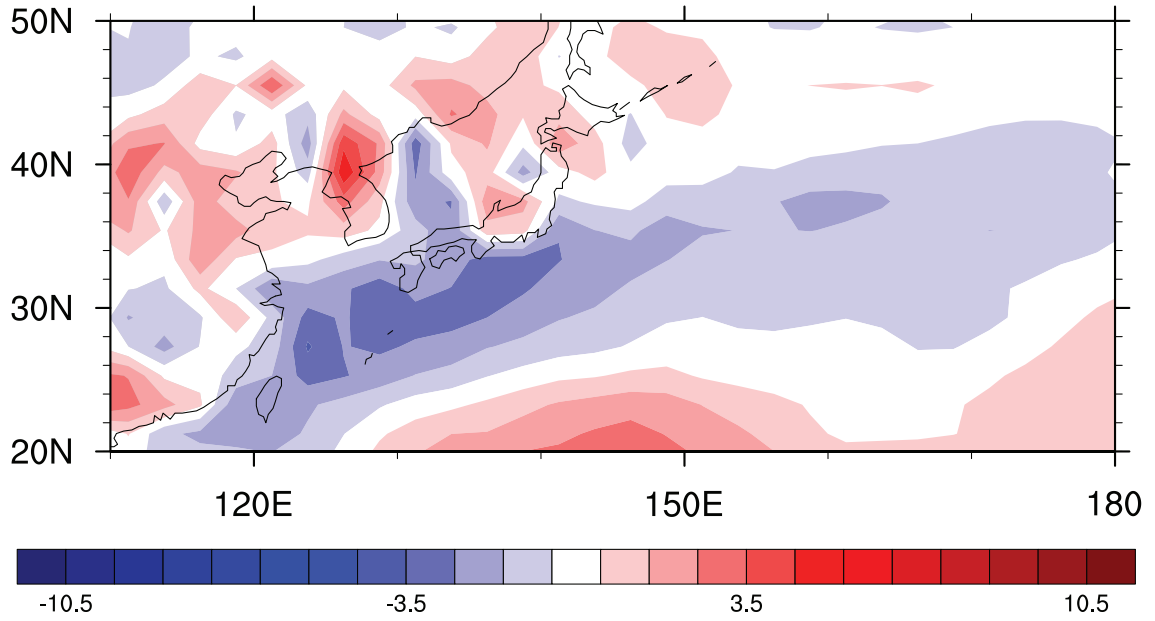


Figure 3.4 Anomaly (TP - noTP experiments) in the product of the zonal mean moisture and stationary eddy divergence $\langle \bar{q} \nabla \cdot \mathbf{v}^* \rangle$. Contours are in mm day^{-1} .

highly weighed by the water vapor content, mostly confined in the lower troposphere.

The zonal mean temperature gradient, $[\overline{\nabla T}]$, or equivalently the zonal mean latitudinal temperature gradient $[\overline{\partial_y T}]$, is nearly invariant in the troposphere in the MB region (not shown), allowing us to extract the temperature gradient term from the vertical integral of the advection of the zonal mean dry enthalpy by stationary eddies, i.e., $-\langle c_p \bar{\mathbf{v}}^* \cdot [\overline{\nabla T}] \rangle \approx -c_p \langle \bar{v}^* \rangle [\overline{\partial_y T}]$. This reveals that the pattern of change in the advection of the zonal mean dry enthalpy by stationary eddies is similar to that in meridional stationary eddy velocity, or meridional velocity, given that the change in the zonal mean meridional velocity is negligible in the simulations (Fig. 3.3d).

The meridional stationary eddy velocity, \bar{v}^* , shows a strong first baroclinic structure in the MB region (averaged from 110°E to 160°E) in both the reanalysis data (Fig. 3.5a) and the AM2.1 numerical simulation in the presence of the TP (Fig. 3.5b), with strong southerlies in the middle and lower troposphere and northerlies in the upper troposphere and stratosphere. It also shows pronounced meridional convergence almost throughout the entire troposphere,

with maximum up to 200 mb, between 30°N and 40°N. In the absence of the TP, the strength of the meridional stationary eddy velocity is significantly weakened, and is accompanied by a sharp reduction in its convergence in the free troposphere (Fig. 3.5c). The difference between the control and experiment runs is shown in Fig. 3.5d, with the presence of the TP causing a pronounced southerly wind to the south and northerly wind to the north of the MB region, and hence strong convergence over the MB region. The spatial patterns of changes in the vertically-integrated meridional stationary eddy velocity convergence and stationary wind fields are shown in Fig. 3.3a,d. The reinforced southerlies over the MB region in the presence of the TP bring abundant warm and moist air from tropical oceans to the MB region and the northwestern Pacific. The enhanced northerlies to the north of the MB region prevent the southerlies from invading further north and are associated with the meridional wind convergence (Fig. 3.5b and Fig. 3.6a). The meridional convergence has to be balanced by zonal divergence if integrated vertically. In pressure coordinates and neglecting topographic effects on boundary velocity, the continuity equation

$$\langle \nabla \cdot \bar{\mathbf{v}} \rangle = 0 \quad (3.2)$$

can be written as $\langle \overline{\partial_x u} + \overline{\partial_y v} \rangle = \langle \overline{\partial_x u^*} + \overline{\partial_y v^*} \rangle = 0$. Therefore, the convergence of the meridional stationary velocity (Fig. 3.5a) is coupled with divergence of the zonal stationary velocity (not shown). The zonal wind diverges over the MB region due to the interaction with the TP and the effect from the subtropical high, as well as possible influences by the precipitation system itself. The lower-level wind convergence (integrated from surface to 700 mb, Fig. 3.6c), due to the meridional wind convergence (Fig. 3.6a) and partly offset by zonal wind divergence (Fig. 3.6b), resembles the anomaly in the product of the zonal mean moisture and stationary eddy convergence $\langle [\bar{q}] \overline{\nabla \cdot \mathbf{v}^*} \rangle$ (Fig. 3.4) because $\delta([\bar{q}] \overline{\nabla \cdot \mathbf{v}^*})$ is highly weighted by $[\bar{q}]$.

At least qualitatively, the horizontal stationary eddy convergence and the meridional stationary eddy velocity can be related through Sverdrup balance, $\beta v^* \sim f \partial_p w^*$. While

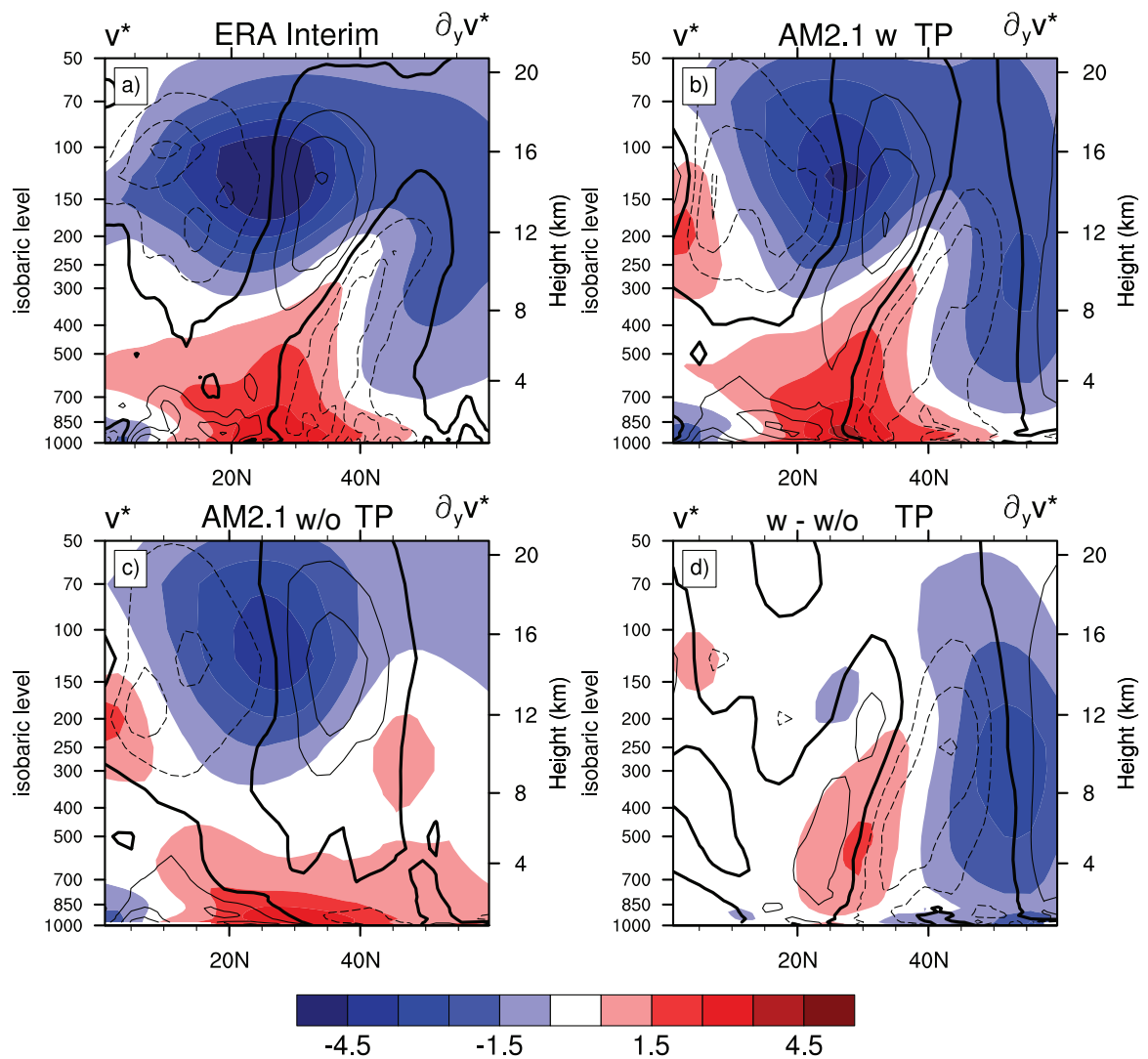


Figure 3.5 Meridional stationary eddy velocity $\overline{v^*}$ (color contours, m s^{-1}) and its convergence $\partial_y \overline{v^*}$ (line contours, contour interval 10^{-6} s^{-1}) averaged from 110°E to 160°E in the ERA-Interim reanalysis data (a), in the AM2.1 simulation in the presence of the TP (b), in the absence of the TP (c), and the difference between a and b (d).

not perfect (note for instance that the maximum of the meridional stationary eddy velocity, indicated by the zero line of its meridional gradient, Fig. 3.6a, and the maximum southerly wind velocity are not exactly colocated), this balance does seem to hold reasonably well in the MB region.

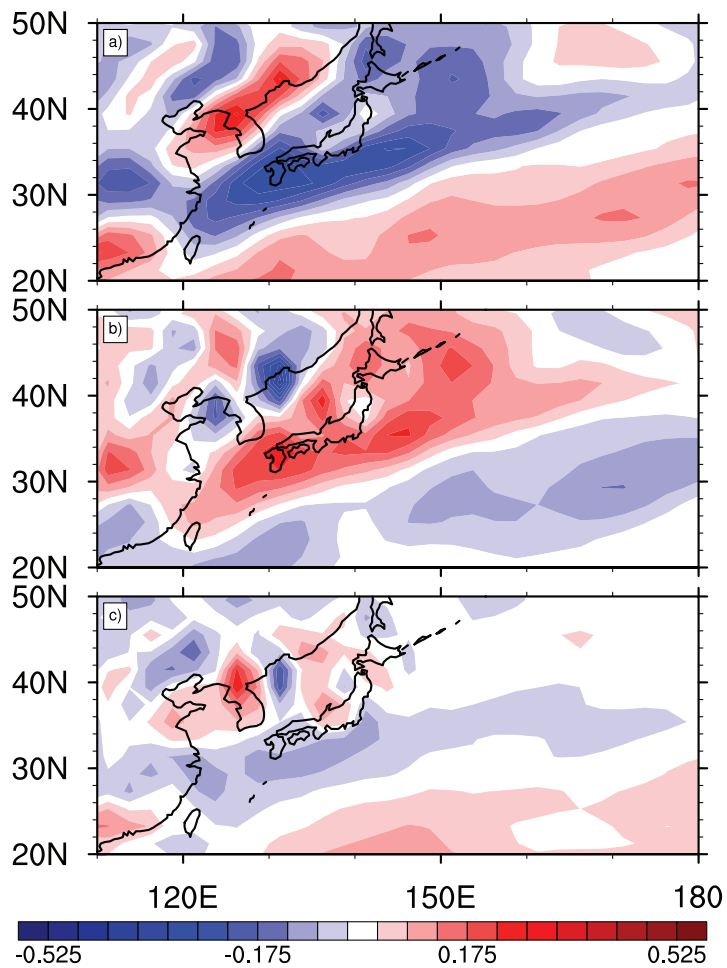


Figure 3.6 Anomalies (TP - noTP experiments) in $\partial_y \overline{v^*}$ (a), $\partial_x \overline{u^*}$ (b), and $\nabla \cdot \overline{\mathbf{v}^*}$ (c) integrated (normalized, not mass-weighted) from surface to 700 mb. Contours are in day⁻¹.

3.3. Conclusions

The numerical experiments with and without the TP show that:

- The TP primarily influences the formation of the MB front through changes in the meridional stationary eddy velocity $\overline{v^*}$ as well as its meridional gradient $\partial_y \overline{v^*}$;
- Changes in the meridional thermal gradient due to zonal asymmetries $\partial_x \overline{T^*}$ have a lesser impact and are confined to the near downstream of the TP.

In the literature, it is well accepted that the onset and demise of the MB season are governed by the position of the subtropical westerly jet (e.g., Ding and Chan 2005; Park et al. 2012a; Molnar et al. 2010; Sampe and Xie 2010), but the exact mechanisms are less well agreed upon. It has been suggested in Sampe and Xie (2010) that horizontal warm air advection from the southeastern flank of the TP by the subtropical westerly jet can initiate ascending motion that would have to be balanced by lower-level convergence and can sustain the front even in the absence of diabatic forcing. Our analysis confirms the importance of the horizontal dry enthalpy advection, but in addition to the advection by the zonal mean flow of temperature zonal asymmetries, it exposes the meridional advection of the mean temperature by the meridional stationary eddy velocity as a key mechanism. It is revealed in the AM2.1 simulations that the anomalous advection by $\overline{v^*}$ of the mean dry enthalpy is strongly coupled to the meridional stationary eddy velocity: increased meridional stationary eddy velocity amplifies the positive energy advection into the MB region and the northwestern Pacific Ocean and therefore intensifies the precipitation. Its pattern (i.e., latitudinal gradient) determines the wind convergence and is closely coupled with zonal eddy velocity. Although the total (zonal and meridional) warm air advection, as investigated by Sampe and Xie (2010), can successfully explain the location and seasonality of the MB, the application of the MSE budget, together with the eddy decomposition, allows us to isolate one single dominant factor, $\overline{v^*}$, based on a widely applicable theoretical framework, which

encapsulates the influences of the TP on the formation of the EASM.

Together with the upper-level westerly jet, the lower-level southerly flow around the subtropical high has also been identified as important in the climatological position and seasonal evolution of the MB front. Rodwell and Hoskins (2001) investigated the dynamics of summertime subtropical anticyclones in a dry model forced by the observed diabatic heating and argued for a more dominant role of the diabatic heating over the topography in driving the meridional southerly flow in the western flank of the North Pacific subtropical anticyclone. In moist circulations, such as the MB front, however, this separation might be artificial, given that patterns of convergence and divergence induced by topography shape and interact with the distribution of the diabatic heating. By using the MSE budget, we circumvent the need to specify or diagnose the diabatic heating and more generally focus on the role of thermally- and/or mechanically-induced stationary flows on the formation of the MB front.

Kodama (1992) investigated the Baiu front from an observational perspective, together with other subtropical convergence zones (STCZs), and found that the lower-level poleward flow around the subtropical high and the subtropical jet are two necessary circulation features for generating the STCZs. His study highlights the role of the lower-level poleward flow in water vapor transport, intensification of the moisture convergence, frontogenesis in equivalent potential temperature fields, and generation of convective instability. The poleward flow itself is interpreted as forming geostrophically in the longitudinal pressure gradient between the monsoonal heat low and the subtropical high (Kodama 1992; Ninomiya 1984). Our analysis suggests that these circulation features might not be independent from each other, and, by means of the MSE and moisture budget, sheds further light into their role in the MB front in terms of their resulting pattern of positive enthalpy advection. In fact, in the presence of upper tropospheric westerly flow, any zonal asymmetry, such as topography, land-sea thermal contrast and diabatic heating, can induce stationary Rossby waves, with associated temperature, moisture, and wind perturbations (see for instance Held et al. 2002, for a

comprehensive review of stationary waves in the northern hemisphere winter). Dispersion characteristics of these stationary Rossby waves might explain aspects of the observed MB, such as its spatial extent and tilted structure.

The results presented here suggest that the TP influences the EASM by both thermal and mechanical effects. In nature, these two effects cannot be separated and we do not argue to be able to give a quantitative assessment of their relative role in this paper. Future studies will attempt a more quantitative assessment by performing modified surface flux and albedo simulations (e.g., Wu et al. 2012). However, the successful explanation of the MB rainfall season within the framework of the MSE budget gives us confidence in continuing to explore attributable factors in the inter-model spread in CMIP5 EASM simulations and in attempting to assess future changes in the EASM in the context of global warming. Factors including accelerating warming and widespread loss of glacier and snow cover throughout the 21st century in the SRES A1B scenario (IPCC AR4), the expansion of the subtropical dry zones and changes in position and strength of the westerly jet, the possible non-linear changes in dry enthalpy advection and latent energy advection because of polar amplification and heterogeneous changes in relative humidity might all be critical in the future evolution of the EASM. The MSE and moisture budgets are expected to provide insights into the possible role of all these factors in EASM changes in a unified theoretical framework.

Chapter 4

Inter-model spread of EASM simulations

We use the understanding we have developed on the dynamics of the EASM based on the MSE and moisture budgets to expose parameters that explain the biases in precipitation amounts and spatial structure in CMIP5 EASM simulations. In return, the different present-day EASM simulations confirm the robustness of our theoretical framework in climate models. While not directly translatable into recommendations for model improvements, our results identify processes that are central for better constraining model simulations and projections of the EASM.

4.1. Data and method

In this study, we examine the CMIP5 decadal2000 hindcasts. The decadal predictions in CMIP5 consist of a series of 10-year or 30-year forecasts with initial observed climate states, and take into account both the long-term mean forced response and the internal decadal variability (Meehl et al. 2009; Taylor et al. 2012). Here, decadal2000 predictions are composed of 10-year integrations, initialized at the end of year 2000, in which ocean initial conditions are representative of either the observed anomaly or full-fields for the start date (i.e., full-field and anomaly initialization methods), but land, sea-ice, and atmosphere initial conditions are chosen at the discretion of different model groups (Taylor et al. 2012). Historical runs

differ from decadal runs in that they are started from stochastically selected preindustrial states and the synchronization between climate predictions and internal variability is not guaranteed. Especially when multi-ensemble mean (MEM) techniques are used to increase the predicability of long-term simulations (e.g., historical runs) in each individual model, the internal variability is suppressed and only an estimate of the forced response survives (Meehl et al. 2007). We prefer the decadal2000 run to the historical and RCP runs, as they allow for a better comparison with observations.

Monthly data of decadal2000 integrations from 2001 to 2009 from seventeen coupled climate models and three additional simulations with different initialization methods (a total of twenty experiments; refer to the legend of Fig. 4.2) are used to assess the model performance. All available ensembles for each individual model are averaged. When computing the MSE and moisture budgets as described below, we first average monthly fields over June and July, and then compute all budget terms and finally produce a long-term climatology by averaging over the nine available years. We also present results in which the long-term climatology (nine-year average) is applied before computing individual budget terms. The difference between the two climatologies lies in that the former (latter) includes (neglects) interannual transient eddies. While the mature MB phase is traditionally considered to span from June 15 to July 14, here we average over both June and July, because most model outputs are available on monthly averages. Accordingly, we focus on the broader EASM region (Fig. 4.1a, enclosed regions), which includes East China (20° - 42° N, 110° - 122° E, including the Meiyu region) and the Changma-Baiu-northwestern-Pacific (CBP, 122° - 170° E, with an upper latitudinal bound of 42° N, and a lower latitudinal bound linearly varying with longitude from 20° N to 30° N). In the context of the MSE budget (Eq. 4.1), vertical pressure velocity is used as a proxy for precipitation. This is a good approximation in continental deep convection regions, such as the Meiyu region, but might be less satisfactory in the CBP region, where precipitation is a mixture of deep convection and large-scale condensation along isentropes associated with extra-tropical storms (Chen and Bordoni 2014; Sampe and

Xie 2010). For this reason, in addition to results for the overall large-scale EASM domain, we also separately discuss East China and the CBP region.

Monthly observed precipitation is obtained from GPCP (Global Precipitation Climatology Project) and TRMM (Tropical Rainfall Measuring Mission) provided from obs4MIPs (<http://obs4mips.llnl.gov:8080/wiki/>, Teixeira et al. 2011) project hosted on the Earth System Grid Federation (<http://esgf.org>). Wind field, temperature and humidity are obtained from ERA Interim reanalysis (37 pressure levels, 512×256 N128 Gaussian grid, analysis fields produced for 0000, 0600, 1200, 1800 UTC) in the Data Support Section of the National Center for Atmospheric Research (NCAR), while precipitation, surface heat fluxes, and radiation are obtained from the ERA-Interim (1.5° grid Dee et al. 2011) 3-hour-forecast fields produced from forecasts beginning at 0000 and 1200 UTC. All data from model forecasts and observations are bilinearly interpolated to a $1^\circ \times 1^\circ$ grid, if necessary. Since there are systematic differences over ocean and land between GPCP and TRMM (Adler et al. 2000), both datasets are used here as observational references (Fig. 4.1b,c). We also use the ERA Interim precipitation to assess consistency and robustness between climate models and the ECMWF operational forecasting model.

Following Chen and Bordoni (2014) (hereafter CB14), we use the MSE and moisture budgets to interpret the inter-model spread of the EASM in the decadal2000 predictions. As a review, the MSE budget over a climatological period is

$$\langle w \partial_p h \rangle = \overline{F^{net}} - \langle \mathbf{v} \cdot \nabla E \rangle, \quad (4.1)$$

where $h = C_p T + gz + L_v q$ is the MSE, $E = C_p T + L_v q$ is the atmospheric moist enthalpy, F^{net} is the net energy flux into the atmosphere and is given by the sum of net radiative fluxes at the surface and top-of-atmosphere, and surface sensible heat and latent heat fluxes, \mathbf{v} is the horizontal wind field (u,v), and w is vertical velocity. $\langle \cdot \rangle$ indicates the mass-weighted vertical integral $\int(\cdot) dp/g$. To the extent that the MSE stratification, $\partial_p h$, remains everywhere

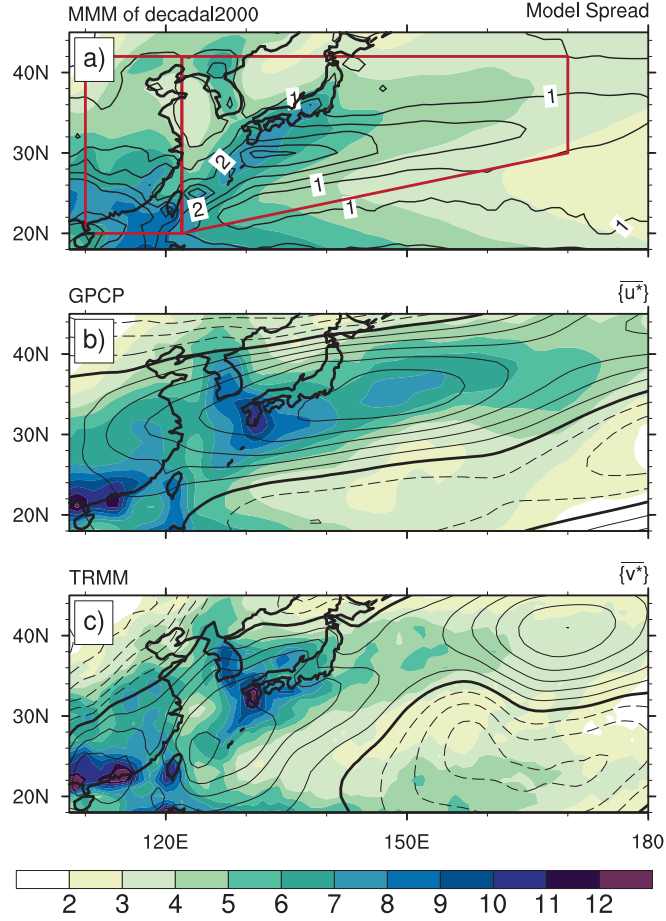


Figure 4.1 June-July climatological mean precipitation (shaded, mm day^{-1}) for the 2001-2009 nine-year period for the CMIP5 decadal2000 MMM (a), GPCP (b) and TRMM (c). Line contours (contour interval 0.5 mm day^{-1}) in (a) show the model spread or standard deviation of the twenty experiments listed in Fig. 4.2. Line contours in (b) and (c) show vertically-normalized stationary zonal and meridional eddy velocities, $\{\overline{u^*}\}$ and $\{\overline{v^*}\}$ (contour interval 1 m s^{-1} and 0.4 m s^{-1}), respectively. Red contour encloses the EASM region, comprising East China and the CBP region. See text for details.

negative, Eq. 4.1 links upward motion to regions of positive $\overline{F^{net}} - \langle \mathbf{v} \cdot \nabla E \rangle$. We further decompose each field into mean, stationary eddy, and transient eddy components, where conventionally $(\cdot)'$ indicates the deviation from the time mean $\overline{(\cdot)}$ (here the two month June and July mean for each individual year), i.e., $u' = u - \overline{u}$, and $(\cdot)^*$ denotes the deviation from the global zonal mean $[\cdot]$, i.e., $u^* = u - [u]$. By performing a similar decomposition using reanalysis data, CB14 found that two stationary eddy fluxes, $-\langle [\overline{u}] \cdot \overline{\partial_x T^*} \rangle$ and $-\langle \overline{v^*} \cdot [\overline{\partial_y T}] \rangle$, are the major contributors to the horizontal moist enthalpy advection. The first term, $-\langle [\overline{u}] \cdot \overline{\partial_x T^*} \rangle$,

represents the advection by the mean zonal flow of zonal temperature asymmetries, due to anomalous heating by the TP, convection and land-sea thermal contrast (Sampe and Xie 2010). The second term, $-\langle \overline{v^*} \cdot [\overline{\partial_y T}] \rangle$, is the advection of the mean meridional temperature gradient by the stationary eddy velocity and can be further approximated as proportional to $\langle \overline{v^*} \rangle$ at any given latitude, given that $[\overline{\partial_y T}]$ is almost height-independent in the free troposphere (Fig. 11d in CB14). Physically, positive stationary meridional eddy velocity $\langle \overline{v^*} \rangle$, arising from zonal asymmetries, transports warm air from the south to the EASM region. Given their role in determining the spatial pattern of positive upward motion, and hence precipitation, in the EASM region, $\overline{F^{net}}$, $-\langle [\overline{u}] \cdot \overline{\partial_x T^*} \rangle$, $-\langle \overline{v^*} \cdot [\overline{\partial_y T}] \rangle$ and $\langle \overline{v^*} \rangle$ will be used to assess the model performance in simulating the spatial structure of the EASM rainfall.

The inter-model spread in rainfall amounts is investigated using the moisture budget:

$$\overline{P} - \overline{E} = -\langle \overline{\nabla \cdot \mathbf{v}q} \rangle, \quad (4.2)$$

which, over a climatological average, directly relates the net precipitation $\overline{P} - \overline{E}$ to the horizontal moisture flux convergence $-\langle \overline{\nabla \cdot \mathbf{v}q} \rangle$. This term is further decomposed into contributions by the wind convergence $-\langle \overline{q \nabla \cdot \mathbf{v}} \rangle$ and moisture advection $-\langle \overline{\mathbf{v} \cdot \nabla q} \rangle$.

4.2. Assessment of inter-model spread

Global MSE and moisture budgets between June and July are evaluated across all climate models and ERA Interim. All models satisfy the global moisture budget by which $[\overline{P}] \approx [\overline{E}]$, with the exception of FGOALS-s2, in which $[\overline{E}] \sim 3.2 \text{ mm day}^{-1}$ and $[\overline{P}] \sim 2.7 \text{ mm day}^{-1}$. Over the climatological June-July average, the global precipitation is not strictly energetically constrained (e.g., O’Gorman et al. 2012), because of the coupling between solar insolation and hemispheric asymmetries in heat capacity. In boreal summer, the atmosphere gains energy, resulting in a positive heat storage in all climate models, mostly ranging from 0.5 W m^{-2} to 3.0 W m^{-2} , and with a maximum of 7.0 W m^{-2} in CFSv2-2011. ERA Interim

is known to have unbalanced moisture and MSE budgets (Berrisford et al. 2011). Hence, while we analyze and discuss results based on all models and observed data, we exclude FGOALS-s2, ERA Interim, and observations from our regression analysis.

The climatological MMM captures reasonably well the elongated band of the EASM precipitation spanning from East Asia into the northwest Pacific, but precipitation amounts are underestimated compared to both GPCP and TRMM (Fig. 4.1) due to biases in both precipitation intensity and spatial extent. Precipitation is particularly underestimated over the EASM oceanic region compared to GPCP, with better agreement with TRMM. The systematic bias between TRMM and GPCP found here, with lower TRMM estimates over EASM oceanic regions, is consistent with previous studies (Adler et al. 2009). The inter-model spread (Fig. 4.1a) is large in both heavily precipitating continental regions and mildly precipitating oceanic regions. The large spread in the former might be accounted for by different convective parameterizations and simulated circulations in different models (e.g., Song and Zhou 2013; Zhou et al. 2009), with discrepant simulations of high precipitation generating large standard deviations. The large spread in the latter appears to be more related to differences in the simulated spatial structure of precipitation over the northwestern Pacific. The analyses below allow for a more in-depth understanding of the inter-model spread in both spatial structure and precipitation amounts in the EASM region.

a. Spatial structure

Fig. 4.2 shows the spatial centered-pattern correlations between precipitation and the MSE budget terms identified in CB14 as fundamental in determining the spatial patterns of upward motion. A relatively high correlation between precipitation and $\overline{F^{net}}$ is observed and agreed upon amongst climate models, particularly in the CBP region. This is not unexpected given that $\overline{F^{net}}$ depends on the circulation itself and, through changes in energy and radiative fluxes because of clouds, is influenced by model-dependent physical parameterizations of clouds, radiation, and air-sea interaction. The observed TRMM and GPCP rainfall estimates

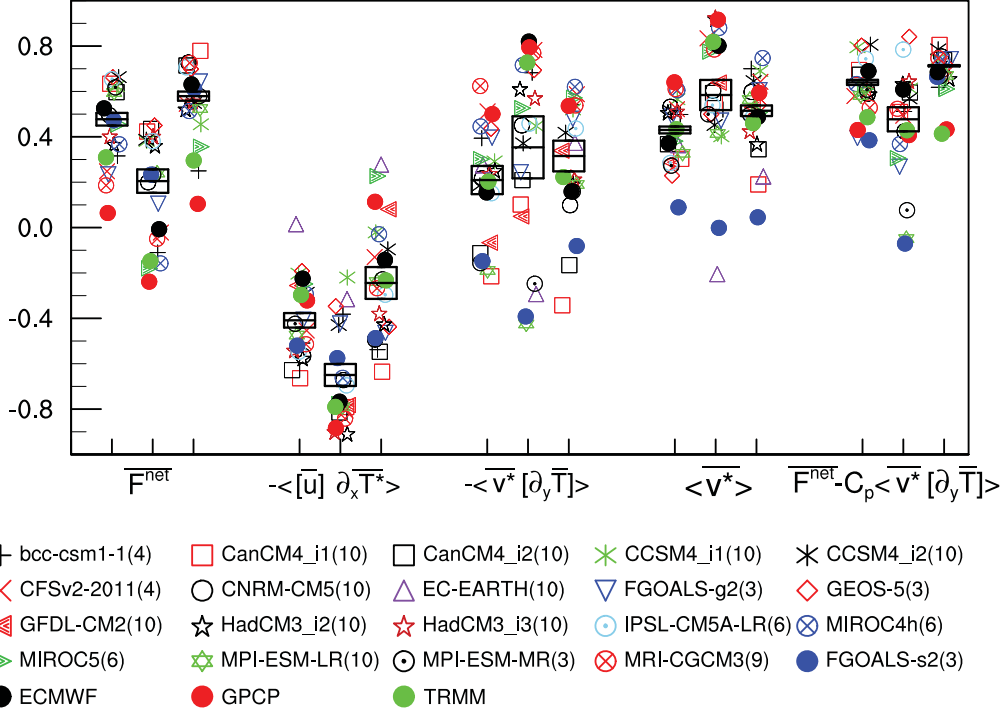


Figure 4.2 Spatial pattern correlation (centered) between the precipitation over the EASM region (left in each column), East China (middle), and the CBP region (right) and the metrics indicated in the diagram. Each metric is summarized by a boxplot, characterized by mean value and standard deviation of correlation (with the exception of FGOALS-s2). The name of the seventeen models and three additional experiments with different initialization method are labeled in the legend, with initialization methods (when necessary) labeled with $i\#$, and the number in parenthesis indicating the number of ensembles.

have relatively low correlation with the ERA Interim $\overline{F^{net}}$.

From a large-scale perspective, the subtropical westerly jet advects warm air from the TP to the MB region and induces ascending motion through $-\langle [\bar{u}] \partial_x \bar{T}^* \rangle$ (CB14, Sampe and Xie 2010); nevertheless, we find a negative correlation between P and $-\langle [\bar{u}] \partial_x \bar{T}^* \rangle$ everywhere in the EASM domain. Thermal effects by the TP and land-sea contrast result in a negative longitudinal temperature gradient in the EASM region. Convection tends to smooth out this temperature gradient in the free troposphere, which helps explain the observed negative correlation. The correlation between precipitation and the term $-\langle \bar{v}^* \cdot [\partial_y \bar{T}] \rangle$ varies significantly amongst different models; however, when we only consider $\langle \bar{v}^* \rangle$, correlations increase

and the model spread decreases significantly, especially in East China (see also the close coincidence of spatial patterns of precipitation and $\{\overline{v^*}\}$ from observations in Fig. 4.1c), with the exception of two outliers. Finally, the largest spatial correlations are obtained when we consider the combined effect of $\overline{F^{net}} - \langle \overline{v^*}[\partial_y \overline{T}] \rangle$. A nonparametric test with bootstrapping techniques shows that the correlation between \overline{P} and $\overline{F^{net}} - \langle \overline{v^*}[\partial_y \overline{T}] \rangle$ is significantly larger than the correlation between \overline{P} and $\overline{F^{net}}$ alone (The null hypothesis in the test is that the mean of the two sample pools is the same. For any constructed samples with size larger than 4 out of total sample pool of size 17 (EC-EARTH and GFDL-CM2 are not included because of incomplete data outputs) with 10,000 random repetitions, the null hypothesis can be rejected at 0.01 level.). This confirms that, in spite of differing simulated precipitation over the EASM region, the underlying dynamics is the same across models and data: the combined positive pattern of the advection of the mean meridional temperature gradient by the stationary eddy meridional velocity $\langle -\overline{v^*}[\partial_y \overline{T}] \rangle$, and the net energy input into the atmospheric column $\overline{F^{net}}$, is the most important large-scale factor controlling the spatial distribution of precipitation in the EASM region.

The analysis above suggests that anomalies in the EASM precipitation are strongly correlated with biases in the simulated $\langle \overline{v^*} \rangle$, which is primarily due to topographically induced stationary waves and the resulting diabatic heating distribution (CB14, Rodwell and Hoskins 2001; Wu et al. 2007a; Park et al. 2012b). The reasons of such disparate simulations of $\langle \overline{v^*} \rangle$ remain unclear, but are likely to be affected by the model’s resolution and the interaction of the model’s physics with the simulated large-scale circulation.

b. Rainfall amount

How can biases in the simulated large-scale dynamics constrain biases in simulated rainfall amounts? The simulated EASM regional precipitation (Fig. 4.3) shows a wide range across the seventeen climate models, with most models producing an area-average of 4.2-5.0 mm day⁻¹, and minima and maxima ranging between ~ 3.5 mm day⁻¹ (EC-EARTH) and \sim

6.5 mm day⁻¹ (HadCM3). ERA Interim precipitation is also presented as a reference. It is not unreasonable to expect that models with moist (dry) biases in the global average might have similarly signed biases in precipitating regions (see Muller and O’Gorman (2011) for similar arguments on the regional precipitation response to climate change). The spread in the simulated EASM rainfall \bar{P} , especially in East China, can in fact be partially explained by the spread in the simulated background global precipitation $[\bar{P}]$ (Fig. 4.3a,d). The remaining spread arises from spread in mean moisture flux convergence $\langle \nabla \cdot \bar{\mathbf{v}} \bar{q} \rangle$, which is close to the total moisture flux convergence $\langle \overline{\nabla \cdot \mathbf{v} q} \rangle$ because of almost negligible transient term in most climate models. CB14 show that the largest contribution to the vertically-integrated moisture convergence comes from the moisture-weighted meridional stationary eddy convergence integrated from the surface to 700 mb, i.e., $MWC = - \int_{surf}^{700mb} \bar{q}^d \partial_y \bar{v}^{*d} dp/g$, where superscript d denotes the decadal climatological average. Fig. 4.3 (b,e,h) show that this metric provides a remarkable, albeit not perfect, estimate of the total moisture flux convergence and accounts for the spread across all climate models.

The empirical association of the EASM precipitation and the subtropical westerly jet has been discussed in many studies (e.g., CB14; Kodama 1992; Sampe and Xie 2010). While several hypotheses have been proposed to explain this association, thermal wind balance suggests a direct link between the intensity and location of the upper-tropospheric subtropical westerly jet and the horizontal temperature gradient, which is influenced by the atmospheric diabatic heating (Zhang et al. 2006). The westerly winds have an equivalent barotropic structure over the EASM region, so we use the vertically-normalized zonal wind eddy velocity $\{\bar{u}^*\} = \frac{1}{(p_{bottom} - p_{top})} \int \bar{u}^* dp$ (e.g., Fig. 4.1b, linear contour) as an index of the subtropical westerly jet core. Precipitation amounts are indeed well correlated to $\{\bar{u}^*\}$ in regions of strong meridional temperature gradient, i.e., CBP (Fig. 4.3i). However, no such correlation is observed over East China, where meridional temperature gradients are weak (Fig. 4.3f).

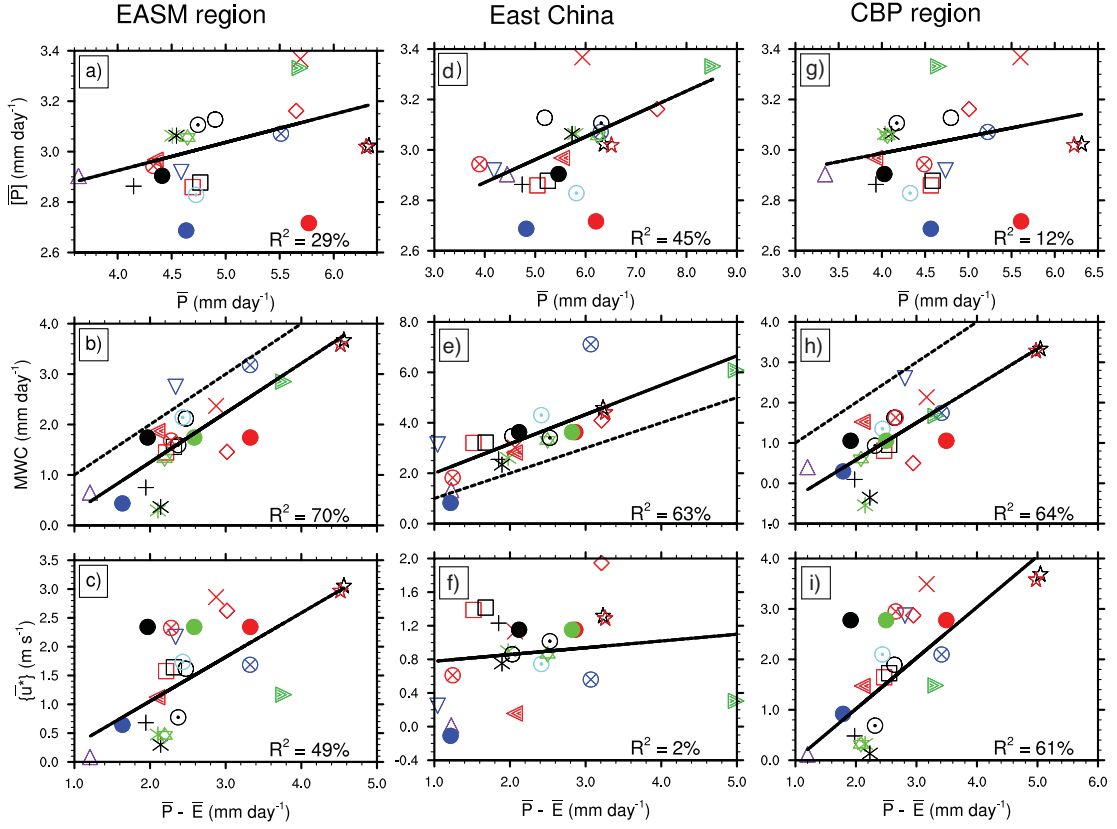


Figure 4.3 Regression between the regional precipitation \bar{P} (x -axis) and (top) global precipitation $[\bar{P}]$ (y -axis), between the estimated moisture flux convergence $\bar{P} - \bar{E}$ (x -axis) and (center) normalized $-\int_{surf}^{700mb} \bar{q}^d \partial_y \bar{v}^{*d} dp$ (y -axis), and (bottom) vertically-normalized stationary zonal wind eddy velocity $\{\bar{u}^*\}$ (y -axis) over the EASM region (left), East China (middle), and the CBP region (right). The coefficient of determination R^2 is calculated based on all models except for FGOALS-s2, which does not satisfy the global P-E budget, excludes ECMWF reanalysis, GPCP, and TRMM products, and is significant at the 95% level of a two-tailed Student's t test if larger than 21%. The dashed line denotes the one-to-one relationship.

4.3. Conclusions

CMIP5 simulations of the EASM have been assessed within the MSE and moisture budgets. We have shown that the spatial distribution of the simulated precipitation is strongly correlated to the sum of the net energy input into the atmospheric column and the zonal mean temperature advection by the meridional stationary velocity, $\overline{F^{net}} - \langle \bar{v}^* [\partial_y \bar{T}] \rangle$. In terms of rainfall amounts, we find that the wide inter-model spread can be only partly relat-

ed to the background spread in the globally-averaged precipitation (particularly over East China), and is primarily due to disparate simulations of the large-scale circulation as characterized by the lower-level meridional stationary wind convergence. In both analyses, the stationary eddy velocity, $\langle v^* \rangle$, appears to be the most important single metric capturing the inter-model spread. The meridional eddy velocity over the EASM region is primarily due to stationary waves induced by land-sea contrast and the TP (CB14), and their interaction with the resulting diabatic heating, highlighting existing deficiencies in how GCMs represent moisture-circulation interactions. These conclusions are consistent with those in CB14 and are expected to provide useful constraints for future projection of the EASM as well as other STCZs.

The EASM rainfall amount is partially affected by the simulated globally-averaged precipitation, whose spread should be energetically constrained on annual averages, but might be only loosely constrained over monthly time scales because of atmospheric heat storage. The range in the simulated June-July global precipitation amongst different models is as large as 0.7 mm day^{-1} , which is equivalent to $\sim 18 \text{ W m}^{-2}$ difference in atmospheric latent heating. Such spread in latent heating can be examined using observations, such as the CERES-EBAF together with sensible heat in ERA Interim and attributed to errors in simulated radiative and/or heat fluxes.

Analyses similar to those discussed here will be used to investigate future projections on the regional scale. We will specifically explore if the inter-model spread in future EASM changes in response to increasing greenhouse gases will diverge, based on the existing wide spread in the present-day climate. If so, identifying key processes that need to be accurately represented in climate models to better constrain present-day climate, as we do in this study, is the first necessary step to reduce future projections of the EASM and ultimately provide effective guidance to adaptation measures at the regional scale.

Chapter 5

Response of the East Asian Summer Monsoon to Atmospheric CO₂ Forcing and Subsequent Sea Surface Warming

Under global warming forced by atmospheric CO₂, regional precipitation has been shown to change in differing ways on different time scales. In this chapter, we use the readily available simulations in the CMIP5 archive to diagnose the mechanisms embedded in the EASM projections at fast and slow time scales. We frame our analysis on the moisture budget, and partition precipitation anomalies into dynamic and thermodynamic components. We find that the dynamic component plays an important role in setting up the spatial pattern of regional precipitation changes. We expose mechanisms behind these dynamical changes. Numerical simulations with the GFDL AM2.1 are used to further assess the relative role of land-sea contrast, topography and SST patterns in driving the circulation, and hence precipitation, response.

5.1. Data and Method

We use 11 climate model single realization outputs (Table 5.1) with monthly mean from several CMIP5 experiments (Taylor et al. 2012): 30-year atmosphere-only simulations forced by a fixed 1xCO₂ or 4xCO₂ concentration with prescribed SST distribution that remains unchanged in both sets of experiments (sstClim or sstClim4xCO₂); 150-year fully-coupled

Table 5.1 CMIP5 models that have outputs in piControl, sstClim, sstClim4xCO2, and abrupt4xCO2.

Model name	Modeling group	Resolution (plevXlatXlon)
bcc-csm1-1	Beijing Climate Center (BCC), China Meteorological Administration	17X64X128
CanESM2	Canadian Centre for CLimate Modelling and Analysis (CCCMA)	22X64X128
CCSM4	National Center for Atmospheric Research (NCAR)	17X192X288
CSIRO-Mk3-6-0	CSIRO in collaboration with Queensland CLimate Change Centre of Excellence (CSIRO-QCCCE)	18X96X192
inmcm4	Institute of Numerical Mathematics (INM)	17X120X180
IPSL-CM5A-LR	L'Institut Pierre-Simon Laplace (IPSL)	17X96X96
MIROC5	L'Institut Pierre-Simon Laplace (IPSL)	17X128X256
MPI-ESM-LR	Max Planck Institute for Meteorology (MPI-M)	25X96X192
MPI-ESM-MR	Max Planck Institute for Meteorology (MPI-M)	25X96X192
MRI-CGCM3	Meteorological Research Institute (MRI)	23X160X320
NorESM1-M	Norwegian Climate Centre (NCC)	17X96X144

ocean-atmosphere simulations forced by a constant 4xCO2 concentration (abrupt4xCO2); and fully-coupled simulations forced by pre-industrial forcings (piControl). The 30-year sstClim and sstClim4xCO2, piControl and the last 30 years of abrupt4xCO2 are averaged to represent the climatology of different climate states. The monthly resolution of available data does not allow for consideration of sub-monthly transient eddies in our analyses.

The fast response is computed as the difference between sstClim4xCO2 and sstClim, in which the SST distribution is prescribed based on the climatology from pre-industrial simulations. In these two sets of experiments the only difference is, therefore, the atmospheric CO₂

concentration. The slow response is computed as the difference between abrupt4xCO2 and sstClim4xCO2, in which the atmospheric CO₂ concentration in both scenarios is essentially the same, and the only difference is the subsequent warming in SSTs in the abrupt4xCO2 scenario.

As done in several previous studies of regional climate changes, we use the moisture budget to study the hydrological change in the EASM region,

$$\langle \overline{\partial_t q} \rangle + \langle \overline{\nabla \cdot (\mathbf{v}q)} \rangle + \langle \overline{\partial_p(\omega q)} \rangle = -\overline{P} + \overline{E}, \quad (5.1)$$

where \mathbf{v} indicates horizontal winds, ω is vertical wind, q is water vapor in the atmosphere, P is precipitation, and E is evaporation. $\overline{(\cdot)}$ indicates temporal mean. Ignoring water vapor storage in the atmosphere and vertical velocity at the surface, Eq. 5.1 can be written as

$$\overline{P} - \overline{E} = -\langle \overline{\nabla \cdot (\mathbf{v}q)} \rangle. \quad (5.2)$$

This budget closes only if variables \mathbf{v} and q include all temporal resolutions. Because our data are at monthly resolution, the calculated moisture flux convergence does not include the contribution from sub-monthly transient eddies. Hence, this contribution has to be estimated as the residual of Eq. 5.2. In the following, we will drop the notation $\overline{(\cdot)}$, with all variables in following equations indicating monthly means.

In order to expose contributions from individual climatic variables to changes in the moisture budget, we decompose specific humidity, q , into the product of relative humidity, H , and saturation specific humidity, q_s , as done by previous studies. One caveat is that by using the monthly average of relative humidity, we ignore the covariance of relative humidity and temperature (through the saturation specific humidity) on sub-monthly timescales.

The moisture budget can hence be written as

$$\delta(P - E) = -\langle \delta \nabla \cdot (\mathbf{v} \cdot Hq_s) \rangle + \text{residual}, \quad (5.3)$$

where δ indicates the difference between sstClim4xCO2 and sstClim (abrupt4xCO2 and sstClim4xCO2) scenarios in the fast (slow) response, and the second term on the right hand side of Eq. 5.3 is a residual, including sub-monthly transient eddies and moisture tendency in the atmosphere. The moisture flux convergence term can be further decomposed as,

$$\begin{aligned}
-\langle \delta \nabla \cdot (\mathbf{v} \cdot H q_s) \rangle &= -\langle \nabla \cdot (\delta \mathbf{v} \cdot H q_s(T)) \rangle + \\
&\quad -\langle \nabla \cdot (\mathbf{v} \cdot q_s(T) \delta H) \rangle - \langle \nabla \cdot (\mathbf{v} \cdot H \delta q_s(T)) \rangle - \langle \nabla \cdot (\mathbf{v} \cdot \delta H \delta q_s(T)) \rangle + \\
&\quad -\langle \nabla \cdot (\delta \mathbf{v} \cdot q_s(T) \delta H) \rangle - \langle \nabla \cdot (\delta \mathbf{v} \cdot H \delta q_s(T)) \rangle - \langle \nabla \cdot (\delta \mathbf{v} \cdot \delta H \delta q_s(T)) \rangle,
\end{aligned} \tag{5.4}$$

where terms on the right hand side represent, respectively, the change due to winds, relative humidity, saturation specific humidity and hence temperature, the covariance between relative humidity and temperature, the covariance between winds and relative humidity, the covariance between winds and temperature and the covariance among winds, temperature, and relative humidity. Assuming no changes in winds and relative humidity, anomalies due to saturation specific humidity, $-\langle \nabla \cdot (\mathbf{v} \cdot H \delta q_s(T)) \rangle$, can be further decomposed into two terms, $-\langle \nabla \cdot (\mathbf{v} \cdot H \delta q_s^*(T)) \rangle$ and $-\langle \nabla \cdot (\mathbf{v} \cdot H \delta (q_s(T) - q_s^*(T))) \rangle$, where $q_s^*(T)$ is $q_s(T)$ at the surface. The former can also be written as $-\alpha \delta T (P - E)$, where $\alpha = L_v / RT^2$, L_v is the latent heat of evaporation and R is the gas constant for water vapor. $-\alpha \delta T (P - E)$ has been described in the literature as the “wet get wetter” pattern (e.g., Held and Soden 2006), by assuming fixed shape of the temperature profile under climate change (similar to the Planck response in climate sensitivity studies) and ignoring changes in transient eddy fluxes. It predicts that with warming, (δT) , the pattern of net precipitation $(P - E)$ will simply be enhanced: becoming more positive when it is already positive; and more negative when it is already negative. The latter arises due to lapse rate changes or changes in the shape of the temperature profile.

In addition to these CMIP5 experiments, we also perform simulations with the GFDL

AM2.1. Six experiments (noTopo_control, noTopo_4xCO2, Topo_control, Topo_4xCO2, Uni4K and CMIP5SST) are performed (see more details in Table 5.2). These experiments have been designed to explore the impact of different regional forcings, such as land-sea contrast, topography and SST distribution, on the EASM response. For instance, the difference between noTopo_4xCO2 and noTopo_control is expected to show how enhanced land-sea thermal contrast influences regional precipitation without any contribution from topographic forcing. These results can be compared with their counterparts with full topography. The difference between 4xCO2 and Uni4K or CMIP5SST is expected to show how SST patterns (in addition to SST uniform warming) affect the EASM. Climatological-fixed SSTs without interannual variability from monthly-mean Reynolds SST analysis are used as boundary condition (Smith et al. 1996). Each experiment ran for 25 years, and the last 14 years of the simulations are used for the analyses.

We analyze changes in the EASM precipitation and circulation just for the month of June, when most models well capture the EASM rainfall band. In doing so, we ignore possible changes in the EASM seasonality and only focus on seasonal mean changes in rainfall intensity and position.

5.2. Rainfall anomalies

With quadruple CO₂ forcing, rainfall increases over the EASM region, particularly over the oceanic regions on the southern flank of the rainfall band (Fig. 5.1a). Most of the precipitation increase only happens when SST starts to warm. With CO₂ forcing alone, rainfall decreases over oceanic regions, while it increases over East China (Fig. 5.1b). The decrease in precipitation is colocated with the rainfall band, indicating that it is not simply a result of model artifact but a robust signal in changes in the strength of the EASM precipitation. The slow response shows a pattern opposite to the fast response – rainfall decreases over East China while it increases over the oceanic regions (Fig. 5.1d). The difference between coupled

Table 5.2 Experiments designed by using the GFDL-AM2.1.

Acronyms	Descriptions	Configurations
noTopo_control	Benchmark present-day simulation with no topography	Removed global topography, climatological SSTs, CO ₂ concentration 320 ppm
noTopo_4xCO2	Evaluate impact on precipitation from enhanced land-sea contrast due to atmospheric CO ₂ forcing without topographic forcing	Same as noTopo_control but with CO ₂ concentration 1280 ppm
Topo_control	Benchmark present-day simulation with full topography	Retained global topography, climatological SSTs, CO ₂ concentration 320 ppm
Topo_4xCO2	Evaluate impact on precipitation from enhanced land-sea contrast due to atmospheric CO ₂ forcing with topographic forcing	Same as Topo_control but with CO ₂ concentration 1280 ppm
Uni4K	Evaluate impact of uniform increase in SSTs by 4K	Same with 4xCO2 but global SSTs are increased by 4K everywhere
CMIP5SST	Evaluate impact of increase in SSTs as evaluated from the MMM in the CMIP5 slow response	Same as 4xCO2 but with anomalies in the slow response from CMIP5 MMM added to global SST

and uncoupled simulations in EASM precipitation is fairly small (Fig. 5.1c, the spatial pattern and magnitude is consistent with a recent study by Song and Zhou 2014, their Fig. 8c) compared to that in either fast or slow response, safely concluding that air-sea interaction can be ignored and that the signal in Fig. 5.1d comes from the SST forcing in the MMM.

a. Fast Response

The fast response of the EASM rainfall band to elevated CO₂ concentrations with fixed SSTs features a decrease (increase) of precipitation over oceanic (land) regions (Fig. 5.1b). This precipitation response is robust in most models (not shown).

Anomalies in net precipitation (Fig. 5.2a) largely explain the pattern of precipitation change in the EASM (Fig. 5.1b), with changes in evaporation being important only over

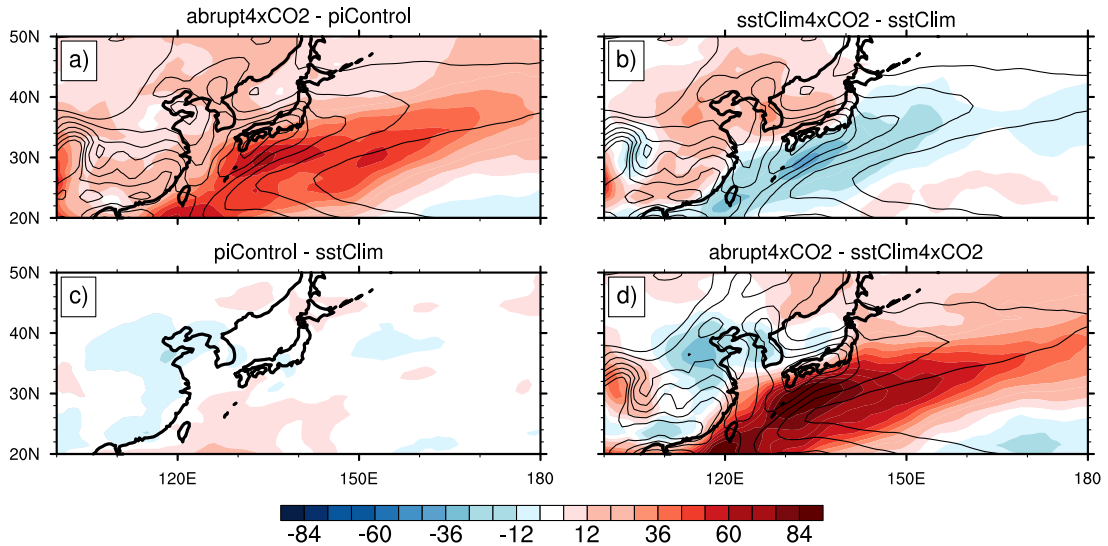


Figure 5.1 Multi-model mean changes in precipitation (shading, W/m^2) between different climate states and climatological precipitation (linear contour interval 1 mm/day, 3 – 9 mm/day) in each base state.

oceanic regions: here, the contribution by evaporation decreases along regions of large climatological evaporation (Fig. 5.2b). The spatial pattern of net precipitation change is consistent with changes in mean moisture flux convergence (Fig. 5.2c), although transient eddy flux anomalies, calculated as the residual of the moisture budget, are not negligible (Fig. 5.2d). Changes in mean moisture flux convergence are mainly captured by those due to winds (Fig. 5.2e). Contributions from changes in temperature (Fig. 5.2g), relative humidity (Fig. 5.2f), and their covariances (Fig. 5.2j-l) play a less important role. This confirms that in the absence of SST changes, the precipitation response is primarily dominated by changes in circulation, as seen in other tropical-subtropical regions (Bony et al. 2013a).

b. Slow response

At a first glance, changes in the slow response appear to follow the “wet get wetter” pattern. However, important deviations from the simple thermodynamic change exist (Fig. 5.3a): While the response is characterized by a well organized positive change in net

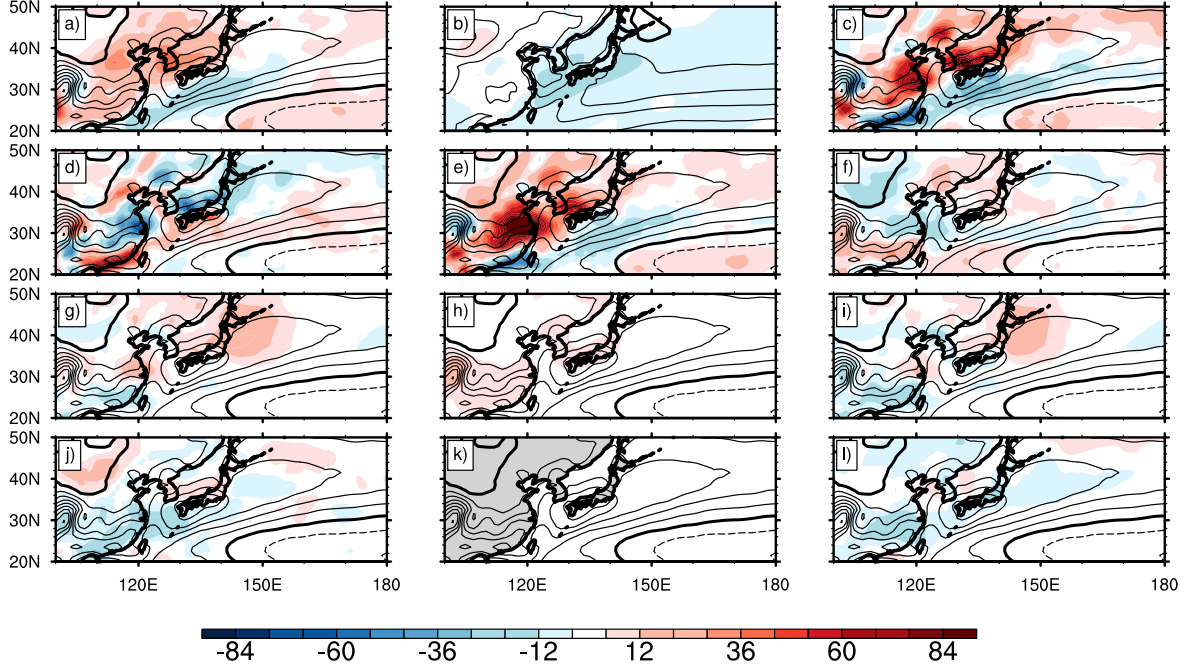


Figure 5.2 MMM anomalies (shading, W/m^2) between sstClim4xCO_2 and sstClim of net precipitation $\delta(P - E)$ (a), evaporation δE (b), mean flux convergence $-\langle \delta \nabla(\mathbf{v} \cdot Hq_s) \rangle$ (c), transient component (d, subtracted from a by c), wind component $-\langle \nabla(\delta \mathbf{v} \cdot Hq_s) \rangle$ (e), relative humidity component $-\langle \nabla(\mathbf{v} \cdot \delta Hq_s) \rangle$ (f), temperature component $-\langle \nabla(\mathbf{v} \cdot H\delta q_s) \rangle$ (g), temperature component due to the Planck response (surface temperature) $-\alpha \delta T_s(P - E)$ (h), temperature component due to lapse rate response (i, subtracted from g by h), covariance between relative humidity and wind $-\langle \nabla(\delta \mathbf{v} \cdot \delta Hq_s) \rangle$ (j), covariance between relative humidity and temperature $-\langle \mathbf{v} \cdot \nabla(\delta H\delta q_s) \rangle$ (k), and covariance between wind and temperature $-\langle \nabla(\delta \mathbf{v} \cdot H\delta q_s) \rangle$ (l). Line contour (contour interval 1 mm/day, solid (dash) line means positive (negative) value) indicates climatological net precipitation in sstClim4xCO_2 (a,c-l), climatological evaporation (b).

precipitation, this is located to the south of its climatological location. The net precipitation change over East China is negative, counteracting its positive change in the fast response. Surface evaporation increases, particularly over oceanic regions where large evaporation reductions occur in the fast response (Fig. 5.3b). This increase in surface evaporation might be due to the experiment configuration: in sstClim4xCO_2 , SSTs are prescribed and surface evaporation is strongly limited; in abrupt4xCO_2 , SSTs are interactive, and a strong increase in local SSTs due to ocean dynamics might explain the narrow band of enhanced evaporation (Xie et al. 2010).

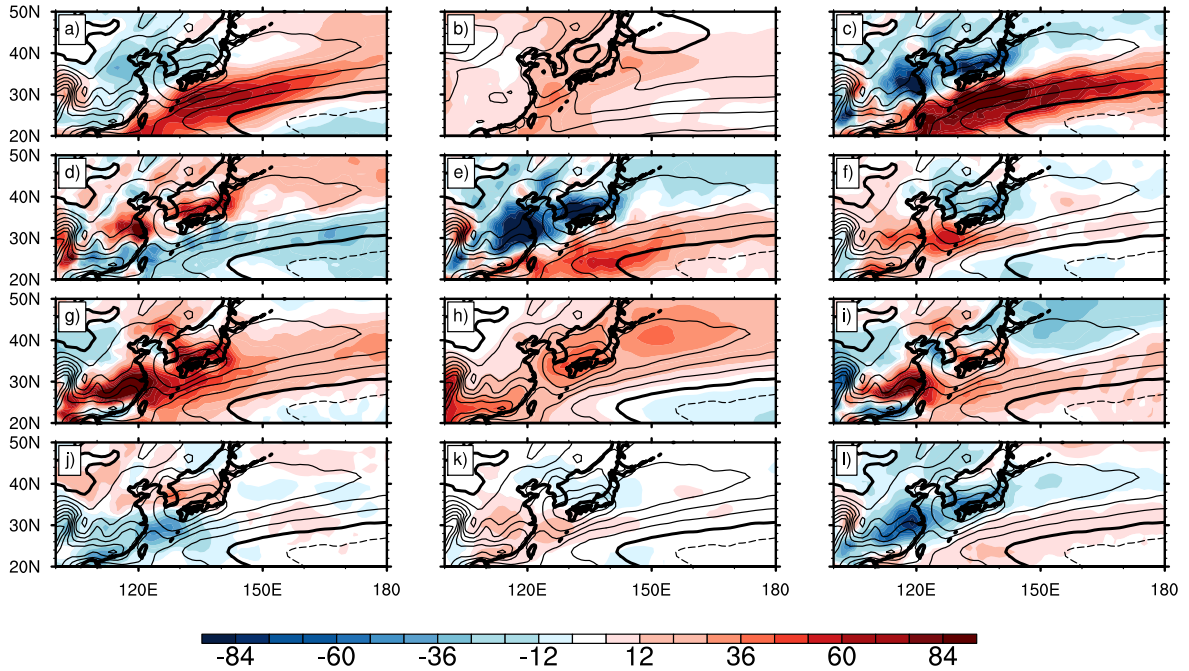


Figure 5.3 Same with Fig. 5.2 but for slow response.

The mean flux convergence, $-\langle \delta \nabla(\mathbf{v} \cdot Hq_s) \rangle$, captures the overall spatial pattern of the net precipitation change in Fig. 5.3a, with strong moisture convergence on the southern flank of the rainfall band. Transient eddies show a significant contribution to the balance (Fig. 5.3d). Recall that because of the monthly resolution of the CMIP5 data, the transient eddy contribution is estimated from the moisture budget residual, which prevents a more careful mechanistic understanding of the transient eddy response. Changes due to winds (Fig. 5.3e) and temperature (Fig. 5.3g) are both important, with circulation changes dominating the overall spatial pattern, and temperature changes increasing moisture convergence over the climatological convergence zone. Contributions from relative humidity changes are nontrivial, but their magnitude and spatial extent are smaller than those from wind and temperature changes (Fig. 5.3f). As discussed in section 2, changes due to temperature can be decomposed into the Planck response (Fig. 5.3h) and the lapse rate response (Fig. 5.3i). The Planck response relates the climatological net precipitation, weighted by the surface warming, to changes in net precipitation, or the so-called “wet get wetter” pattern. The

Planck response dominates the total response due to temperature, in both magnitude and spatial pattern. Weak signals over some land and oceanic regions are due to nearly zero climatological net precipitation, where local precipitation is primarily balanced by evaporation (c.f. Fig. 7a in Chen and Bordoni 2014). The coupling between temperature (saturation specific humidity) and wind changes (Fig. 5.3l) is dominant among the covariance terms (Fig. 5.3j-l) and resembles the dynamic change due to only winds (Fig. 5.3e). The reasoning is as follows: since temperature increases everywhere, the sign in the response is due to changes in winds, with specific humidity, $(q_s(T))$, and specific humidity changes, $(\delta q_s(T))$, acting as scaling factors.¹

In both fast and slow responses, changes in circulation are significant and dominate the spatial pattern of the precipitation anomalies. Changes in thermodynamic quantities, such as temperature and relative humidity, play a less important role. Hence, we focus primarily on analyzing the local circulation changes, and infer possible mechanisms through which fundamental forcings, such as land-sea contrast, topography, and atmospheric CO₂, affect local circulations directly or indirectly through larger-scale atmospheric circulation changes such as those of the NPSH.

Fig. 5.4 shows changes in precipitation and moisture flux due to changes in winds and geopotential height. Specifically, to clearly link geopotential height to circulation changes, in Fig. 5.4 we show differences in the local geopotential relative to the maximum value in the NPSH. This is because, through geostrophic balance, winds are linked to gradients in geopotential height rather than its magnitude. Additionally, geopotential heights tend to systematically shift upward under global warming. Our metric in Fig. 5.4 accounts for all of these factors.

On the larger scale, changes in the location and the strength of the NPSH in the fast

¹A comparison between Figs. 5.3 e and l shows that $q_s(T)$ and $\delta q_s(T)$ are of similar magnitude. This is due to the nonlinear dependence of $q_s(T)$ on temperature, which gives rises to big changes in $q_s(T)$ even for small changes in T . For instance, the water vapor saturation pressure is 3523 Pa at 300 K and 4701 Pa at 305 K, which implies that for only 5K difference in temperature, the water vapor saturation pressure differs by around 33%.

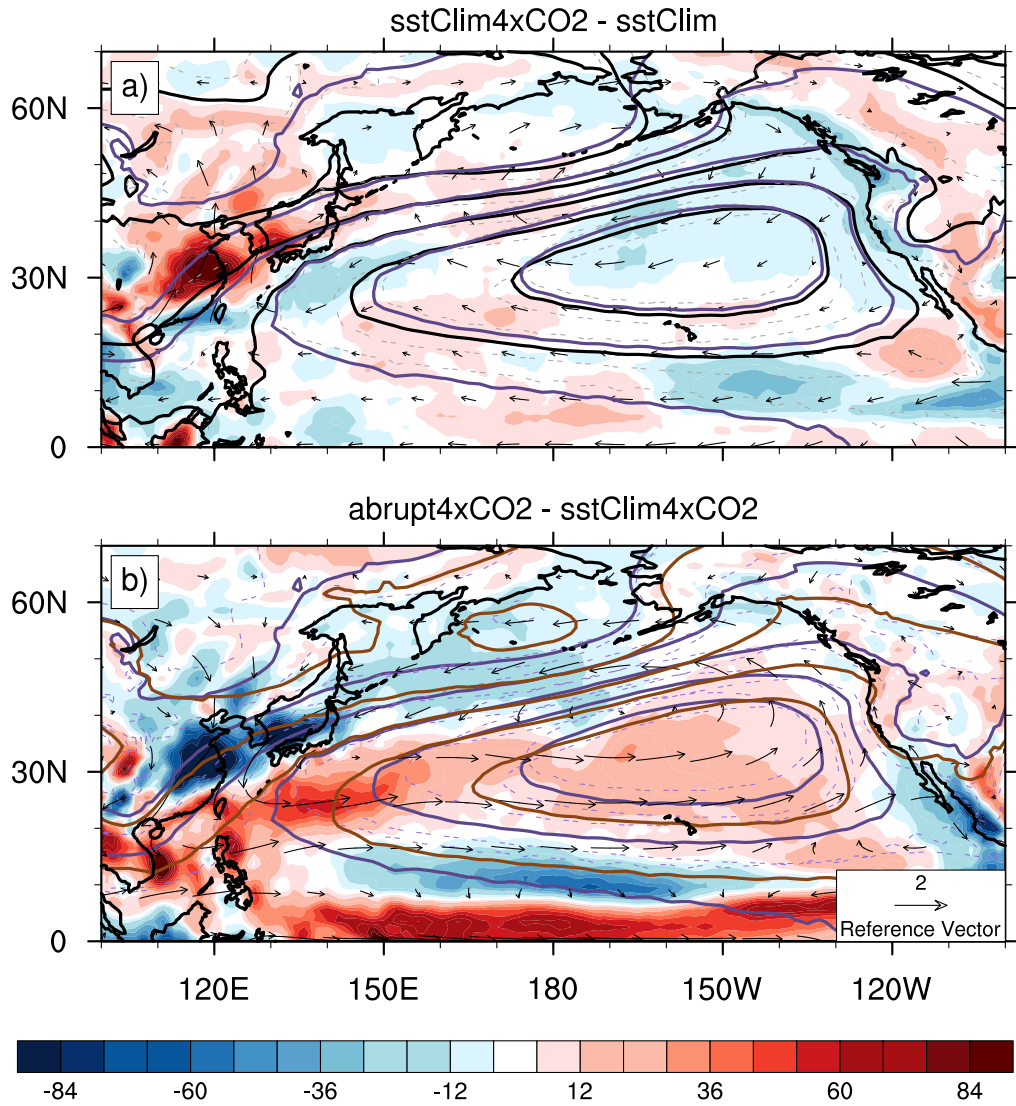


Figure 5.4 MMM anomalies of precipitation (shading, W/m^2) due to winds, winds at 850 mb (vector, m/s), and difference in geopotential height between its maximum and locational value (line contour, contour interval 30 m, solid black, purple and brown lines indicate sstClim, sstClim4xCO2, and abrupt4xCO2, respectively) at 850 mb in the fast (a) and slow (b) responses. Short dash lines in black and purple indicate the inter-model spread (1 standard deviation) in sstClim and sstClim4xCO2 simulations.

response are within one standard deviation of the inter-model spread and therefore not significant. In the slow response, instead, the NPSH moves southward and weakens significantly. This implies that changes in winds over the EASM region are mostly local responses in the fast response, while resulting from a combination of local and remote responses, mediated

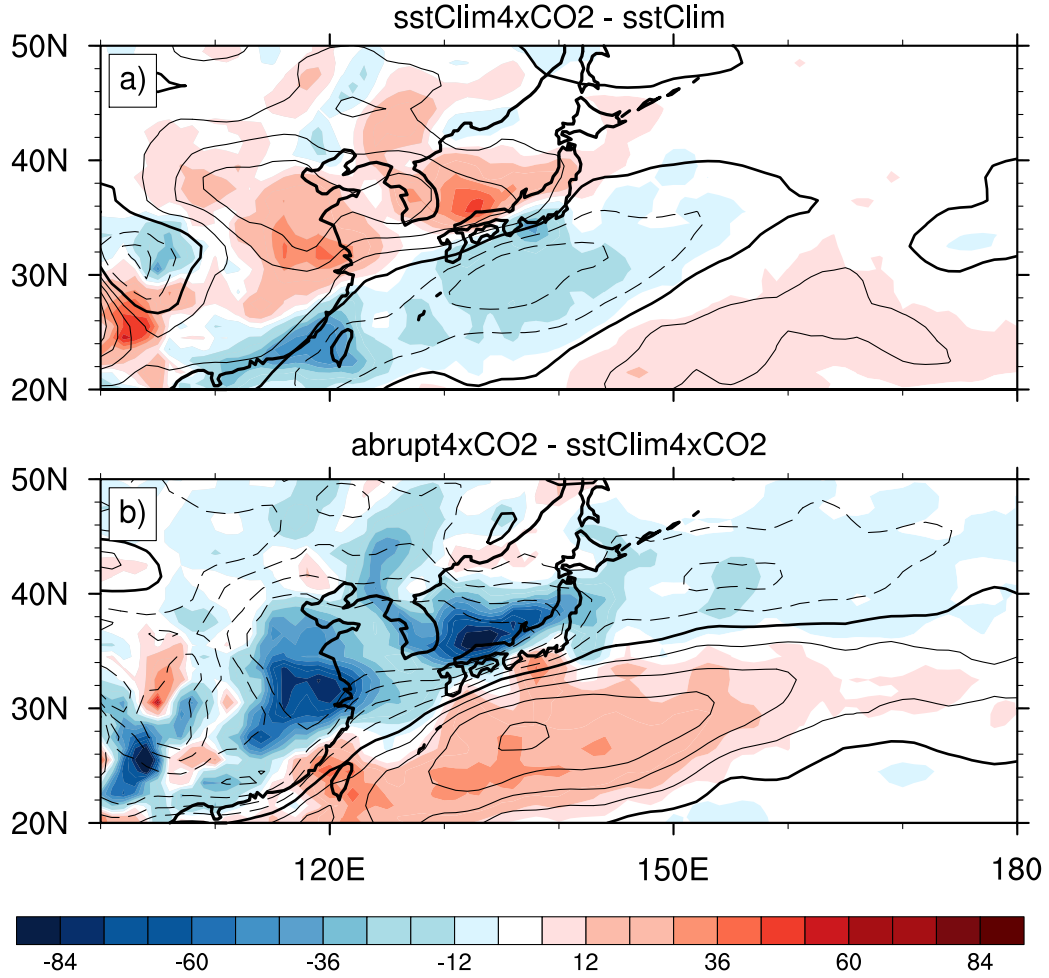


Figure 5.5 MMM anomalies of climatological moisture weighted wind convergence (shading, W/m^2) and vertical velocity at 500 mb (line contour, contour interval 0.005 Pa/s). Solid/dash line indicates ascending/descending motion.

by the NPSH, in the slow response.

The dynamic moisture flux convergence anomalies, $(-\langle \nabla \cdot q_0 \delta \mathbf{v} \rangle)$, can be further decomposed into a wind convergence component, $(-\langle q_0 \nabla \cdot \delta \mathbf{v} \rangle)$, and an advection component, $(-\langle \delta \mathbf{v} \cdot \nabla q_0 \rangle)$. The wind convergence component, $(-\langle q_0 \nabla \cdot \delta \mathbf{v} \rangle)$, can be expressed in terms of the vertical advection using continuity, $-\langle \delta \omega \partial_p q_0 \rangle$. The change in this term is largely explained by changes in vertical velocity at 500 mb (i.e., $\delta \omega_{500}$, Fig. 5.5).

The vertical velocity is directly associated with remote forcing (i.e., energy advection), local radiative and surface fluxes, and stability. According to the MSE budget (Chen and

Bordoni 2014), vertical velocity can be approximated as the fraction between energy input and moist static stability. Here, we define a proxy for vertical velocity at 500 mb based on the MSE budget,

$$\omega_{500\text{apprx}} = \frac{-\langle \mathbf{v} \cdot \nabla E \rangle + F^{\text{net}}}{-\alpha \langle \partial_p h \rangle}, \quad (5.5)$$

where $F^{\text{net}} = S_t^\downarrow - S_t^\uparrow - S_s^\downarrow + S_s^\uparrow - R_t^\uparrow + R_s^\uparrow - R_s^\downarrow + SH + LH$, $h = c_p T + gz + L_v q$ is the MSE, $E = c_p T + L_v q$ is the atmospheric moist enthalpy, and F^{net} is the net energy flux into the atmosphere, with the subscript t and s denoting the top of atmosphere and surface, respectively.² α is a coefficient added to account for the coupling between vertical velocity and MSE stratification. Transient eddies are ignored and the coupling coefficient α is assumed to be homogeneous for simplicity. Fig. 5.6 shows changes in vertical velocity as diagnosed from the model output directly and from the approximation in Eq. 7.1 (i.e., δw and assuming $\alpha = 1$).

At the first order, changes in vertical velocity can be partitioned into changes in energy input and changes in stability (Appendix). Contributions from changes in energy input (mostly from horizontal advection of moist enthalpy) are significantly larger than those from changes in stability in both fast and slow responses (Fig. 5.7). In the fast response, anomalous positive moist enthalpy advection over Northeast China and negative moist enthalpy advection over the climatological rainfall band are closely associated with changes in vertical velocity. In the slow response, anomalies in moist enthalpy advection change sign, with anomalous positive moist enthalpy advection over ocean and negative advection over land. Contributions from local stability are considerably smaller, however, with a destabilizing effect over land in the fast response and over oceanic regions in the slow response. Anomalies in moist enthalpy advection are due to both dry enthalpy and latent energy advection, with similar spatial pattern (not shown) because of close relationship between temperature and water vapor changes via the Clausius-Clapeyron relationship.

²The vertical integration of moist static energy stratification is from 700 mb to 100 mb to account for the steepest slope for stability.

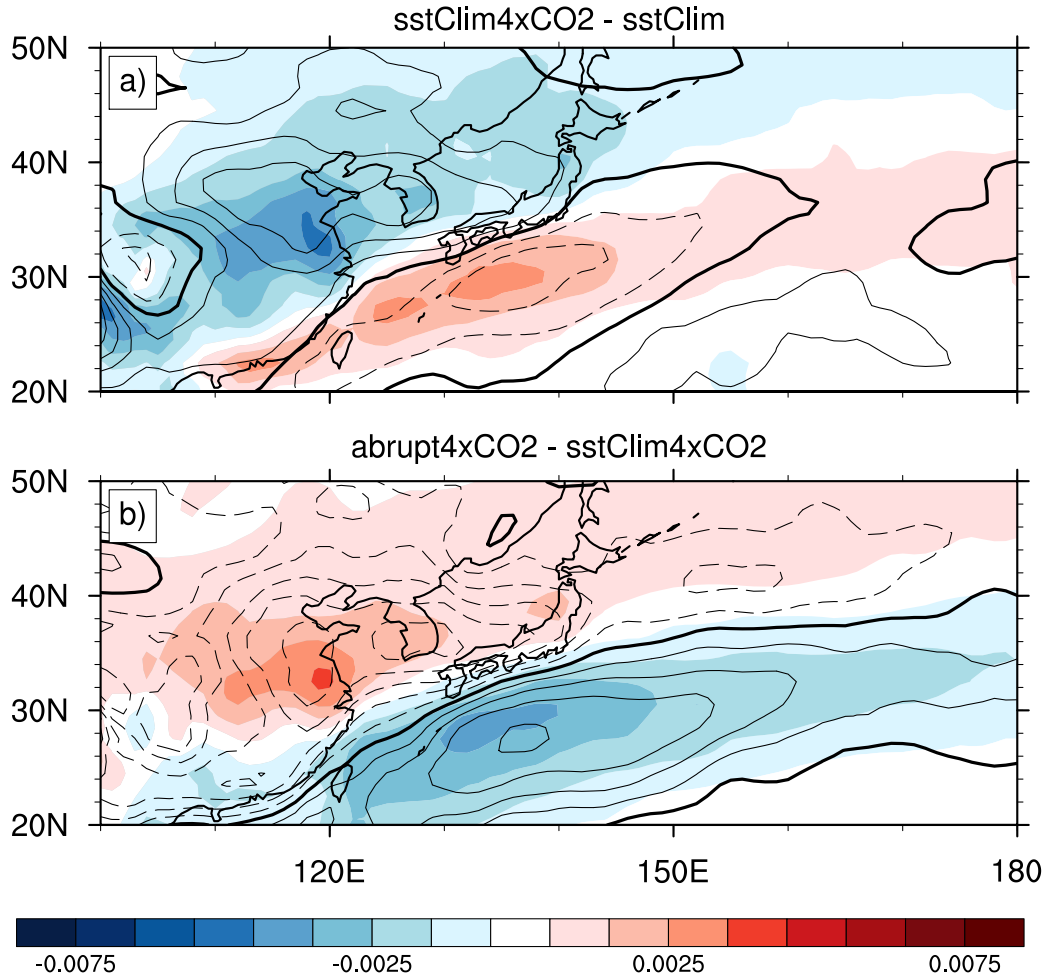


Figure 5.6 MMM anomalies of approximated vertical velocity $\omega_{500\text{apprx}}$ (Eq. 7.1, shading, Pa/s) and MMM anomalies of climatological vertical velocity at 500 mb (line contour, contour interval 0.005 Pa/s). Solid/dash line indicates ascending/descending motion. $\omega_{500\text{apprx}}$ is multiplied by a factor of 2 in the fast response (a).

Changes in the advection term ($-\langle \delta \mathbf{v} \cdot \nabla q_0 \rangle$) are a direct result from (mostly geostrophic) wind anomalies. In the fast and slow responses, changes in local precipitation over East China and adjacent oceanic regions are highly associated with meridional wind anomalies (Fig. 5.8 b, d). Intensified (weakened) meridional wind enhances (reduces) moisture transport, resulting in higher (lower) rainfall. In addition, the meridional component of the geostrophic flow on a β plane can induce convergent flow, which reinforces local precipitation in addition to positive advective anomalies. Changes in meridional wind at 850 mb are largely geostrophic, a consequence from changes in surface pressure gradient through geopotential

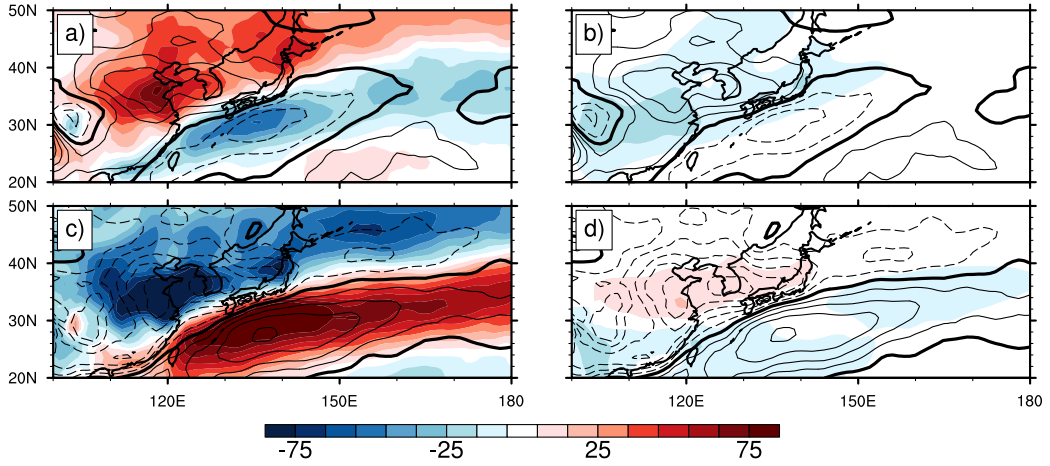


Figure 5.7 MMM anomalies of energy input (a and c, first term in Eq. 7.2, shading, W/m^2), fractional changes in stability weighted by climatological energy input (b and d, second term in Eq. 7.2, shading, W/m^2), and climatological vertical velocity at 500 mb (line contour, contour interval 0.005 Pa/s) in the fast (a and b) and slow (c and d) responses. Solid/dash line indicates ascending/descending motions.

height (Z_{850}) gradient anomalies. For simplicity, ignoring subtle influences from changes in the atmospheric temperature between the surface and 850 mb pressure level, Z_{850} is only dependent on $\ln(p_s)$, where p_s indicates surface pressure. Anomalies in locational differences in surface pressure, i.e., $\delta \ln(p_{s1}/p_{s2})$ will change the Z_{850} gradient, and thereafter create wind anomalies, δv_{850} . In the fast response, enhanced land-sea contrast is manifest in an increased surface pressure gradient, with lower pressure over land and higher pressure over ocean. Meridional wind is subsequently enhanced. In the slow response, however, land-sea contrast is weakened, and the meridional wind is reduced. This relationship is well observed amongst different model simulations (Fig. 5.9).³ Changes in precipitation over the oceanic rainfall band, however, are largely due to changes in zonal wind, particularly in the slow response (Fig. 5.8 c). Enhanced lower-level westerly wind might be related to a southward displacement of the NPSH. In the fast response, the NPSH does not feature significant changes in its spatial pattern, which might be the reason why contributions from anomalous advection of climatological moisture are limited.

³The robustness of the relationship between $\delta \ln(p_{s1}/p_{s2})$ and δv_{850} is insensitive to the width of the region we choose (the East boundary varies from 130E to 140E).

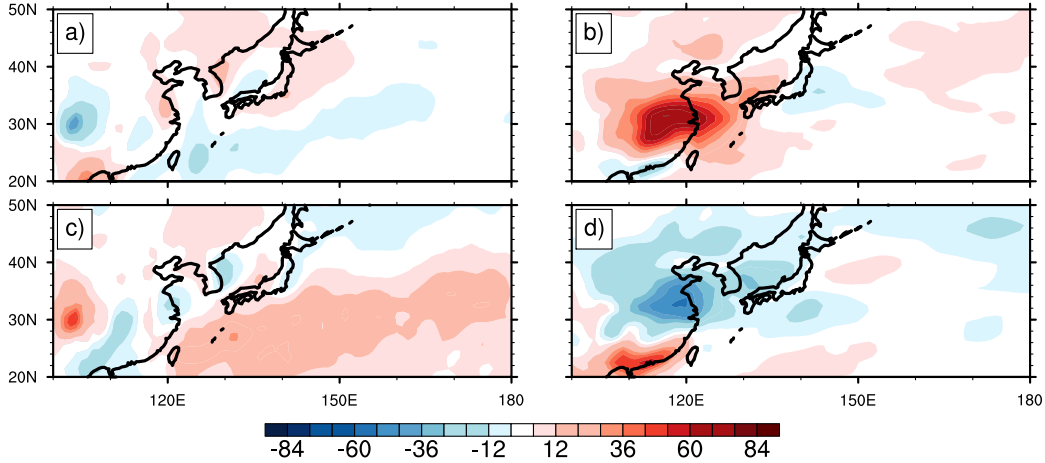


Figure 5.8 Zonal (a, c) and meridional (b, d) components of MMM anomalies of climatological moisture advection at 850 mb (shading, W/m^2) in the fast (a, b) and slow (c, d) responses.

c. Summary

We have diagnosed precipitation changes in the EASM region in both fast and slow responses. Some robust conclusions emerging from this diagnosis include:

- Changes in net precipitation are associated with changes in the moisture flux convergence, which is dominated by the dynamic component (i.e., by changes in circulation);
- The wind convergence term in the dynamic component is directly linked to changes in vertical velocity through continuity;
- These changes in vertical velocity are found to be mostly related to changes in moist enthalpy advection, with changes in vertical stability playing a lesser role;
- Changes in horizontal moisture advection over East China are dominated by changes in the meridional wind, which is a consequence of changes in land-sea contrast. The zonal component dominates the slow response over the oceanic regions, as a possible consequence of the southward displacement of the NPSH.

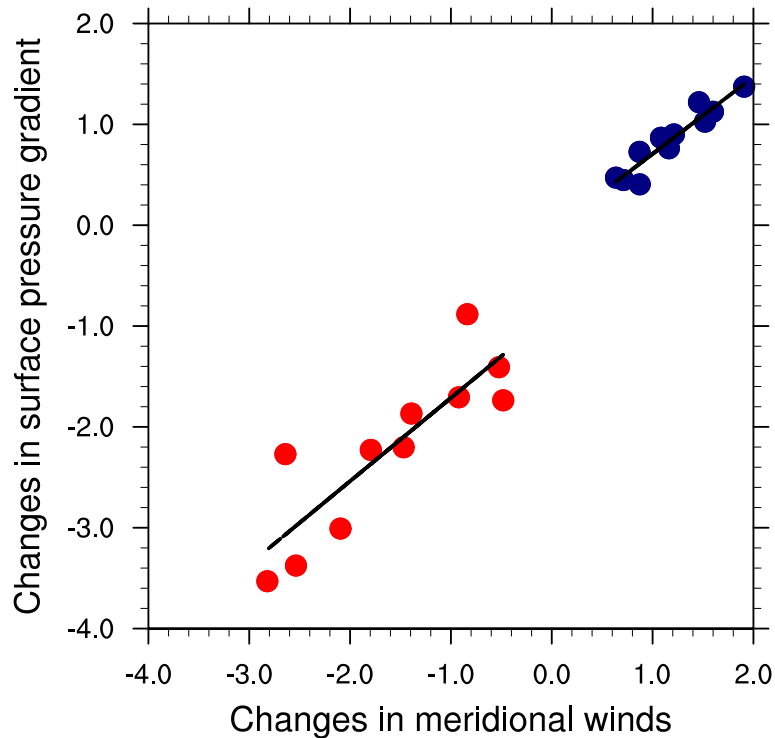


Figure 5.9 Scatterplot (blue/red for fast/slow reponse) of meridional wind anomaly over East China and adjacent oceans (25N-40N, 110E-130E) and surface pressure gradient anomaly between land (100E-120E) and ocean (130E-150E) over 25N-40N band. Each dot represents one model output as indicated in Table 5.1. Solid line indicates linear regression line in fast/slow response, respectively. See text for more details.

5.3. Numerical simulations

We use the GFDL AM2.1 to investigate the impact of land warming and SST patterns on the EASM response to CO_2 forcing. We have previously shown that topography plays an essential role in the rainfall band formation (Chen and Bordoni 2014, Chapter 3 of this thesis). As discussed in Chapter 3, the presence of topography reinforces the land-sea thermal contrast, in addition to its mechanical interactions with the prevailing flow. However, in a changing climate, can enhanced land-sea thermal contrast due to land warming alone provide a large enough forcing to cause changes in precipitation? In addition, how do changes in

SST patterns affect the response of the EASM?

a. Land warming

In order to expose impacts of land warming alone on the EASM, we design two experiments with changing CO₂ concentration in the absence of global topography: noTopo_control and noTopo_4xCO2. Fig. 5.10 shows the simulated precipitation change in May, June, and July with and without topography. Consistent with our previous study (Chen and Bordoni 2014), in the presence of topography, a well organized rainfall band is simulated during the EASM season: the rainfall band disappears when topography is removed. In the absence of topography (Fig. 5.10, right), there are no significant changes in precipitation until July, when the rainfall band dissipates even in the control experiment (with topography). The difference highlights the limited impact of land warming alone on the EASM rainfall, and emphasizes the importance of topography in its response to CO₂ forcing.

b. SST patterns

Previous literature (e.g., Xie et al. 2010) has discussed the importance of SST patterns in regional precipitation changes, arguing that the “wet get wetter” response can hold only for uniform SST changes. We illustrate the impact of spatially varying SST patterns on the projected EASM rainfall by comparing the Uni4K and CMIP5SST experiments (Fig. 5.11). With spatially varying SSTs (Fig. 5.12), rainfall increases from East China through the northwestern Pacific; rainfall instead decreases over Japan and part of the northwestern Pacific in the case of uniform SST warming. In the latter case, changes in regional net precipitation do not follow the pattern of the climatological net precipitation, as would be expected from the “wet get wetter” response.

Differences in rainfall projection are largely due to the dynamic component (Fig. 5.13) in the moisture budget. With spatially varying SSTs, the NPSH weakens and moves south-

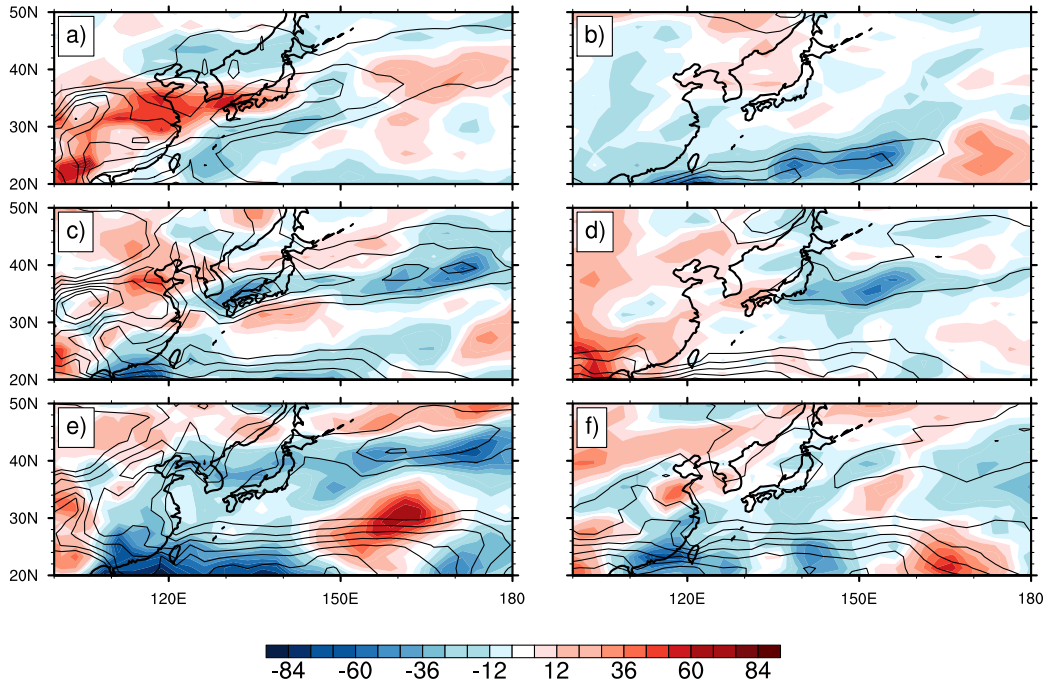


Figure 5.10 GFDL AM2.1 simulations of precipitation (shading, W/m^2) in the fast response with full topography (left) and without topography (right) in May (a,b), June (c,d), and July (e,f). Line contour (contour interval 1 mm/day, 3 – 9 mm/day) indicates climatological precipitation in each comparison.

ward, which is associated with a southward displacement of the westerly jet (Fig. 5.12a). The weakening of the NPSH, together with its spatial displacement, creates an anomalous westerly wind to the southeast of Japan, resembling the MMM response in CMIP5 simulations. With uniform SST warming, the NPSH intensifies and there is little evidence of any southward displacement. As a consequence, the prevailing wind to the southeast of Japan is northeasterly, which results in a reduction in precipitation.

5.4. Summary and discussion

In this Chapter, we analyzed the response of the EASM rainfall band to atmospheric CO_2 forcing and subsequent SST warming within the context of the moisture budget. The spatial pattern of net precipitation changes is dominated by changes in mean moisture flux

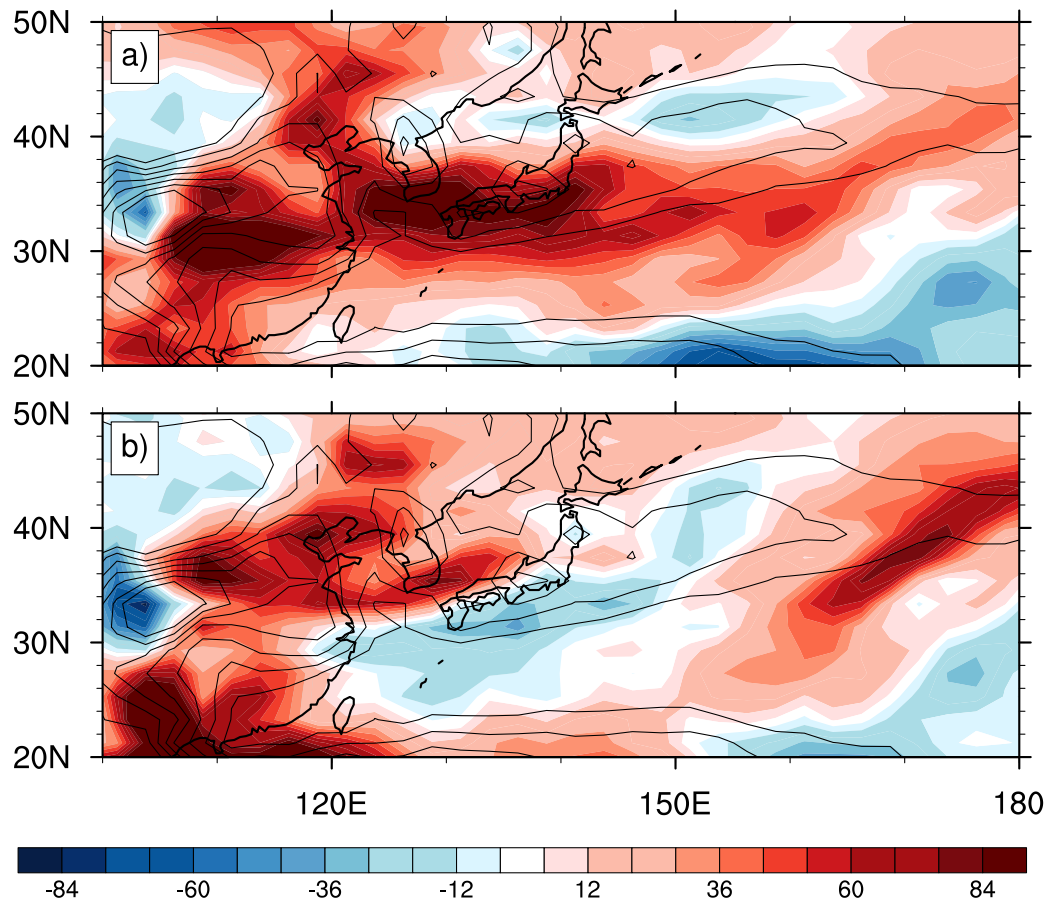


Figure 5.11 GFDL AM2.1 simulations of precipitation in June (shading, W/m^2) with CMIP5 anomalous SST pattern (a) and with 4K uniform SST increase (b). Line contour (contour interval 1 mm/day, 3 – 9 mm/day) indicates climatological precipitation.

convergence, which in turn is primarily explained by changes in circulation. The thermodynamic component however is non-negligible; it mimics the net precipitation climatology and contributes significantly to rainfall changes under warming. Surface pressure anomalies, as a consequence of land-sea contrast due to CO_2 forcing, create an anomalous meridional flow over East China and adjacent oceans, which affects the moisture advection. The NPSH weakens and moves significantly southward in the slow response, creating an anomalous westerly flow to the south of the climatological rainfall band and subsequently increasing moisture advection. In addition to contributions from anomalous moisture advection due to winds, anomalous wind convergence also contributes to rainfall changes. The spatial pattern

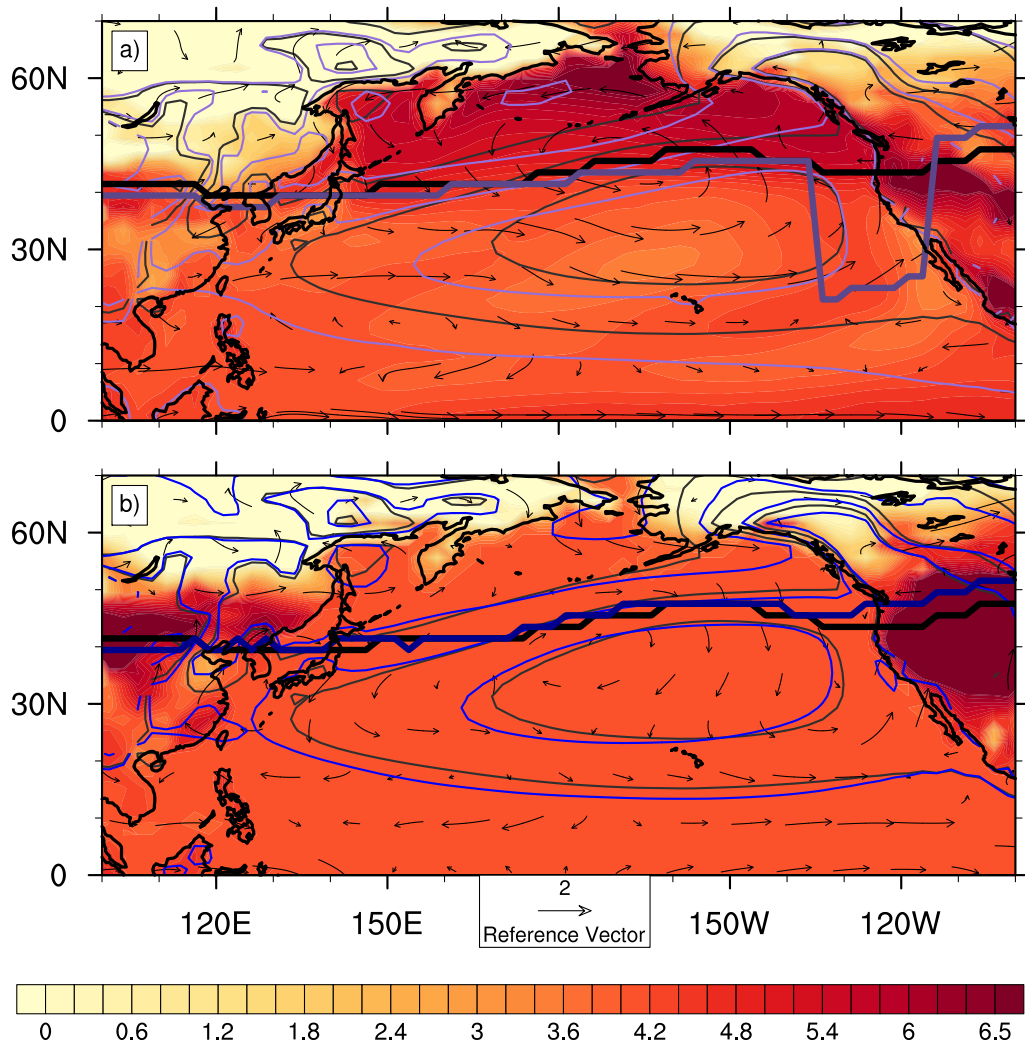


Figure 5.12 GFDL AM2.1 simulations of surface temperature (shading, W/m^2), 850 mb winds (vector) and the westerly core (maximum westerly wind, black indicates climatology, purple and blue indicate simulations with CMIP5 anomalous SST pattern and 4K uniform SST increase, respectively) with CMIP5 anomalous SST pattern (a) and with 4K uniform SST increase (b).

is colocated with that of vertical velocity anomaly at 500 mb, which can be thought of as a response to a remote forcing, provided by anomalous horizontal moist enthalpy advection.

Numerical simulations without topography show that enhanced land-sea contrast due to land warming alone cannot induce similar precipitation changes. This result implies that the land warming is not a sufficient condition for the EASM rainfall changes. It also emphasizes the important role of topography in the EASM response in terms of its climatology and

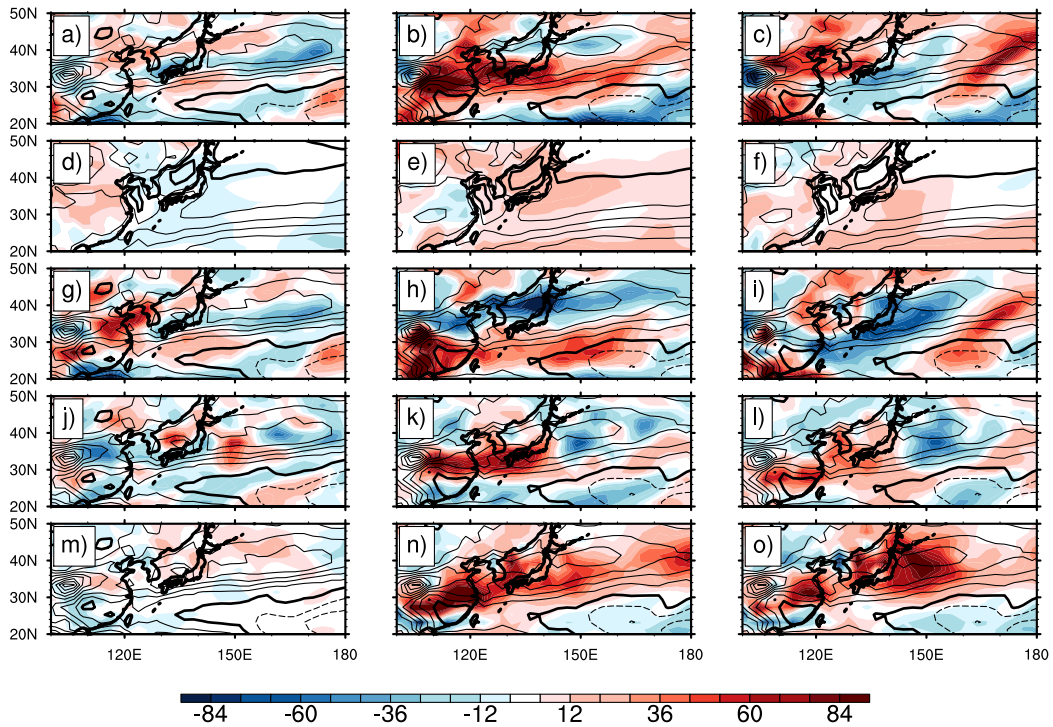


Figure 5.13 GFDL AM2.1 simulations of net precipitation (a-c), evaporation (d-f), wind component (g-i), relative humidity component (j-l) and temperature component (m-o) as in Fig. 5.2 for fast response (left), slow response (middle), and slow response with uniform 4K increase in SSTs (right) with full topography. Line contour (contour interval 1 mm/day, 3 – 9 mm/day) indicates climatological precipitation in each comparison.

climate change. In addition, spatially varying SST changes are shown to play a key role in rainfall changes in the oceanic regions through associated changes in the NPSH.

The fast and slow responses of the EASM to CO_2 forcing show an opposite pattern, implying a compensating effect in transient climate change. This result is consistent with recent work by Shaw and Voigt (2015), who highlight how changes in land-sea contrast in response to the direct radiative forcing and the indirect SST warming have an opposite impact on global circulation change. Speaking of the EASM specifically, we acknowledge the importance of land-sea contrast but emphasize the role of topography rather than that of land warming alone. Our simulations are based on GCM experiments with realistic continents, rather than the more idealized study by Shaw and Voigt (2015), who prescribe SSTs to artificially introduce land-sea contrast in their aquaplanet simulations.

Results emerging from this work have important implications for improving EASM projections in GCMs. The dynamic component due to circulation changes, though highly model dependent and hard to constrain, can disclose mechanisms through which different forcing agents influence the EASM. The thermodynamic component mimics the climatology. Therefore, a better representation of the climatological precipitation will be the first necessary step to reduce spread in regional precipitation projections. In addition, analysis of the results from the fast response highlight how dramatic changes in rainfall can occur even as a direct response to CO₂ forcing, without any SST warming. These changes can have a tremendous societal impact on heavily populated monsoon regions. This confirms how geo-engineering schemes that have been proposed as climate mitigation strategies and that only aim at reducing surface warming without CO₂ sequestration might have unexpected implications for the global and regional hydrological cycle (Bony et al. 2013a; O’Gorman et al. 2012).

Chapter 6

Conclusions

Observational analyses of the energetics of the EASM in present-day climate show that horizontal advection of moist enthalpy, rather than local thermodynamic forcing, plays a central role in its existence and seasonality. The horizontal moist enthalpy advection is in turn primarily associated with stationary quantities, such as zonal asymmetries in the zonal temperature gradient and in the meridional velocity. Numerical simulations show how the TP exerts a profound influence on the EASM formation primarily by enhancing the stationary eddy meridional wind, rather than by reinforcing the longitudinal thermal gradient. The enhanced meridional stationary eddy velocity throughout the whole troposphere increases dry enthalpy advection into the EASM region significantly, which supports the formation of a well-organized rainfall band. At upper levels, increases in the meridional stationary wind are linked to the acceleration of the deflected westerly jet over Northeast China; at lower levels, the enhanced meridional stationary eddy velocity represents the northwestern flank of the NPSH. In the absence of the TP, the NPSH narrows in latitude meridionally and gets elongated zonally, which allows its western flank to penetrate into the inner Asian continent (Rodwell and Hoskins 2001). As a result, these changes in the NPSH result in a significant weakening of the southerly wind over the EASM region. In the presence of the TP, the northwestern flank of the NPSH is more tilted, resulting in an anomalous southerly wind therein.

The GFDL AM2.1 simulations provide support to this mechanism. However, there are

a few caveats to keep in mind. The first one is that the choice of prescribed SSTs reduces the changes in the NPSH in the lower troposphere. Therefore, we choose 750 mb (above the boundary layer, where the wind response is less affected by the prescribed SSTs) to diagnose how topography shapes the NPSH (Fig. 6.1). Another limitation is that the geopotential height might not be a good proxy for winds where the ageostrophic component might not be small, such as mountainous regions. With consideration of these caveats, we focus only on the North Pacific region. In the presence of topography (Fig. 6.1, top), the NPSH is spatially limited over the Pacific, with a relatively more tilted structure in its northwestern flank; in the absence of topography (Fig. 6.1, bottom), the NPSH is strongly weakened. Additionally, it penetrates into the Asian continent and shows a relatively flat spatial structure, with its western boundary limited by a low pressure system over the Indian continent, and its northwestern flank by the westerly winds.

The importance of the meridional stationary eddy velocity in the EASM formation is investigated in CMIP5 current climate simulations. The spatial correlation between simulated EASM precipitation and stationary southerly wind is found to be high amongst all available model outputs. The inter-model spread of EASM rainfall amount can be largely explained by stationary meridional wind convergence.

In a changing climate, the dynamic component due to circulation changes plays an important role in setting up the spatial pattern of net precipitation changes. Rainfall changes due to wind convergence and moisture advection are both important. The rainfall anomaly due to the wind convergence is largely explained by changes in moist enthalpy advection. The rainfall anomaly due to moisture advection is dominated by changes in meridional wind over land and zonal wind over the ocean: over East China, changes in meridional wind are a direct consequence of land-sea thermal contrast; over the oceanic regions, changes in the zonal wind are modulated by changes in the larger-scale circulation pattern of the NPSH. Numerical simulations reveal the importance of topography and spatial SST patterns in rainfall changes in the EASM region.

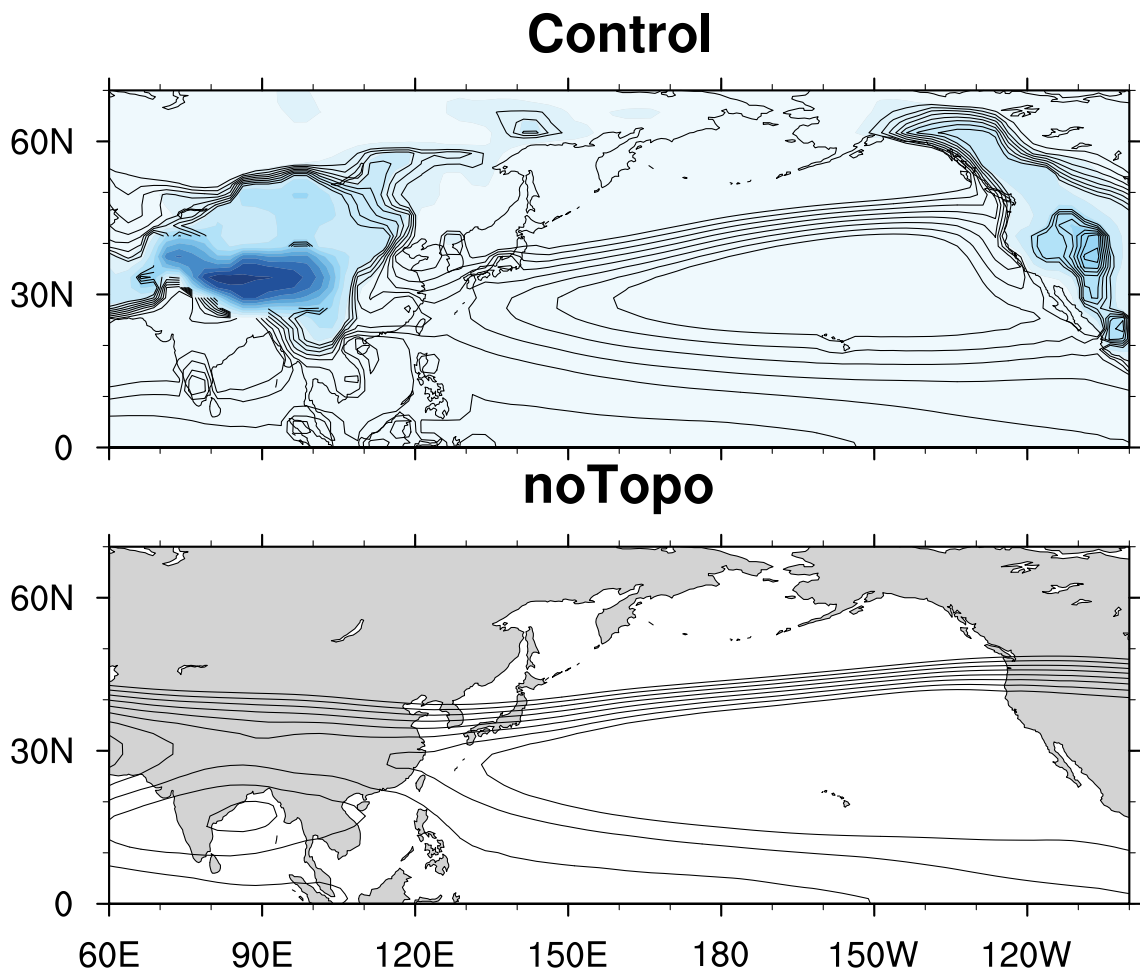


Figure 6.1 GFDL AM2.1 simulations of geopotential height at 750 mb in the presence (top) and absence (bottom) of global topography. Color shading indicates topography height.

Climatology

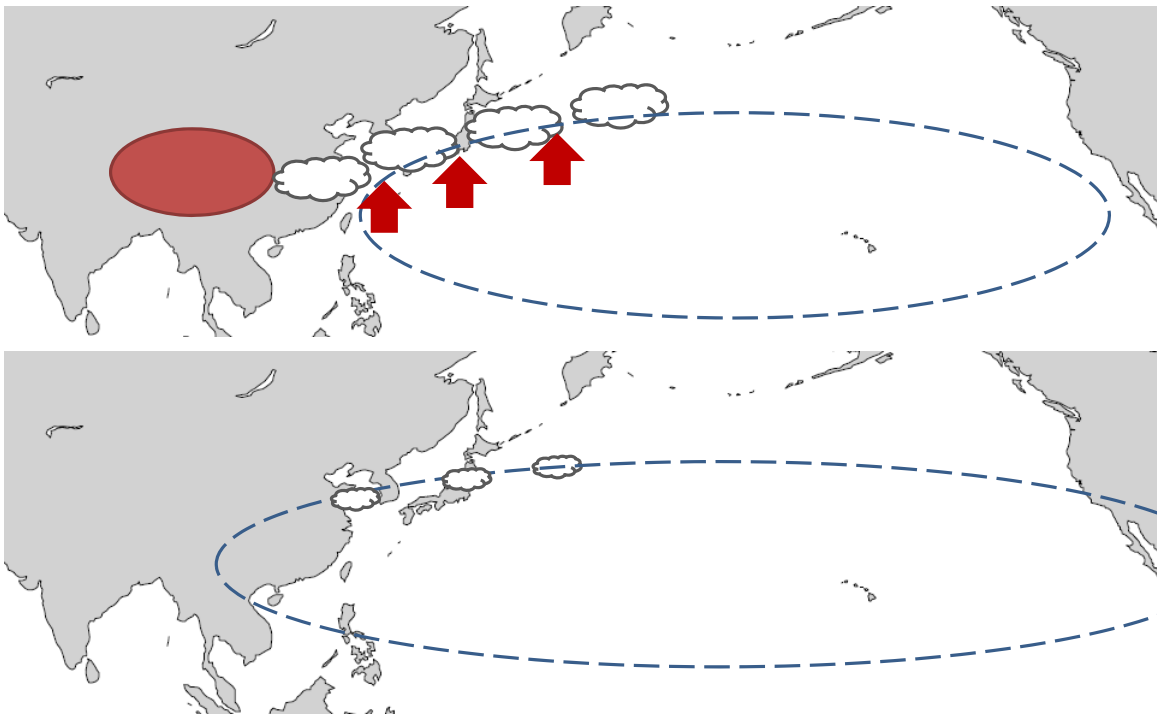


Figure 6.2 Schematic of the role of the TP (red oval) in the NPSH (dashed lined) and the EASM in present-day climate.

In summary, observational studies show that southerly wind plays an important role in the energetics of the EASM. The TP affects the rainfall band formation primarily through the meridional stationary wind velocity (Fig. 6.2 top). In the absence of the TP, the NPSH expands more widely and significantly weakens the southerly wind in the EASM region. As a result, the rainfall band disappears (Fig. 6.2 bottom). In the fast response to CO_2 forcing, enhanced land-sea thermal contrast reinforces the meridional wind, which results in an increase of rainfall over East China (Fig. 6.3). In the slow response, the land-sea thermal contrast is weakened because of sea surface warming, and the rainfall over East China decreases. The NPSH moves southward, causing the rainfall band to move southward (Fig. 6.4).

Fast response

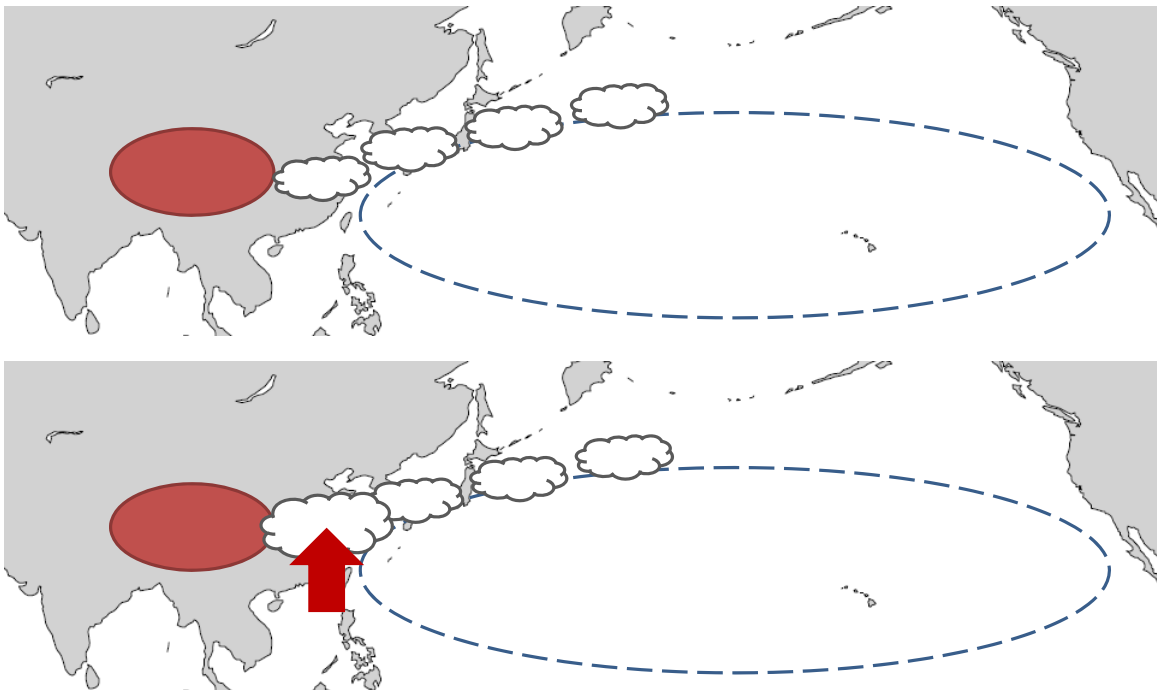


Figure 6.3 Schematic of the fast response of the EASM to CO₂ forcing. Notation as in Fig. 6.2.

Slow response

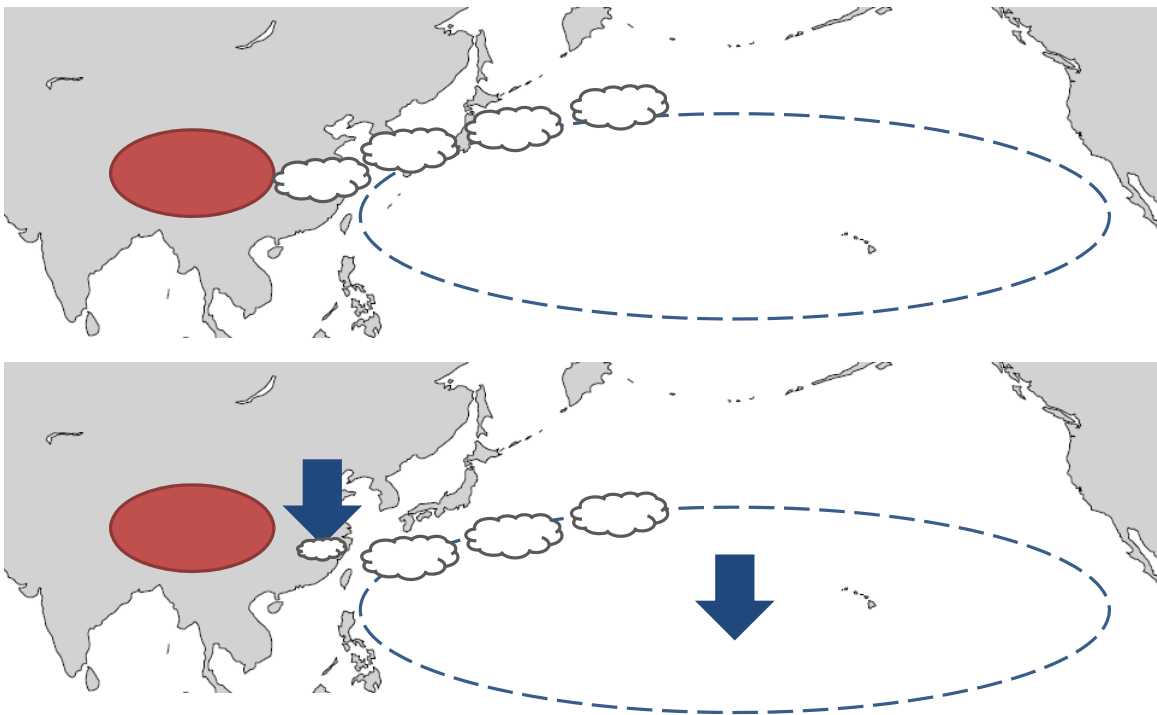


Figure 6.4 Schematic of the slow response of the EASM to CO₂ forcing. Notation as in Fig. 6.2.

Chapter 7

Appendix: Decomposition of the approximated vertical velocity

We use a , s , and w to represent energy input ($-\langle \mathbf{v} \cdot \nabla E \rangle + F^{\text{net}}$), stability ($\langle \partial_p h \rangle$) and approximated vertical velocity at 500 mb ($\omega_{500\text{apprx}}$). Therefore, Eq. 5.5 can be expressed symbolically as $w = \frac{a}{\alpha s}$. Changes in vertical velocity (δw) can be expressed as

$$\frac{\delta w}{w_0} = \frac{\delta a}{a_0} - \frac{\delta s}{s_0}, \quad (7.1)$$

where the subscript 0 indicates the control experiment, which is sstClim (sstClim4xCO2) in the fast (slow) response. Because a_0 approximates to zero in some regions, we reformulate Eq. 7.1 by multiplying a_0 on both sides of the equation,

$$\frac{a_0 \delta w}{w_0} = \delta a - \frac{a_0 \delta s}{s_0}. \quad (7.2)$$

One advantage of this approach is that we can avoid imposing an empirical value of α while still being able to diagnose respective contributions.

Bibliography

- Abe, M., T. Yasunari, and A. Kitoh, 2004: Effects of Large-scale Orography on the Coupled Atmosphere-Ocean System in the Tropical Indian and Pacific Oceans in Boreal Summer. *J. Meteor. Soc. Japan*, **82** (2), 745–759.
- Adler, R. F., G. J. Huffman, D. T. Bolvin, S. Curtis, and E. J. Nelkin, 2000: Tropical rainfall distributions determined using trmm combined with other satellite and rain gauge information. *J. Appl. Meteor.*, **39** (12), 2007–2023.
- Adler, R. F., J.-J. Wang, G. Gu, and G. J. Huffman, 2009: A ten-year tropical rainfall climatology based on a composite of trmm products. *J. Meteor. Soc. Japan*, **87** (0), 281–293.
- Anderson, J., et al., 2004: The new GFDL global atmosphere and land model AM2-LM2: Evaluation with prescribed SST simulations. *J. Climate*, **17** (24), 4641–4673.
- Berrisford, P., P. Kållberg, S. Kobayashi, D. Dee, S. Uppala, A. Simmons, P. Poli, and H. Sato, 2011: Atmospheric conservation properties in ERA-Interim. *Quart. J. R. Met. Soc.*, **137** (659), 1381–1399.
- Bony, S., G. Bellon, D. Klocke, S. Sherwood, S. Fermepin, and S. Denvil, 2013a: Robust direct effect of carbon dioxide on tropical circulation and regional precipitation. *Nature Geoscience*, **6** (6), 447–451.
- Bony, S., et al., 2013b: Carbon dioxide and climate: perspectives on a scientific assessment. *Climate Science for Serving Society*, Springer, 391–413.

- Boos, W. R. and J. V. Hurley, 2013: Thermodynamic Bias in the Multimodel Mean Boreal Summer Monsoon. *J. Climate*, **26** (7), 2279–2287.
- Ceppi, P., Y.-T. Hwang, D. M. Frierson, and D. L. Hartmann, 2012: Southern Hemisphere jet latitude biases in CMIP5 models linked to shortwave cloud forcing. *Geophys. Res. Lett.*, **39** (19).
- Chen, H., T. Zhou, R. B. Neale, X. Wu, and G. J. Zhang, 2010: Performance of the new NCAR CAM3. 5 in east asian summer monsoon simulations: Sensitivity to modifications of the convection scheme. *Journal of Climate*, **23** (13), 3657–3675.
- Chen, J. and S. Bordoni, 2014: Orographic Effects of the Tibetan Plateau on the East Asian Summer Monsoon: An Energetic Perspective. *J. Climate*, **27** (8), 3052–3072.
- Chen, T. and C. Chang, 1980: The structure and vorticity budget of an early summer monsoon trough (Mei-Yu) over southeastern China and Japan. *Mon. Wea. Rev.*, **108** (7), 942–953.
- Chou, C. and J. Neelin, 2003: Mechanisms Limiting the Northward Extent of the Northern Summer Monsoons over North America, Asia, and Africa. *J. Climate*, **16** (3), 406–425.
- Chou, C., J. Neelin, and H. Su, 2001: Ocean-atmosphere-land feedbacks in an idealized monsoon. *Quart. J. R. Met. Soc.*, **127** (576), 1869–1891.
- Dao, L. and S. Chen, 1957: The structure of general circulation over continent of Asia in summer [J]. *Acta Meteorol. Sin.*, **3**, 005.
- Dee, D., et al., 2011: The ERA-Interim reanalysis: Configuration and performance of the data assimilation system. *Quart. J. R. Met. Soc.*, **137** (656), 553–597.
- Dima, I. and J. M. Wallace, 2003: On the Seasonality of the Hadley Cell. *J. Atmos. Sci.*, **60**, 1522–1527.

- Ding, Y., 1992: Summer monsoon rainfalls in China. *J. Meteor. Soc. Japan*, **70** (1), 397–421.
- Ding, Y. and J. Chan, 2005: The East Asian summer monsoon: An overview. *Meteor. Atmos. Phys.*, **89** (1), 117–142.
- Enomoto, T., B. J. Hoskins, and Y. Matsuda, 2003: The formation mechanism of the Bonin high in August. *Quart. J. R. Met. Soc.*, **129** (587), 157–178.
- Flohn, H., 1957: Large-scale aspects of the “summer monsoon” in South and East Asia. *J. Meteor. Soc. Japan*, **75**, 180–186.
- Gao, H. and S. Yang, 2009: A severe drought event in northern China in winter 2008–2009 and the possible influences of La Niña and Tibetan Plateau. *J. Geophys. Res.*, **114** (D24), D24104.
- Gao, H., S. Yang, A. Kumar, Z. Hu, B. Huang, Y. Li, and B. Jha, 2011: Variations of the East Asian Mei-yu and simulation and prediction by the NCEP climate forecast system. *J. Climate*, **24** (1), 94–108.
- He, C. and T. Zhou, 2015: Responses of the western north pacific subtropical high to global warming under rcp4.5 and rcp8.5 scenarios projected by 33 cmip5 models: The dominance of tropical indian ocean–tropical western pacific sst gradient. *Journal of Climate*, **28** (1), 365–380.
- Held, I. M. and B. J. Soden, 2006: Robust responses of the hydrological cycle to global warming. *Journal of Climate*, **19** (21), 5686–5699.
- Held, I. M., M. Ting, and H. Wang, 2002: Northern winter stationary waves: Theory and modeling. *J. Climate*, **15**, 2125–2144.
- Hirahara, S., H. Ohno, Y. Oikawa, and S. Maeda, 2012: Strengthening of the Southern Side of the Jet Stream and Delayed Withdrawal of Baiu Season in Future Climate. *J. Meteor. Soc. Japan. Ser. II*, **90** (5), 663–671.

- Hsu, P., T. Li, H. Murakami, and A. Kitoh, 2013: Future Change of the Global Monsoon Revealed from 19 CMIP5 Models. *J. Geophys. Res. Atmos.*, **18**, 1247–1260.
- Huang, D.-Q., J. Zhu, Y.-C. Zhang, and A.-N. Huang, 2013: Uncertainties on the simulated summer precipitation over Eastern China from the CMIP5 models. *J. Geophys. Res.-Atmos.*
- Huffman, G., R. Adler, M. Morrissey, D. Bolvin, S. Curtis, R. Joyce, B. McGavock, and J. Susskind, 2001: Global Precipitation at One-Degree Daily Resolution from Multisatellite Observations. *J. Hydrometeor.*, **2** (1), 36–50.
- Kaspi, Y. and T. Schneider, 2013: The role of stationary eddies in shaping midlatitude storm tracks. *J. Atmos. Sci.*, **70**, 2596–2613.
- Kitoh, A., 2004: Effects of Mountain Uplift on East Asian Summer Climate Investigated by a Coupled Atmosphere-Ocean GCM. *J. Climate*, **17** (4), 783–802.
- Kitoh, A. and T. Uchiyama, 2006: Changes in onset and withdrawal of the east asian summer rainy season by multi-model global warming experiments. *JOURNAL-METEOROLOGICAL SOCIETY OF JAPAN SERIES 2*, **84** (2), 247.
- Kitoh, A., S. Yukimoto, A. Noda, and T. Motoi, 1997: Simulated changes in the asian summer monsoon at times of increased atmospheric co₂. *Journal of the Meteorological Society of Japan*, **75** (6), 1019–1031.
- Kodama, Y.-M., 1992: Large-Scale Common Features of Subtropical precipitation Zones (the Baiu Frontal Zone, the SPCZ and the SACZ) Part I: Characteristics of Subtropical Frontal Zones. *J. Meteor. Soc. Japan*, **70**, 813–836.
- Krishnan, R., S. Sundaram, P. Swapna, V. Kumar, D. Ayantika, and M. Mujumdar, 2011: The crucial role of ocean–atmosphere coupling on the Indian monsoon anomalous response during dipole events. *Climate Dynamics*, **37** (1-2), 1–17.

- Kuo, Y.-H., L. Cheng, and R. A. Anthes, 1986: Mesoscale analyses of the Sichuan flood catastrophe, 11-15 July 1981. *Mon. Wea. Rev.*, **114** (11), 1984–2003.
- Li, C. and M. Yanai, 1996: The onset and interannual variability of the Asian summer monsoon in relation to land-sea thermal contrast. *J. Climate*, **9** (2), 358–375.
- Lin, S.-J., 2004: A “vertically lagrangian” finite-volume dynamical core for global models. *Mon. Wea. Rev.*, **132** (10), 2293–2307.
- Liu, X. and Z.-Y. Yin, 2002: Sensitivity of East Asian monsoon climate to the uplift of the Tibetan Plateau. *Palaeogeography, Palaeoclimatology, Palaeoecology*, **183** (3), 223–245.
- Meehl, G. A., et al., 2007: Global climate projections. *Climate change*, 747–845.
- Meehl, G. A., et al., 2009: Decadal prediction: can it be skillful? *Bull. Amer. Meteor. Soc.*, **90** (10), 1467–1485.
- Merlis, T. M. and T. Schneider, 2010: Atmospheric dynamics of Earth-like tidally locked planets. *J. Adv. Model. Earth Syst.*, **2** (13), doi:10.3894/JAMES.2010.2.13.
- Mitchell, J. F., C. Wilson, and W. Cunnington, 1987: On CO₂ climate sensitivity and model dependence of results. *Quarterly Journal of the Royal Meteorological Society*, **113** (475), 293–322.
- Molnar, P., W. Boos, and D. Battisti, 2010: Orographic controls on climate and paleoclimate of Asia: thermal and mechanical roles for the Tibetan Plateau. *Annu. Rev. Earth Planet. Sci.*, **38**, 77–102.
- Muller, C. and P. O’Gorman, 2011: An energetic perspective on the regional response of precipitation to climate change. *Nature Climate Change*, **1** (5), 266–271.
- Neelin, J., 2007: Moist dynamics of tropical convection zones in monsoons, teleconnections, and global warming. *The Global Circulation of the Atmosphere*, T. Schneider and A. H. Sobel, Eds., Princeton University Press, 267–301.

- Ninomiya, K., 1984: Characteristics of Baiu front as a predominant subtropical front in the summer Northern Hemisphere. *J. Meteor. Soc. Japan*, **62** (6), 880–894.
- Ninomiya, K. and T. Murakami, 1987: The early summer rainy season (Baiu) over Japan. *Monsoon meteorology*, C.-P. Chang and T. N. Krishnamurti, Eds., Oxford University Press, 93–121.
- O’Gorman, P. A., R. P. Allan, M. P. Byrne, and M. Previdi, 2012: Energetic constraints on precipitation under climate change. *Surveys in geophysics*, **33** (3-4), 585–608.
- Park, H., J. Chiang, and S. Bordoni, 2012a: Mechanical impact of the Tibetan Plateau on the seasonal evolution of the South Asian monsoon. *J. Climate*, **25** (7), 2394–2407.
- Park, H.-S., J. Chiang, and S. Bordoni, 2012b: Mechanical impact of the Tibetan Plateau on the seasonal evolution of the South Asian monsoon. *J. Climate*, **25**, 2394–2407.
- Peixoto, J. P. and A. H. Oort, 1992: *Physics of Climate*. American Institute of Physics.
- Rodwell, M. and B. Hoskins, 1996: Monsoons and the dynamics of deserts. *Quart. J. R. Met. Soc.*, **122** (534), 1385–1404.
- Rodwell, M. and B. Hoskins, 2001: Subtropical Anticyclones and Summer Monsoons. *J. Climate*, **14** (15), 3192–3211.
- Saito, N., 1985: Quasi-stationary waves in mid-latitudes and the Baiu in Japan. *J. Meteor. Soc. Japan*, **63**, 983–995.
- Sampe, T. and S. Xie, 2010: Large-Scale Dynamics of the Meiyu-Baiu Rainband: Environmental Forcing by the Westerly Jet. *J. Climate*, **23** (1), 113–134.
- Schiemann, R., D. Lüthi, and C. Schär, 2009: Seasonality and interannual variability of the westerly jet in the Tibetan Plateau region. *J. Climate*, **22** (11), 2940–2957.

- Schneider, T., 2004: The Tropopause and the Thermal Stratification in the Extratropics of a Dry Atmosphere. *J. Atmos. Sci.*, **61** (12), 1317–1340.
- Shaw, T. and A. Voigt, 2015: Tug of war on summertime circulation between radiative forcing and sea surface warming. *Nature Geoscience*.
- Smith, T. M., R. W. Reynolds, R. E. Livezey, and D. C. Stokes, 1996: Reconstruction of historical sea surface temperatures using empirical orthogonal functions. *J. Climate*, **9** (6), 1403–1420.
- Sobel, A., J. Nilsson, and L. M. Povalni, 2001: The weak temperature gradient approximation and balanced tropical moisture waves. *J. Atmos. Sci.*, **58**, 3650–3665.
- Solomon, S., D. Qin, M. Manning, Z. Chen, M. Marquis, K. Averyt, M. Tignor, and H. M. (eds.), 2007: IPCC, 2007: Climate Change 2007: The Physical Science Basis. Contribution of Working Group I to the Fourth Assessment Report of the Intergovernmental Panel on Climate Change. Tech. rep., Cambridge University Press, Cambridge, United Kingdom and New York, NY, USA.
- Song, F. and T. Zhou, 2013: Inter-annual variability of east asian summer monsoon simulated by CMIP3 and CMIP5 AGCMs: Skill dependence on Indian Ocean-western Pacific anticyclone teleconnection. *Journal of Climate*, (2013).
- Sperber, K. R., H. Annamalai, I.-S. Kang, A. Kitoh, A. Moise, A. Turner, B. Wang, and T. Zhou, 2012: The Asian summer monsoon: an intercomparison of CMIP5 vs. CMIP3 simulations of the late 20th century. *Climate Dynamics*, 1–34.
- Stevens, B. and S. Bony, 2013: What Are Climate Models Missing? *science*, **1237554** (1053), 340.
- Suda, K. and T. Asakura, 1955: A study on the unusual ‘Baiu’ season in 1954 by means of northern hemisphere upper air mean charts. *J. Meteor. Soc. Japan*, **33**, 1–12.

- Tao, S., 1987: *A review of recent research on the East Asian summer monsoon in China*. Oxford University Press.
- Taylor, K. E., R. J. Stouffer, and G. A. Meehl, 2012: An overview of cmip5 and the experiment design. *Bull. Amer. Meteor. Soc.*, **93** (4), 485–498.
- Teixeira, J., D. Waliser, R. Ferraro, P. Gleckler, G. Potter, et al., 2011: Satellite observations for cmip5 simulations. *CLIVAR Exchanges*, **16** (2).
- Terao, T. and T. Kubota, 2005: East-west sst contrast over the tropical oceans and the post el niño western north pacific summer monsoon. *Geophys. Res. Lett.*, **32** (15).
- Trenberth, K. E., J. W. Hurrell, and D. P. Stepaniak, 2006: The Asian Monsoon: Global perspectives. *The Asian Monsoon*, B. Wang, Ed., Springer Praxis, 67–87.
- Waliser, D. E., 2006: Intraseasonal variability. *The Asian Monsoon*, B. Wang, Ed., Springer Praxis, 203–257.
- Wang, B., 1987: The development mechanism for Tibetan Plateau warm vortices. *J. Atmos. Sci.*, **44**, 2978–2994.
- Wang, B., 2006: *The Asian Monsoon*. Springer Praxis.
- Wang, W., Y.-H. Kuo, and T. T. Warner, 1993: A diabatically driven mesoscale vortex in the lee of the Tibetan Plateau. *Mon. Wea. Rev.*, **121** (9), 2542–2561.
- Webster, P., 1987: The Elementary Monsoon. *Monsoons*, J. S. Fein and P. L. Stephens, Eds., John Wiley & Sons, New York, NY, 3–32.
- Webster, P. and J. Fasullo, 2003: Monsoon: Dynamical Theory. *Encyclopedia of Atmospheric Sciences*, **3**, 1370–1391.

- Wu, G., W. Li, H. Guo, H. Liu, J. Xue, and Z. Wang, 1997: Sensible heat driven air-pump over the Tibetan Plateau and its impacts on the Asian Summer Monsoon. *Collections on the Memory of Zhao Jiuzhang*, Y. Duzheng, Ed., Chinese Science Press, 116–126.
- Wu, G., Y. Liu, B. He, Q. Bao, A. Duan, and F. Jin, 2012: Thermal Controls on the Asian Summer Monsoon. *Scientific Reports*, **2**, 404.
- Wu, G., L. Sun, Y. Liu, H. Liu, S. Sun, and W. Li, 2002: Impacts of land surface processes on summer climate. *Selected Papers of the Fourth Conference on East Asia and Western Pacific Meteorology and Climate*. In: C. P. Chang et al. (eds), World Scientific, 64–76.
- Wu, G. et al., 2007a: The influence of mechanical and thermal forcing by the Tibetan Plateau on Asian climate. *Journal of Hydrometeorology*, **8**, 770–789.
- Wu, G., et al., 2007b: The influence of mechanical and thermal forcing by the Tibetan Plateau on Asian climate. *J. Hydrol.*, **8** (4), 770–789.
- Xie, S.-P., C. Deser, G. A. Vecchi, J. Ma, H. Teng, and A. T. Wittenberg, 2010: Global warming pattern formation: sea surface temperature and rainfall*. *Journal of Climate*, **23** (4), 966–986.
- Xie, S.-P., K. Hu, J. Hafner, H. Tokinaga, Y. Du, G. Huang, and T. Sampe, 2009: Indian ocean capacitor effect on indo-western pacific climate during the summer following el niño. *J. Climate*, **22** (3), 730–747.
- Yanai, M. and G. Wu, 2006: Effects of the Tibetan Plateau. In: B. Wang (ed.). *The Asian Monsoon*, B. Wang, Ed., Springer Praxis, 513–549.
- Yang, J., Q. Liu, S.-P. Xie, Z. Liu, and L. Wu, 2007: Impact of the indian ocean sst basin mode on the asian summer monsoon. *Geophys. Res. Lett.*, **34** (2).
- Yang, S. and W. K.-M. Lau, 2006: Interannual variability of the Asian monsoon. *The Asian Monsoon*, B. Wang, Ed., Springer Praxis, 259–293.

- Yeh, T. C., S. W. Lo, and E. C. Chu, 1957: On the heat balance and circulation structure in the troposphere over the Tibetan Plateau and its vicinity. *Acta Meteor. Sinica*, **28**, 108–121.
- Zhang, Y., X. Kuang, W. Guo, and T. Zhou, 2006: Seasonal evolution of the upper-tropospheric westerly jet core over east asia. *Geophysical research letters*, **33** (11).
- Zhao, P., S. Yang, M. Jian, and J. Chen, 2011a: Relative controls of asian-pacific summer climate by asian land and tropical-north pacific sea surface temperature. *J. Climate*, **24** (15), 4165–4188.
- Zhao, P., S. Yang, H. Wang, and Q. Zhang, 2011b: Interdecadal relationships between the asian-pacific oscillation and summer climate anomalies over asia, north pacific, and north america during a recent 100 years. *Journal of Climate*, **24** (18), 4793–4799.
- Zhou, T., et al., 2009: Why the western pacific subtropical high has extended westward since the late 1970s. *Journal of Climate*, **22** (8), 2199–2215.